

Advanced Processing of Graphene for High Performance Devices

Submitted in partial fulfillment of the requirements

for the degree of

Doctor of Philosophy

by

Poonam Jangid

(Roll No. 144076008)

Supervisor

Prof. Anil Kottantharayil



**Department of Electrical Engineering
Indian Institute of Technology Bombay**

2020

Dedicated to... My Parents

Thesis Approval

The Thesis entitled

Advanced Processing of Graphene for High Performance Devices

By
Poonam Jangid
(Roll No. 144076008)

is approved for the degree of
Doctor of Philosophy



13/05/2020

Prof. Santanu Mahapatra



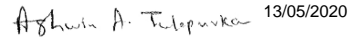
14 May 2020

Prof. Siby K. George



11 May 2020

Prof. Anil Kottantharayil



13/05/2020

Prof. Ashwin Tulapurkar

Date: May 11, 2020
Place: IIT Bombay, Mumbai

Declaration

I declare that this written submission represents my ideas in my own words and where others' ideas or words have been included, I have adequately cited and referenced the original sources. I declare that I have properly and accurately acknowledged all sources used in the production of this report. I also declare that I have adhered to all principles of academic honesty and integrity and have not misrepresented or fabricated or falsified any idea/data/fact/source in my submission. I understand that any violation of the above will be a cause for disciplinary action by the Institute and can also evoke penal action from the sources which have thus not been properly cited or from whom proper permission has not been taken when needed.



Poonam Jangid
(144076008)

Date: May 11, 2020
Place: IIT Bombay, Mumbai

Acknowledgements

First and foremost, I would like to express my sincere gratitude to my supervisor Prof. Anil Kottantharayil for his support, encouragement and discussions throughout the course of my research work. I also owe many thanks to Prof. Saurabh Lodha and Prof. Ashwin A. Tulapurkar for their valuable suggestions and comments during my PhD program as research progress committee members.

I would like to acknowledge the "IITB Nanofabrication Facility" (IITBNF), Department of Electrical Engineering, IIT Bombay where all the work presented in this thesis has been carried out. I wish many thanks to all the IITBNF staff members for their technical and friendly support throughout the work. My special thanks to Gayatri and Dawuth, who helped me in getting acquainted with Raith 150 Two system. I acknowledge Centre for Research in Nanotechnology and Science (CRNTS) and Sophisticated Analytical Instrument Facility (SAIF), IIT Bombay for SEM and Raman measurements. I thank Prof. Indradev Samajdar, former head of the SAIF, for allowing me to get trained and have access to the LRS (Laser Raman Spectrometer) facility even in wee hours. I acknowledge the IRCC conductive Atomic Force Microscopy (c-AFM) facility and Nanoindenter Central facility of IIT Bombay for AFM and indentation analysis respectively.

I would like to thank Department of Science and Technology, Govt. of India and The Department of Electronics and Information Technology, Govt. of India for the financial assistance as well as research facilities in our laboratory.

I am very much thankful to our present and past research group members for their suggestions and comments. I want to thank Shaivalini Singh, Abhishek Mishra, Meenakshi B., Kousik Midya, Manali Khare, Amritha Janardanan, Manini Gour, Sahul Nath, Anakha, Sreejith, Robin, Dibyendu, Prem Sai, Rajashekhar, Tarun and Saima for all kind of support, discussion on several technical and non technical topics. Special Thanks to Sarthak whose assistance was a milestone in the completion of this thesis.

There are some best friends to me whose encouragement and emotional supports I can never forget in my life, specially Manoj, Sumit, Luv, Jai Prakash, Parul, Nayana, Sonali, Jayeeta, Dipankar, Nikita and Jayshree. They backed me whenever I needed any help. Special thanks to HTEM group friends (Devika, Amardeep, Pranav, Chithra, Farjana, Vaibhav) for various gatherings and outings which make this journey a lot more joyful experience.

Last but not the least, I am thankful to my parents, my brothers and sister for their constant support and encouragement for my higher studies.

Abstract

Graphene Nanoribbons (GNRs) are one dimensional nanostructures where confinement of charge carriers in one direction leads to unique electronic and spin transport properties. Graphene has limited use for transistor applications because of zero bandgap but GNRs can be used. The sub-10 nm and < 20 nm width of GNRs exhibit the finite bandgap. Electronic band structure or band gap of graphene can be modified by narrowing the width, and edge disorders.

The aim of present study is to fabricate graphene nanoribbons by Pt nanocrystal-assisted etching of graphene and study the electrical characteristics of bottom-gated field-effect graphene nanoribbon transistors. This work report the realization of graphene nanoribbon transistors with I_{ON}/I_{OFF} ratio of 2×10^7 and electron and hole mobilities of $400 \text{ cm}^2\text{V}^{-1}\text{s}^{-1}$ and $1100 \text{ cm}^2\text{V}^{-1}\text{s}^{-1}$ respectively at 6 K. Pt-catalyzed etching of exfoliated graphene and CVD graphene are compared to evaluate their etching behavior by thermally-activated Pt nanoparticles. Transition metal platinum act as a catalyst material for etching of graphene due to high carbon solubility. Etching behavior in graphene is evaluated by AFM and SEM techniques. Sub-10 nm and 10-20 nm width of graphene nanoribbons are obtained by etching of graphene by moving of two Pt nanoparticles in parallel to each other. AFM of etched graphene exhibit crystallographic orientation angles 30° , 60° , 90° , 120° and 150° which is attributed to armchair and zigzag edges. The distribution of most of the angles are $30^\circ \times n$, where n has integer value between 0 and 6. The electronic structural changes in etched graphene is studied by Raman Spectroscopy. Polarized Raman spectroscopy and mapping of etched graphene reveals edge chirality of GNRs. D-band is more prominent in armchair edges than zigzag edges. High on-off ratio of GNR transistors define the bandgap opening in graphene nanoribbons. The performance parameters obtained are some of the best values in comparison with other GNRs synthesis methods like chemical solution and lithography techniques reported in the lit-

erature. The high performance indicates the highly smooth edges along crystallographic directions in GNR obtained by the catalytic etching process.

Graphene is a fascinating material for micro and nano devices but fracture arises during device fabrication or graphene processing, hinder the properties of graphene. Another reason of fracture in graphene devices is electrical breakdown due to resistive heating. Reconstruction of graphene and GNRs are necessary for electronics applications of graphene. The fractured graphene is reconstructed by e-beam irradiation and methane gas treatment at high temperature. Physical characterization techniques like SEM and AFM confirm the healing of cracks. Graphene layers are investigated before breakdown and after reconstruction of fractured graphene by Raman Spectroscopy. Analysis of current-voltage characteristics before breakdown and after reconstruction exhibit restoration of current values. The maximum current density has the current density order of 10^8 A/cm² after reconstruction. Reconstruction of graphene and GNRs are required for on-chip interconnect applications because of high current carrying requirements. Methane gas treatment method is highly scalable and more cost-effective than e-beam irradiation for reconstruction of graphene and GNRs. This study suggest that high crystalline GNRs are achievable with high I_{ON}/I_{OFF} ratio and healing of fractured graphene is viable by methane gas treatment and e-beam irradiation methods.

Table of Contents

Acknowledgements	v
Abstract	vii
List of Figures	xii
List of Tables	xxiv
List of Acronyms	1
1 Introduction	4
1.1 Scope of the Present Work	7
1.2 Thesis Organization	8
2 Literature Review	10
2.1 Introduction to Graphene	10
2.2 Band Gap Engineering	12
2.2.1 Theoretical Predictions	14
2.2.2 Experimental Progress	17
2.3 Graphene Nanoribbon Synthesis Methods	18
2.3.1 GNR Fabrication by Lithography Technique	18
2.3.2 GNRs by Unzipping of Carbon Nanotubes	23
2.3.3 GNRs Fabrication by Atomic Force Microscopy, Scanning Probe Lithography and Focused Ion-Beam Etching Techniques	25
2.3.4 Chemically Derived GNRs	26
2.3.5 Metal-Assisted Etched GNRs	28
2.4 Reconstruction of Carbon Nanotubes, Graphene and Graphene Nanoribbons	31

2.4.1	Reconstruction of Graphene by High Energy Electrons in TEM	31
2.4.2	Healing of Carbon Nanotubes by Low Energy Electrons in Scanning Electron Microscopy System	36
2.4.3	Effect of Electron-Beam Irradiation on Graphene and GNR Devices	38
2.5	Breakdown Current Density of Graphene and Graphene Nanoribbons	42
2.6	Summary	44
3	Experimental Techniques Used in This Work	46
3.1	Preparation of Graphene on SiO ₂ Substrate	46
3.2	Electron-Beam Lithography	47
3.3	Sputtering Technique	51
3.4	Optical Microscopy	52
3.5	Scanning Electron Microscopy (SEM)	53
3.6	Atomic Force Microscopy (AFM)	55
3.7	Raman Spectroscopy and Imaging	57
3.8	Semiconductor Device Analyzer	61
3.9	Summary	63
4	Graphene Nanoribbon Transistors with High I_{ON}/I_{OFF} Ratio and Mobility	65
4.1	Synthesis of Metal Nanoparticles	65
4.1.1	Synthesis of Metal Nanoparticles by Electroless Plating	66
4.1.2	Synthesis of Metal Nanoparticles by Sputtering and Thermal Annealing	67
4.2	Why Pt-assisted Etching of Graphene	67
4.3	Fabrication of GNR Field-Effect Transistors	68
4.4	Results and Discussion	70
4.5	Summary	81
5	Reconstruction of Fractured Graphene and GNRs by Thermal Treatment in Methane Gas and by Electron-Beam Irradiation	84
5.1	Reconstruction of Graphene by Methane Gas Exposure	86
5.1.1	Fabrication of Graphene Devices	86
5.1.2	Results	87

5.1.3	Discussion	95
5.2	Reconstruction of Graphene by E-Beam Irradiation	96
5.2.1	Experimental	97
5.2.2	Results	97
5.2.3	Discussion	102
5.3	Summary	104
6	Conclusions and Future Scope	105
6.1	Future Directions	106
	Appendices	108
A.1	Process Recipe for Fabrication of Graphene Nanoribbon Transistors	108
A.2	Physical Characterization	112
A.3	Graphene Device Fabrication for Reconstruction	112
A.4	Device Characterization	112
	References	113
	List of Publications	133

List of Figures

1.1	Ambipolar electric field effect in monolayer graphene. Resistivity as a function of gate voltage, resistivity decreases rapidly with gate voltage and this indicates high carrier mobility.	5
1.2	Armchair and zigzag edges of GNR. Nanoribbon edge structure determine the electronic structure.	6
1.3	Bandgap as a function of nanoribbon width from experiments and calculations.	7
2.1	Graphene is the building block of other graphitic materials in other dimensionalities. Graphene can be fold into 0D buckyballs, wrapped-up into 1D nanotubes and make 3D graphite (stack of layers).	11
2.2	(a) Crystal structure of monolayer graphene with two atoms (A and B). The shaded rhombus region represents unit cell of graphene, \mathbf{a}_1 and \mathbf{a}_2 are the the primitive lattice vectors. (b) The Brillouine zone of graphene with two Dirac point K and K'.	12
2.3	Electronic dispersion in the honeycomb lattice. Left: energy spectrum of graphene calculated by tight binding approach. Right: zoom-in of valance and conduction band which is showing one Dirac point.	12
2.4	(a) Armchair and zigzag nanoribbons. N_a and N_z are the number of dimer lines across armchair and zigzag ribbon width. (b) Schematic drawing of (8,1) GNR. The chiral vector (m, n) connecting crystallographically equivalent sites along the edge defines the edge orientation of the GNR (black arrow). The blue and red arrows are the projections of the (8, 1) vector onto the basis vectors of the graphene lattice.	13

2.5	Scanning electron micrograph of a large graphene, which shows that most of the monolayer faces are zigzag and armchair edges, as indicated by blue and red lines represented.	13
2.6	(a) Basic electronic band structure of zigzag GNR calculated using tight-binding model. GNR configurations depend on chirality and ribbon width. (b) Magnetic moment per edge unit length M versus chirality angle θ for 7-nm-wide GNRs that was calculated using the mean-field Hubbard model at $U/t = 1$ (Red circles). Here U and t represents Coulomb repulsion and hopping integrals respectively. The dashed black line corresponds to the edge-state density $n(\theta)$ in the limit of infinite width.	15
2.7	(a) Band gap of armchair GNRs versus GNR width (calculated using the tight-binding approach). (b) Band gaps Δ^0 and zone-boundary splittings Δ^1 of the spin-polarized ground states of zigzag GNRs as a function of width based on local density approximation.	16
2.8	Extracted bandgap values of GNR as a function of ribbon width. Symbol represents experimental data. The black dotted line is the experimental data in empirical form E_g (eV) = 0.8 / W (nm). The purple, orange and blue solid lines show the bandgap dependence on width for three armchair families, extracted using first principle calculations. Green solid lines represents zigzag edged nanoribbons, extracted using local density approximation.	18
2.9	(a) Schematic of back-gated nanoribbon transistor. (b) Scanning Electron Microscopy (SEM) image of the 12 nm nanoribbon, magnified view of nanoribbon is shown in inset.	19
2.10	(a) Transport characteristics of 12 nm wide back-gated GNR FET at various temperatures. (b) Output characteristics at 4 K. (c) Differential conductance map of a 12 nm GNR FET as a function of V_{DS} and V_{BG} at 4K. (d) Differential conductance and absolute drain current $v/s V_{DS}$ at V_G 50.5 V.	20

2.11	(a)-(d) Optical images of epitaxial nanoribbon transistors on wafer size SiC substrate. (e) SEM image of GNR having 10 nm width with source and drain contact metal. (f) SEM image of HSQ array ribbon patterns, consisting of 13 nm GNR line width and 17 nm space, showing no deformation or collapse. HSQ was used as a mask to etch graphene during O ₂ plasma etch process.	21
2.12	(a) Drain Current as a function of gate voltage for 10 nm GNR FET at various temperatures. I _D is dominated by thermionic emission at 300 K and suppressed at 4 K. Band-to-band tunneling dominate at 4 K. (b) I _D versus V _{DS} at different V _{GS} showing clear on-off states. (c) I _D versus V _{DS} with fixed V _{GS} for different GNR width at 4 K.	22
2.13	The differential conductance map as a function of V _{DS} and V _{GS} of GNR width 10 nm (c) and 17 nm (d) are shown in (a) and (b) at 4 K respectively. Red and black color indicate high and low conductance in the map. (e) Energy band diagram model is based on the Schottky barrier. (f) Extracted band gap of GNR FET vs. width of GNR. The linear line was predicted using the model. The deviation of these GNRs width is around 0.5 nm by SEM.	22
2.14	Schematic of GNRs production from CNTs. (a) A pristine Multi Wall Carbon Nanotube (MWCNT) was used as the starting raw material. (b) Poly Methyl Methacrylate (PMMA) resist were coated on MWCNT/Si substrate. (c) PMMA-MWCNT film was peeled from the Si substrate, turned over and then exposed to an Ar plasma. (d-g) Etching time was varied: GNRs with CNT cores were obtained after etching for a short time t ₁ - (d) tri-, bi- and single-layer GNRs were produced after etching for times t ₂ , t ₃ and t ₄ , respectively (t ₄ > t ₃ > t ₂ > t ₁ ; e-g). (h) PMMA was stripped from nanoribbons.	24

2.15	(a) A schematic of GNR device. (b) Transfer characteristic of 16-nm-wide GNR device probed in vacuum after electrical annealing. Dirac point is located near $V_{gs} = 50$ V. Inset shows the AFM image of this device; scale bar is 200 nm. (c) I_{ds} - V_{gs} curves for 7-nm-wide GNR device at various biases probed in air. The on/off ratio is 10 for this device. (d) I_{ds} - V_{ds} curves for the device in c at gate biases V_{gs} ranging from 240 V (bottom) to 40 V (top) in steps of 10 V.	25
2.16	(a,b) GNR cut in the zigzag direction with various width (4.6 and 2.5 nm) by SPL. Height profile of GNR is shown below figure (a) and (b). (c) 20 nm large arrays of GNRs by using FIB etching technique.	26
2.17	(a) Schematic of device geometry. Below: SEM of the device is showing 100 nm wide contact pad with a 26 nm source drain gap. (b) Transport characteristic of a device at $V_{SD} = 1$ V in both air and under vacuum at 77 K. (c) Electrical characterization of a typical device post passivation, under vacuum, at 77 K. I_D as a function of gate bias at different V_{SD} . (d) Output characteristics at different gate bias, inset: same data presented in logarithmic scale.	27
2.18	(a) Left : schematic of GNR structures that shows 120° angle of trench by nanoparticles. Right : AFM images of GNR with 120° angle of trench. (b) Left : schematic of GNR structures that shows 60° angle of trench. Right : AFM images of GNR with 60° angle of trench.	29
2.19	(a) Transport characteristic and b) Output characteristics of optimum etched nanoribbon area. SEM image of device is shown in inset of figure (b) with 1 μm scale bar. (c) Transport and (d) Output characteristic of high etched density area of nanoribbons.	30
2.20	(a) Graphene nanoribbons show very few zigzag (pink lines) and armchair edges (green lines) before Joule heating. (b, c) GNRs after 10 min. Joule heating at 1.6 V. Most of the edges are either zigzag or armchair edges, as shown in figure (c). (d) High-magnified view of the annealed sample is showing zigzag-armchair and zigzag-zigzag edges. Scale bars in (a), (b) and (c), 4 nm; in (F), 1 nm.	32

2.21	(a) Schematic diagram of experimental setup for measurement of electrical properties of graphene in the TEM-STM holder. (b) TEM image of a monolayer graphene with Pt probe and Au tip. (c, d) Schematic picture of "top-to-top" and "layer-to-layer" joining geometries of graphene sheets. (e) TEM image showing the practical manipulation of a graphene sheet.	34
2.22	Joining of individual single layer graphene with both joining geometries (a) Graphene monolayer with Pt probe and Au tip. Inset is showing High Resolution Transmission Electron Microscopy (HRTEM) image of monolayer. (b) Two segments of graphene layer after applying a voltage. (c) "Top-to-top" joining geometry. (d) Same graphene sheet after cracks due to high applied voltage. (e) I-V characteristic of original and joined graphene layer. (f) "Layer-to layer" joining geometry. (g) Same joined graphene layer was broken again due to high biasing and in situ pulling process. (h) I-V characteristic of joined graphene layer and graphene layer at the Pt probe and Au tip respectively.	35
2.23	(a) MWNT between contact pads. (b) I-V characteristic of the same tube. (c) SEM of broken tube after applying high voltage. (d) SEM image of same tube after repairing. (e,f) I-V characteristics after breakdown and after healing.	37
2.24	(a) I-V characteristic of current annealed CNT before breakdown. (b) I-V curve after joining of tube. (c) Comparison of current values in the range -5 to 5 V before and after joining. (d) Comparison of current values in the range -6 to 6 V before and after joining.	38
2.25	(a) Conductance versus gate voltage before and after exposure for a suspended graphene. (b) Raman Spectrum before and after irradiation on same sample. This graphene was exposed in EVO 40 SEM system with 30 keV acceleration voltage and 0.15 nA current for 5 min.	39
2.26	(a) Electrical characteristics of low EBL exposure current (red), moderate EBL exposure current (blue) and high EBL exposure current (green). Low exposure current has better characteristics than moderate and high exposure current. (b) Raman Spectrum of the same devices. G and 2D peak have red shift due to increment of exposure current dose.	40

2.27	Schematic diagram of resist residual formation and radicals trapping on active area of graphene device. (a) Top view of exfoliated graphene and e-beam irradiated area. (b) Resist radicals are transferred to unexposed graphene-PMMA interface due to e-beam exposure. (c) Irradiated area after development and plasma etching. (d) Second PMMA layer is spin coated and previous residual layer remain under this second PMMA layer which is solidified after baking.	41
2.28	Electron-beam irradiation effects on Graphene Field-effect Transistors (GFETs). (a) Six consecutive sweeps after e-beam irradiation. Hysteresis has been reduced after sixth sweeping. (b) First and sixth sweep of irradiated device compared with the unexposed device. (c) Experimental data values compared with modeling data. (d) Summary of extracted mobility, contact resistance and carrier concentration.	43
2.29	(a) Current-voltage characteristics of 22 nm width GNR array of 10 GNRs which shows breakdown after certain bias voltage. (b,c) Resistance and breakdown current density (unit -10^8 A/cm ²) of 10 GNRs. (d) Breakdown current density versus resistivity. (e) The average breakdown current density as a function of wire length.	44
3.1	Optical micrograph of (a) exfoliated graphene flakes on SiO ₂ substrate, and (b) transferred CVD graphene. For identification of graphene boundary on SiO ₂ substrate, red dashed line is drawn.	47
3.2	Schematic description of an e-beam lithography process for patterning of metals.	49
3.3	(a) Block Diagram of major components of electron beam lithography system. (b) A simplified ray diagram of round-beam electron lithography system.	50
3.4	(a) SEM image of 60 nm width array of lines patterned using Raith 150 ^{Two} lithography system. (b) SEM image of array of numbers which was patterned by Raith 150 ^{Two} system.	50
3.5	(a) Schematic illustration of sputtering system. (b) Photograph of orion sputter system which is taken from IITB website.	51
3.6	Contrast of graphene as a function of wavelength.	52

3.7	Optical images of mechanically exfoliated graphene. (a) Bright field optical image. (b) Dark field optical image. Graphite flake boundary is glowing more than few layer graphene.	53
3.8	(a) Principle of SEM instrument is shown by a schematic diagram. (b) Photograph of the FESEM instrument which is used for this work.	54
3.9	(a) Schematic description of electron interaction with incident electron-beam. (b) SEM image of 60 nm width array of lines which is taken in Raith 150 Two lithography system.	55
3.10	(a) Schematic of principle of atomic force microscopy. (b) MFP3D Origin atomic force microscope. Image is taken from iitb website.	56
3.11	(a) AFM image of monolayer and trilayer graphene. Source of image is Graphene Industries Ltd.website. (b) Carbon nanotubes and graphene nanoribbons. GNRs was prepared by sonication of carbon nanotubes.	57
3.12	(a) Raman spectrum of bulk graphite and graphene obtained using a 514 nm laser. (b,c) Raman spectra using 514 nm and 633 nm lasers with the number of layers. (d) D band at the edge of graphite and monolayer graphene (514 nm laser). (e) The four components of the 2D band is shown in bilayer graphene (514 and 633 nm).	58
3.13	(a) Raman mapping of G band intensity of armchair (edge 1) and zigzag (edge 2). (b,c) Raman imaging of D band intensity along horizontal and vertical polarization direction. (d) Raman spectra of edge 1 and 2 (a,b) due to horizontal polarization and (c,d) due to vertical polarization. (e) Spectra of D band intensity of b and c.	59
3.14	Photograph of Horiba LabRAM HR model of laser confocal Raman microscope.	60
3.15	(a) Source I, measure V configuration. (b) Source V, measure I configuration. (c) Schematic configuration to use a switching matrix for I-V and C-V testing. The figures are taken from Keysight Technologies Inc. website (URL: https://www.keysight.com/en/pc-2250789/b1500a-semiconductor-device-analyzer?nid=-33019.0.00cc=INlc=eng).	62
3.16	Measurement setup of Agilent B1500 Semiconductor Device Analyzer for I-V and C-V characterization at different temperature.	63

4.1	(a) SEM images of clusters of Ni nanoparticles. Solvent residue is also visible around clusters of nanoparticles. (b) Ni nanoparticles are seen to be of rectangular shape and have size in the range of 100 - 200 nm.	66
4.2	(a) SEM image of Ni nanoparticles synthesized by sputtering. (b) 5-150 nm size of Ni nanoparticles. 150 nm size of Ni nanoparticle is shown by yellow marker.	67
4.3	Schematic of GNRs fabrication by electron beam lithography.	69
4.4	(a) Cartoon of cutting of graphene by Pt nanoparticles. (b) Array of 1 μm linewidth of Pt nanoparticles after annealing at 500°C.	69
4.5	SEM image of (a) etched CVD graphene (b) Etched exfoliated graphene show sub-10 nm and ~ 20 nm GNRs (shown by black arrows). Pt nanoparticles also shows etching in 60° crystallographic orientation angle.	70
4.6	SEM image of etched exfoliated graphene. One nanoribbon with two Pt nanoparticles (black circle with arrow) at the edges is shown and other three nanoribbons do not have any nanoparticles at the edges shown by black arrows.	71
4.7	SEM image of etched exfoliated graphene by (a) Ni nanoparticles and (b) Pt nanoparticles. Nanoparticles are highlighted by yellow circles.	72
4.8	AFM image of etched CVD graphene. (a) Wrinkles of CVD graphene are shown by yellow arrows. (b) Etched graphene area is shown by yellow arrow. The etching of CVD graphene is randomly orientated. White particles are Pt nanoparticles.	72
4.9	Pt nanoparticle assisted etching of graphene (a) AFM topography image of etched graphene that shows chirality preserving angles 30°, 60° and 120°. (b) AFM phase image of etched geometric nanostructures. (c) AFM topography image showing chirality angle 60° and 10 nm GNR. Pt nanoparticles do not cross previously etched trenches or region. (d) AFM topography image of etched trenches. White particles are Pt nanoparticles.	73
4.10	AFM image of etched graphene. The black arrows are showing that nanoparticles do not etch previously etched trench and turn away from it. The etched trench turns away in nanometer distance because of Coulombic interactions. White particles are Pt nanoparticles.	74

4.11	(a) Raman spectra of pristine graphene before etching and after Pt catalyzed etching. (b) Polarized Raman spectra of etched graphene. (c) Statistics of angles that preserve crystallographic orientations. Most of the trenches make 60° and 120° angles that have identical crystallographic orientations (zigzag or armchair).	76
4.12	D-band Raman Mapping of etched CVD and exfoliated graphene. Black arrows are showing higher D-band intensity (magenta color) and less intensity is shown by red color.	77
4.13	(a) Transfer characteristic (drain voltage 1.5 V) and (b) output characteristics of ~15 nm wide GNR. Transfer characteristic shows ~600 on/off ratio. (C) SEM image of device with Ti-Au electrodes. The channel length is 110 nm.	77
4.14	(a) Drain current as a function of gate bias at different drain voltages for ~18 nm wide GNR device. Transfer characteristic shows high on/off ratio of 2.2×10^7 . (b) Drain current as a function of drain voltage. (c) SEM image of device with Ti-Au electrodes. The channel length is 500 nm. . .	78
4.15	(a) Device performance of graphene nanoribbon field effect transistors. The I_{ON}/I_{OFF} ratio of various ribbon widths for $V_D = 0.5$ V at low temperature 6 K. (b) Data from reference Li et al. compared with our data. . . .	79
4.16	Bandgap as a function of ribbon width at different temperature.	80
4.17	The mobility of GNRs as a function of width of nanoribbons. Mobility of GNRs decrease with ribbon width because of edge scattering and acoustic phonon scattering.	80
5.1	A simplified ray diagram of graphene reconstruction methods investigated in this work.	85
5.2	Process sequences used for fabrication and characterization of two groups of devices.	87
5.3	(a) Measured I-V characteristics of a graphene device showing electrical breakdown. Insets show SEM images of the graphene before and after electrical breakdown. (b) AFM image of a device after breakdown. . . .	88

5.4	(a) I-V characteristics of group A devices before breakdown, after breakdown and after 15 min. of thermal treatment in methane. Current is not fully restored after 15 min. of methane exposure. (b) Current-voltage characteristics after 30 min. of thermal treatment in methane. (c) Current-voltage characteristics before breakdown and after 45 min. of thermal treatment in methane gas. (d) Comparison of current values before and after 60 min. of methane treatment.	89
5.5	(a) I-V characteristics of a device after breakdown. The current is in the range of picoamperes, the noise floor of the measurement system, after breakdown. (b) Ratio of current after methane gas exposure to the current before breakdown (both the currents measured at 3 V) as a function of methane exposure time. I_{BB} - Before Breakdown current, I_{AME} - After Methane Exposure current.	90
5.6	(a) SEM of graphene showing crack after breakdown and (b) SEM image of reconstructed graphene. Crack is healed after CH ₄ exposure.	90
5.7	(a) AFM image of graphene with small crack width of ~ 10 nm. (b) AFM image after healing of small crack. (c) AFM image of graphene with a large crack (~ 120 nm) after breakdown. (d) AFM image after reconstruction of large crack in (c).	91
5.8	The maximum current density (J_{MAX}) of graphene as a function of (a) length and (b) resistivity (ρ). Maximum current density decreases with the resistivity and length. The lines are fits to experimental data.	92
5.9	(a) Raman spectra before and after CH ₄ exposure for 30 min. G and 2D peaks are red shifted after CH ₄ exposure, suggesting doping. (b) Deconvolution of the 2D peak obtained before breakdown. (c) Deconvolution of the 2D obtained after CH ₄ exposure. (d) Raman spectra obtained on SiO ₂ far from device areas before breakdown and after CH ₄ exposure. . .	93
5.10	Atomic Force Microscopy (AFM) image of exfoliated graphene with consecutive force points. The AFM tip force was 800 nN.	94

5.11	(a) AFM image of exfoliated graphene after force microscopy with 800 nN force. Black arrow shows the fracture. The magnified view of fracture is shown in the inset of figure (a). (b) AFM image of exfoliated graphene after thermal treatment with methane gas. Fracture is healed after thermal treatment.	95
5.12	(a) AFM image of exfoliated graphite flake after nanoindentation with 1 mN force. (b) Height profile along the blue line in figure(a). Depth and width of nanoindent are approximately 6 nm and 300 nm. (c) AFM image of exfoliated graphene after thermal treatment in methane gas. (d) Height profile of blue line in figure(c). The depth of the indent has decreased from 6 nm to 3 nm at many locations within the 300 nm indicating reconstruction.	96
5.13	Schematic of graphene healing process. (a) Intact graphene device with contact pads. (b) Fractured graphene after electrical breakdown. (c) Healed graphene after CH ₄ exposure.	97
5.14	Process sequences used for fabrication and characterization of two groups of devices for reconstruction of graphene by e-beam irradiation and e-beam irradiation with methane exposure.	98
5.15	(a) Current-voltage characteristic of graphene before breakdown, after breakdown and after e-beam exposure. (b) Fractured graphene is showing picoampere currents after breakdown.	99
5.16	(a) SEM image of graphene nanoribbons after breakdown and (b) after e-beam irradiation. After breakdown it is showing crack and after irradiation crack is not clearly visible.	99
5.17	Current-voltage characteristics (a) Before breakdown and after 2 min. e-beam irradiation and 15 min. of methane exposure. (b) Before Breakdown and after 2 min. e-beam irradiation and 60 min. of methane exposure.	100
5.18	(a) SEM of graphene crack after breakdown and (b) Healed graphene after e-beam with CH ₄ exposure.	100
5.19	(a) SEM of intact graphene before breakdown (no crack) and (b) Crack is shown after electrical stress. (c) Crack is invisible after CH ₄ gas treatment.	101

5.20	(a) Ratio of current after e-beam with methane gas exposure to the current before breakdown (both the currents measured at 3 V) as a function of methane exposure time. (b) Maximum current density as a function of resistivity.	101
5.21	(a) Raman spectrum of graphene before breakdown and after e-beam irradiation. (b,c) Lorentzian fitting of 2D peak before and after e-beam irradiation which confirms number of layers are same. (d) Raman Spectrum of graphene before breakdown and after e-beam irradiation with methane exposure. (e,f) Lorentzian fitting of 2D peak before and after e-beam irradiation with methane exposure which confirms the more number of graphene layer formation.	103
5.22	Schematic of graphene healing process. (a) Graphene device with contact pads. (b) Fractured graphene after electrical breakdown and exposed with e-beam irradiation. (c) Healed graphene after e-beam irradiation.	104

List of Tables

4.1	Comparison of various GNR transistor characteristics reported in the literature using different fabrication methods. GNR devices fabricated using Pt nanocrystal-assisted etching shows better performance than previously reported GNR devices. DSA - Direct Self Assembly, CDL = Carbon Dimer Lines, NA - Not Available.	82
-----	--	----

List of Acronyms

AC	Alternating Current
AFM	Atomic Force Microscopy
ALD	Atomic Layer Deposition
Au	Gold
BSD	Backscatter Electron Detector
Cr	Chromium
Cu	Copper
CNP	Charge Neutrality Point
CNTs	Carbon Nanotubes
C-V	Capacitance-Voltage Characteristics
CVD	Chemical Vapour Deposition
DFT	Density Functional Theory
DR	Double Resonance
DTM	Direct Transconductance Method
EBID	Electron-Beam-Induced Deposition
EBL	Electron Beam Lithography
EHT	Extra High Tension

Fe	Iron
FESEM	Field Emission Scanning Electron Microscopy
FET	Field Effect Transistor
FIB	Focused Ion Beam
GFET	Graphene Field Effect Transistor
GIS	Gas Injection System
GNR	Graphene Nanoribbons
HOPG	Highly Oriented Pyrolytic Graphite
HRTEM	High Resolution Transmission Electron Microscopy
HSQ	Hydrogen Silsesquioxane
IPA	Iso-Propyl alcohol
I-V	Current-Voltage Characteristics
LDA	Local Density Approximation
LED	Light Emission Diode
LER	Line Edge Roughness
MIBK	Methyl Isobutyl Ketone
MOSFET	Metal Oxide Semiconductor Field Effect Transistor
MWNT	Multi-wall Nanotube
NEGF	Non-equilibrium Greens Function
Ni	Nickel
Pt	Platinum
PMMA	Poly Methyl Methacrylate

PmPV	poly(m-phenylenevinylene-co-2,5-dioctoxy-p-phenylenevinylene)
RIE	Reactive Ion Etching
RT	Room Temperature
SB	Schottky Barrier
SE	Secondary Electron
SED	Secondary Electron Detector
SEM	Scanning Electron Microscope
SMU	Source Measure Unit
SPL	Scanning Probe Lithography
STM	Scanning Tunneling Microscope
Ti	Titanium
TEM	Transmission Electron Microscopy
TEM-STM	Transmission Electron Microscopy-Scanning Tunneling Microscope
TLM	Transmission Line Method
TM	Transition Metal
XPS	X-ray Photoelectron Spectroscopy

Chapter 1

Introduction

Graphene is known as a concept since 1940s [1]. In 2004, A. K. Geim and K. S. Novoselov discovered a new material graphene which has attracted the attention of various research groups. Graphene has superior and exceptional properties such as ultra high mobility (greater than Si - $200,000 \text{ cm}^2\text{V}^{-1}\text{s}^{-1}$ at 300 K and $120,000 \text{ cm}^2\text{V}^{-1}\text{s}^{-1}$ in suspended graphene at 240 K) [2, 3], very high thermal conductivity ($> 3000 \text{ WmK}^{-1}$) [4], high Young's modulus (1 TPa), high mechanical strength (130 GPa) [5], high optical transmittance [6] and impermeability to all gases [7]. The ultra high mobility of graphene is the most interesting feature from device perspective as high mobility is the prerequisite for transistors. One of the most important aspect of graphene is the massless Dirac fermions. These Dirac fermions travel with the speed of 10^6 m/s [8]. Graphene plays a vital role for promising applications in field effect transistors, optoelectronics, sensors and flexible devices [9–12]. The charge carriers of graphene can travel thousands of interatomic distances without scattering so it also can be used for ballistics devices [8, 13].

The main cause for interest in graphene is it's unique nature of charge carriers (mimic of relativistic particles). The charge carrier concentrations can be tuned between electrons and holes due to ambipolar electric field effect as shown in Fig. 1.1 and their mobilities can surpass $15000 \text{ cm}^2\text{V}^{-1}\text{s}^{-1}$ even at room temperature. But its carrier mobility depends on temperature (independent between 10 K and 100 K). Mobility degrades at room temperature due to unintentional impurity scattering and it can be improved upto $\sim 100,000 \text{ cm}^2\text{V}^{-1}\text{s}^{-1}$ [14]. Graphene always has low conductance value even after vanishing of charge carrier concentrations near the Dirac point [8].

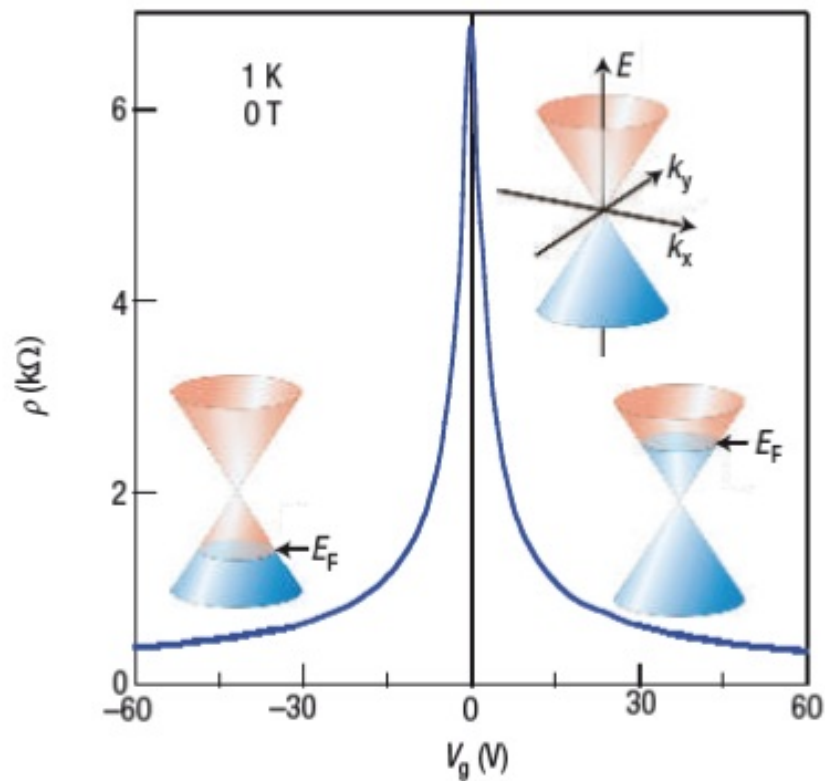


Fig. 1.1. Ambipolar electric field effect in monolayer graphene. Resistivity as a function of gate voltage, resistivity decreases rapidly with gate voltage and this indicates high carrier mobility. This Fig. is adapted from reference [14].

In 2004, AK Geim and Novoselov reported that graphene can be produced by mechanical exfoliation of Highly Oriented Pyrolytic Graphite (HOPG) using scotch tape. Graphene monolayer can be identified on 300 nm SiO₂ using optical microscope [15]. Various research groups reported that large scale production of graphene sheets can be achieved by Chemical Vapor Deposition (CVD) method for practical applications. CVD graphene has been produced on metal substrates (Cu, Ni and Pt) at high temperature (800-1000°C) in a mixture of CH₄, hydrogen and argon [16]. Other chemical methods of graphene production are reduction of graphite oxide and unzipping of carbon nanotubes [17].

Graphene transistors have insufficient on/off current ratio due to zero bandgap of graphene. Bandgap can be opened in graphene by confinement of charge carriers by creating nanostructures like graphene nanoribbons [18] and quantum dots with lateral confinement [19], and by applying edge distortions and electric field effect in bilayer graphene [20, 21]. In case of Graphene Nanoribbons (GNRs), the energy bandgap is

inversely proportional to the nanoribbon width [22]. GNR's electronic properties are distinct from graphene as it shows metallic as well as semiconducting behavior depending on the edge structure (zigzag or armchair) and width of ribbons [23]. Armchair and zigzag edges of GNR are shown in Fig. 1.2.

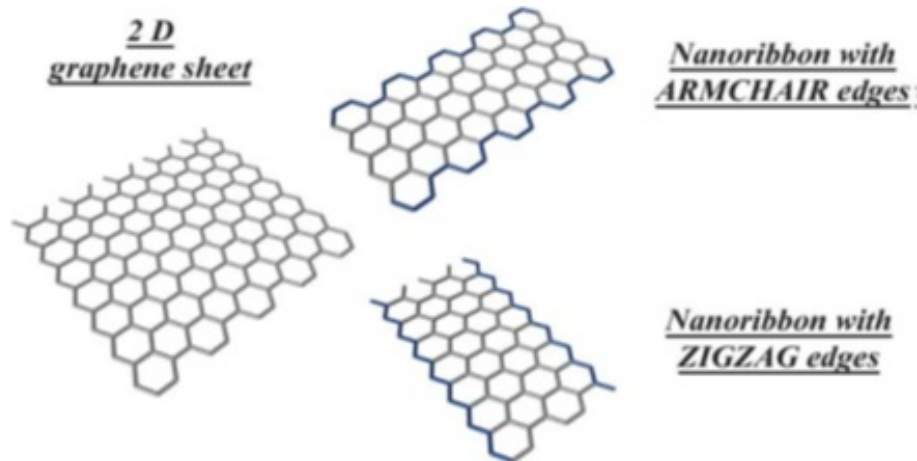


Fig. 1.2. Armchair and zigzag edges in GNR. Nanoribbon edge structure determine the electronic structure. This Fig. is adapted from reference [24].

The bandgap opening in graphene nanoribbons has already been verified theoretically and experimentally, as shown in Fig. 1.3 [18, 25–27]. The bandgap of 200 meV is extracted experimentally in width < 20 nm graphene nanoribbons [18]. The rough edges, edge configuration, edge functionalization and doping affect the bandgap [28, 29]. The perfect edged nanoribbon is not ideal for electronic applications due to low mobility. Larger opening of bandgap create parabolic curvature around the Dirac point which enhance the effective mass of charge carriers [30] and it probably decrease the mobility. Experimentally extracted GNR mobilities are about $200 \text{ cm}^2\text{V}^{-1}\text{s}^{-1}$ in 1-10 nm wide nanoribbons [18, 31] and $1100 \text{ cm}^2\text{V}^{-1}\text{s}^{-1}$ in 18 nm width nanoribbons [32]. Mobility of $1500 \text{ cm}^2\text{V}^{-1}\text{s}^{-1}$ have been verified in 14 nm width nanoribbons by the theoretical calculations [33]. We need highly smooth crystalline edges of nanoribbons for high on/off ratio transistors with high mobility. High on/off ratio with high mobility in graphene nanoribbon transistors would enhance speed of devices.

Fracture in graphene is a severe concern for graphene's applications which arise during graphene processing like graphene transfer, chemical processing and during fabrication of graphene transistors, and high bias measurements [34, 35]. Fracture of graphene is a prominent issue for graphene based devices as graphene has low fracture toughness

(16 J/m²) in spite of high mechanical strength [36]. In device fabrication process, graphene breaks down due to breakage of carbon-carbon bonds and wrinkles appear during transfer process [37]. Another reason of graphene breakage is the lower friction force (0.36 - 0.62 nN) than Si surface (1.1 - 4.3 nN) [38]. CVD growth of poly-crystalline graphene [39] and sonication of carbon nanotubes [40] induce inevitable cracks, grain boundaries and defects in graphene. Thus healing or reconstruction of graphene is essential for applications of graphene devices.

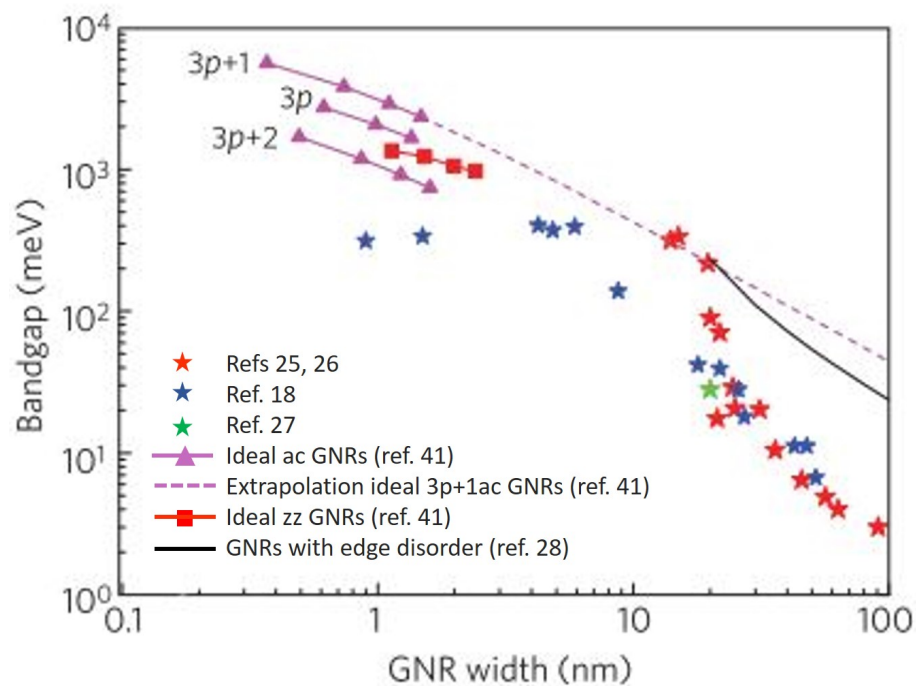


Fig. 1.3. Bandgap as a function of nanoribbon width from experiments [25] [26] [18] [27] and calculations [41] [28].

1.1 Scope of the Present Work

Different synthesis methods have been deployed for production of regular smooth edges and narrow GNRs. Top down methods like Scanning Tunneling Microscopy (STM) lithography [42], anodic oxidation by Atomic Force Microscopy (AFM) [43], unzipping of Carbon Nanotubes (CNTs) by strong acid treatment [44], and patterning of graphene by Electron Beam Lithography (EBL) [45] damage the GNRs and edges of GNRs. Thus bottom-up approaches like chemical synthesis [46] and metal catalyzed anisotropic etch-

ing using Ni, Fe, Cu [47] have been explored for fabrication of GNRs with smooth and achiral edges. But transition metal Pt has not been explored yet for GNR synthesis. In this work, Pt is used for production of crystalline smooth edged GNRs. Pt has higher carbon solubility and high misfit factor than other metals (Ni, Fe, Cu) which is required for etching of graphene. Thus Pt is more suitable transition metal than other metals (Ni, Fe, Cu) for etching of graphene. Our objective is the fabrication of highly smooth edged graphene nanoribbons for field-effect transistor applications and Pt nanoparticles-assisted etching produce the crystalline edged GNRs.

In literature, graphene is reconstructed using sophisticated and expensive Transmission Electron Microscopy - Scanning Tunneling Microscopy (TEM-STM) tool via e-beam irradiation [48]. Carbon Nanotubes (CNTs) are healed by e-beam irradiation in Scanning Electron Microscope (SEM) tool. But thermal treatment of fractured graphene in methane gas for reconstruction is not explored yet which is a feasible and cost-effective method than e-beam irradiation method. In this work, we have explored the inverse process of metal catalyzed CVD growth for etching of graphene for fabrication of GNRs. Another objective of this work is to develop a catalyst free process using CH_4 for healing of fractured graphene.

1.2 Thesis Organization

This thesis contains six chapters including introduction as the first chapter. Other chapters are organized in the following manner.

Chapter 2 gives a brief literature review on graphene and graphene nanoribbons. Structure and type of graphene nanoribbon edges is discussed. The bandgap engineering of graphene and graphene nanoribbons are explored. Literature review on fabrication methods of graphene nanoribbons and their transport properties are presented. Healing of CNTs by e-beam irradiation in SEM and joining of graphene layers by e-beam in TEM are reviewed briefly.

Chapter 3 describes physical and electrical characterization techniques used in this thesis. Overview of physical characterization techniques, namely optical microscopy, Raman spectroscopy and AFM for identification of graphene and GNRs are provided. Electron-beam lithography Raith 150 Two is used for device fabrication. Specifications

and process steps of lithography are provided. The metal deposition technique of sputtering and the semiconductor device analyzer which is used for electrical characterization are also described.

In chapter 4, synthesis of graphene nanoribbons by metal-assisted etching and fabrication of bottom gated GNR transistor are described. Physical and electrical characteristics of GNRs are studied in detail. Our results are benchmarked to those presented in the literature.

In Chapter 5, causes for fracture of graphene and reconstruction methods of fractured graphene are discussed. Validation of reconstruction of graphene by e-beam irradiation and methane gas treatment are given by physical and electrical characterization techniques. We argue that the methane gas treatment method is superior to e-beam irradiation method for reconstruction of broken graphene.

In chapter 6, thesis is summarized with future directions.

Chapter 2

Literature Review

2.1 Introduction to Graphene

Graphene is a 2D high crystalline material consisting of monolayer of carbon atoms. Graphene is the building block of many carbon materials in all dimensionalities like 0D (zero dimensional) buckyball, 1D (one dimensional) nanotubes and 3D (three dimensional) stack of graphene sheets (Fig. 2.1) [14].

The electronic properties of all materials are described by Schrodinger equations in condensed matter physics but in the exceptional case of graphene, it is described by the Dirac equation. Dirac equation describes the electronic transport, scalability of graphene devices to nanodimensions and various forms of graphene [49]. The honeycomb crystal structure of graphene is made of hexagonal arrangement of carbon atoms. The honeycomb crystal structure and Brillouine zone of graphene are shown in Fig. 2.2 [50]. In graphene, carbon has sp^2 hybridization, one σ bond and two π bonds, one is π (full of electrons that is called valance band) and another is π^* (empty band that is called conduction band). These two bands touch each other at Brillouin zone corner and create zero bandgap as shown in Fig. 2.3. It shows semimetal behavior (where conduction and valance band degenerate at Dirac point in Brillouin zone) and have symmetrical linear dispersion relation ($E = \hbar v_f k$) between electronic energy E and wave vector k . Here $v_f = 10^6 \text{ ms}^{-1}$ is the effective speed of light [51].

Graphene has excellent electronic properties which makes it a potential candidate for high speed analog applications. But for switching applications, we need a bandgap and that can be created by quantum confinement in graphene. The quantum confinement

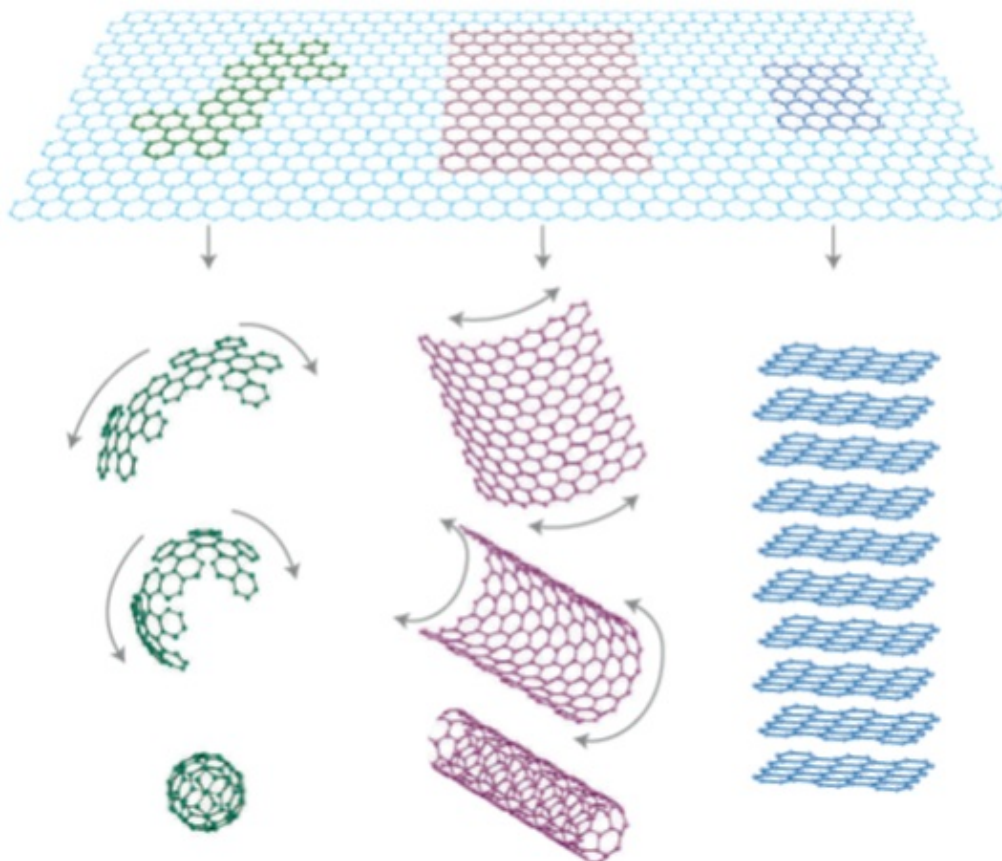


Fig. 2.1. Graphene is the building block of other graphitic materials in other dimensionalities. Graphene can be fold into 0D buckyballs, wrapped-up into 1D nanotubes and make 3D graphite (stack of layers). This Fig. is adapted from reference [14].

of charge carriers in 1D graphene nanoribbons induce transport gap and it depends on the width of graphene nanoribbons and crystallographic orientation of edges. Graphene nanoribbon energy gap is inversely proportional to the width. GNRs possess two types of achiral edges, armchair and zigzag that is determined by hexagon orientation of nanoribbon length which is shown in Fig. 2.4(a) [52]. Both the edges have different chemical reactivity and properties. Only zigzag edges have spin transport properties. Chiral angle θ and chiral vector (n,m) represent the GNR chirality as shown in Fig. 2.4(b) [53]. Graphene edges after mechanical exfoliation also have crystalline zigzag and armchair edges that has been validated by scanning electron micrograph which is shown in Fig. 2.5.

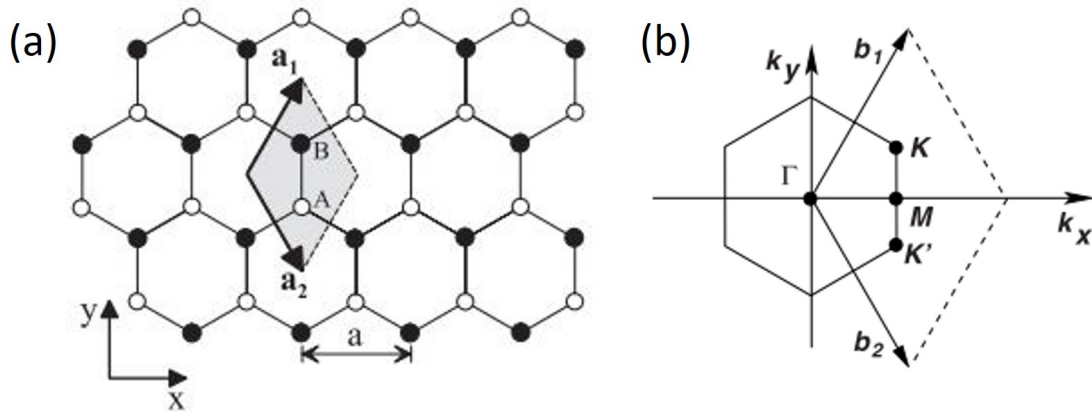


Fig. 2.2. (a) Crystal structure of monolayer graphene with two atoms (A and B). The shaded rhombus region represents unit cell of graphene, \mathbf{a}_1 and \mathbf{a}_2 are the primitive lattice vectors. (b) The Brillouine zone of graphene with two Dirac points K and K'. This Fig. is adapted from reference [50].

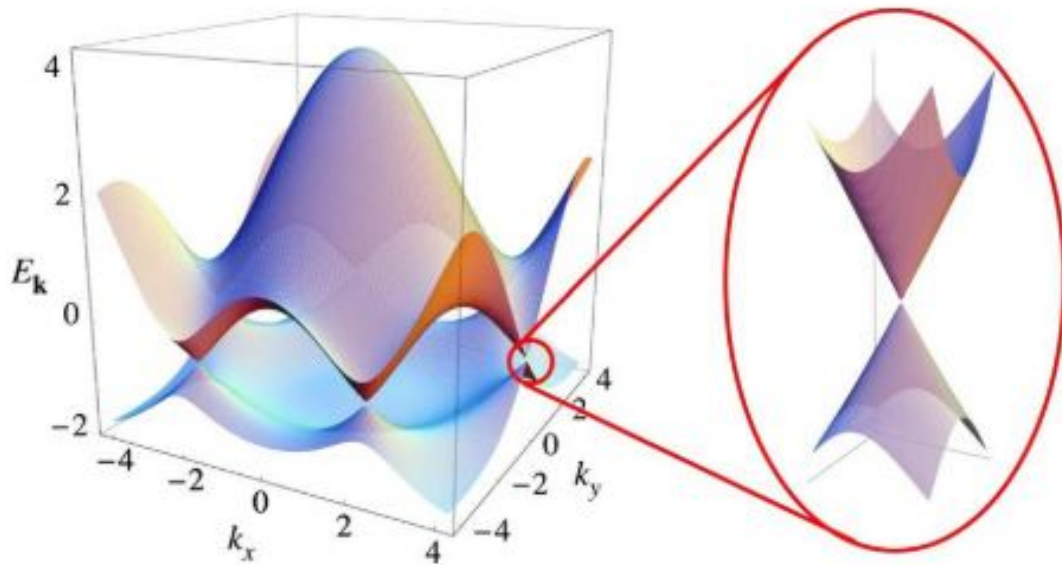


Fig. 2.3. Electronic dispersion in the honeycomb lattice. Left: energy spectrum of graphene calculated by tight binding approach. Right: zoom-in of valance and conduction band which is showing one Dirac point. This Fig. is adapted from reference [51].

2.2 Band Gap Engineering

GNR's electronic band structure can be tailored by width and chirality (crystallographic orientation) of nanoribbons. Ab-initio theory or calculations demonstrate that the energy

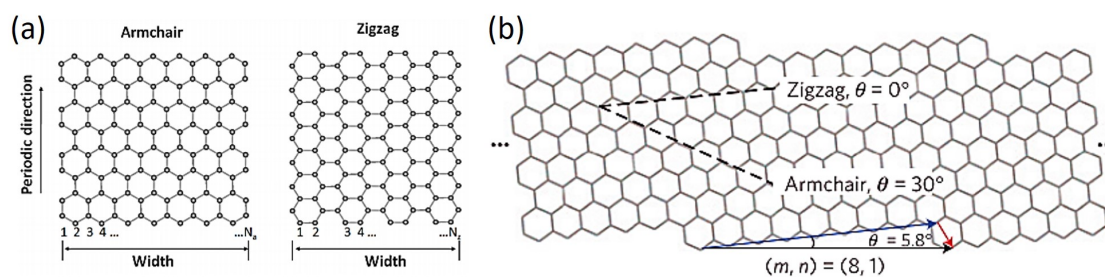


Fig. 2.4. (a) Armchair and Zigzag Nanoribbons. N_a and N_z are the number of dimer lines across armchair and zigzag ribbon width [52]. (b) Schematic drawing of (8,1) GNR. The chiral vector (n,m) connecting crystallographically equivalent sites along the edge defines the edge orientation of the GNR (black arrow). The blue and red arrows are the projections of the $(8, 1)$ vector onto the basis vectors of the graphene lattice. This Fig. is adapted from reference [53].

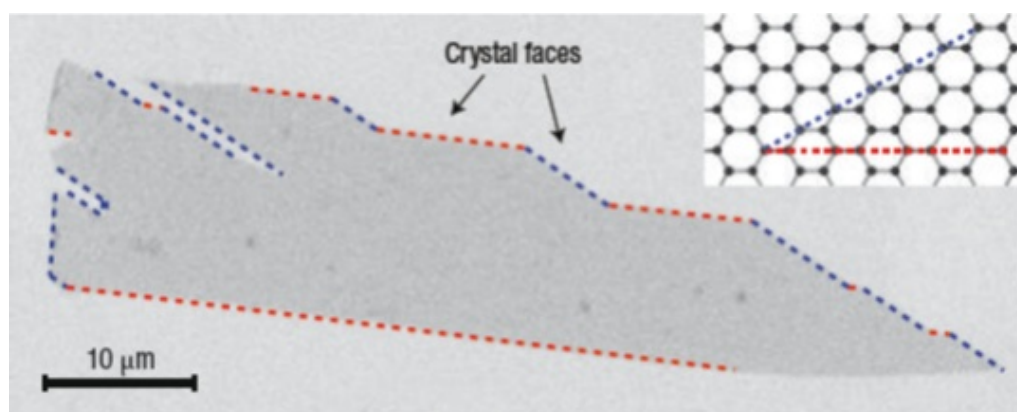


Fig. 2.5. Scanning electron micrograph of a large graphene, which shows that most of the monolayer faces are zigzag and armchair edges, as indicated by blue and red lines represented. This Fig. is adapted from reference [8].

gaps in the armchair arise due to quantum confinement and edge effects [22]. In the zigzag edges, bandgap arise due to edge magnetization [54]. The arm chair GNRs can be metallic or semiconducting that is determined by its width but zigzag always shows metallic behavior. But in both cases, GNR's width must be in nanometers for bandgap opening. Hydrogen passivated GNRs edges (arm-chair and zigzag) always have direct and nonzero bandgap [22].

2.2.1 Theoretical Predictions

Many theoretical calculations have been devoted to the study of electronic properties of armchair and zigzag GNRs. The tight-binding approach [55], Density Functional Theory (DFT) calculation [22, 56] and first principle approximation [22] have been applied for the estimation of bandgap in armchair and zigzag nanoribbons. According to first principle calculations, in armchair nanoribbons, bandgap is induced due to quantum confinement effect and increment of hopping integral between the π orbitals of the edge atoms due to changes in the atomic bonding lengths [22]. In zigzag nanoribbons, bandgap arise due to a staggered sublattice potential from magnetic ordering of edge states [54]. Zigzag edged nanoribbons also have direct bandgap which is inversly proportional to ribbon width. Zigzag nanoribbons have a peculiar edge-state structure near Fermi level without considering spins. Edge chirality and width of GNR play important role in determining the electronic properties of GNRs.

Graphene nanoribbon chirality describe the orientation of the GNRs edges with respect to the crystalline lattice of graphene [55]. It is defined by the chirality angle θ . Armchair and zigzag high-symmetry directions are directly related to the angles $\theta = 30^\circ$ and $\theta = 0^\circ$ respectively, although all intermediate θ values correspond to chiral directions. GNR band structure (tight-binding structure) also depends on chirality angle θ . As θ increases, two Dirac cones of graphene approach each other onto 1D Brillouin zone of GNR. The density of edge states is reduced due to decrease of length in momentum space of flat edge-state band (connecting the two Dirac points) that is shown in Fig. 2.6(a) for the special case of $\theta = 19.1^\circ$ (chiral zigzag GNR) [57]. The density of edge states is defined by the magnetic moment per edge unit length which is shown in Fig. 2.6(b). Density of edge states per unit length is given by equation 2.1 [58].

$$n(\theta) = \frac{2}{3a} \cos \left(\theta + \frac{\pi}{3} \right) \quad (2.1)$$

Here a is the lattice constant. In armchair GNRs, edge orientation $\theta = 30^\circ$ reserves the equivalence of the two sublattices of the bipartite lattice of graphene. Amchair GNR edge states disappear in this case according to equation 2.1. All armchair GNR shows either metallic or semiconducting behavior at the Dirac point [55].

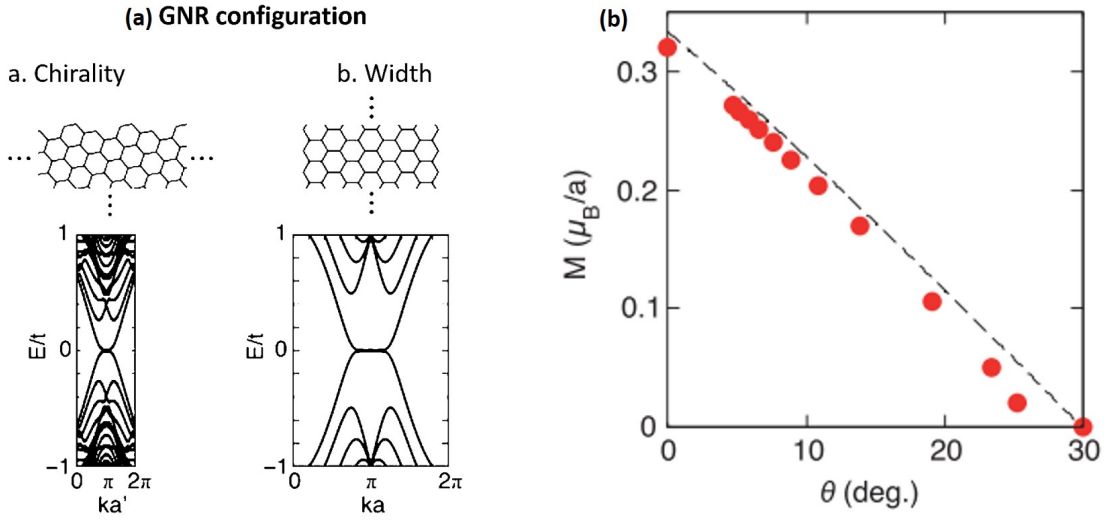


Fig. 2.6. (a) Basic electronic band structure of zigzag GNR calculated using tight-binding model. GNR configurations depend on chirality and ribbon width. (b) Magnetic moment per edge unit length M versus chirality angle θ for 7-nm-wide GNRs that is calculated using the mean-field Hubbard model at $U/t = 1$ (Red circles). Here U and t represent Coulomb repulsion and hopping integrals respectively. The dashed black line corresponds to the edge-state density, $n(\theta)$ in the limit of infinite width. This Fig. is adapted from reference [55].

As GNR width decreases, it creates more spacing between sub-bands because of quantum confinement but does not affect the edge-state band (Fig. 2.6(a)) [22]. Armchair GNRs are classified into two categories on the basis of tight-binding electronic structure: (a) metallic if $N = 3P + 2$ (N is the number of pairs of atoms per GNR unit cell, P is a positive integer value) and (b) semiconducting if $N = 3P + 1$ or $3P$ [59, 60]. Graphene nanoribbon width and bandgaps can be calculated by using first principle calculations [42]. Graphene nanoribbon width is given by

$$W = \frac{\sqrt{3}(N-1)}{2} * a_{c-c} \quad (2.2)$$

Where $a_{c-c} \sim 1.42 \text{ \AA}$ is the carbon-carbon bond length. Bandgap as a function of ribbon width of three armchair families is shown in Fig. 2.7(a) which is calculated using tight-binding approximation [22]. Zigzag edged nanoribbons show metallic behavior with peculiar edge states. By using Local Density Approximation (LDA), the bandgap Δ^0

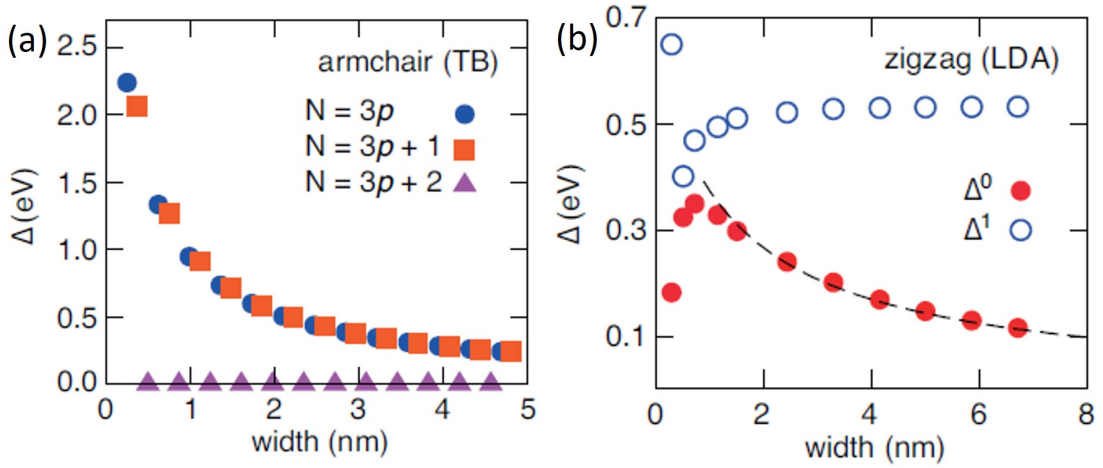


Fig. 2.7. (a) Band gap of armchair GNRs versus GNR width (calculated using the tight-binding approach). (b) Band gaps Δ^0 and zone-boundary splittings Δ^1 of the spin-polarized ground states of zigzag GNRs as a function of width based on local density approximation. This Fig. is adapted from references [22, 55].

and zone-boundary splitting Δ^1 of zigzag edged GNRs (spin-polarized ground states) are calculated as a function of ribbon width as shown in Fig. 2.7(b) [22].

$$E_{g,3P} = \Delta_{3P}^0 - \frac{8\delta t}{3P+1} \sin^2\left(\frac{P\pi}{3P+1}\right) \quad (2.3)$$

$$E_{g,3P+1} = \Delta_{3P+1}^0 + \frac{8\delta t}{3P+2} \sin^2\left(\frac{(P+1)\pi}{3P+2}\right) \quad (2.4)$$

$$E_{g,3P+2} = \Delta_{3P+2}^0 - \frac{2|\delta|t}{P+1} \quad (2.5)$$

where

$$\Delta_{3P}^0 = t\left(4\cos\left(\frac{P\pi}{3P+1}\right) - 2\right), \quad \Delta_{3P+1}^0 = t\left(2 - 4\cos\left(\frac{(P+1)\pi}{3P+2}\right)\right), \quad \Delta_{3P+2}^0 = 0, \quad t = 2.7\text{eV}, \quad \delta = 0.12$$

$$E_g^{\text{zigzag}}(\text{eV}) = \frac{9.33}{W(A^0) + 15} \quad (2.6)$$

Electronic structure of graphene nanoribbons is described by edge configurations, edge chirality and confinement width. All these parameters should be considered for determination of electronic and magnetic properties of GNRs.

2.2.2 Experimental Progress

The experimental realization of nanoribbons has been already demonstrated [18, 22, 25, 27, 31, 61, 62] which provides validation of theoretical predictions of nanoribbon's electronic and magnetic properties. In graphene nanoribbon transistors, on/off current ratio can be improved by tuning the bandgap [18]. Bandgap can be tuned by varying the width of graphene nanoribbons or lateral constriction of charge carriers in graphene [18, 22, 25]. High on/off ratio (upto 10^6) is already reported in narrow width of GNRs [18, 31]. Another approach for opening the bandgap is to break the inversion symmetry in bilayer graphene by applying external electric field normal to graphene plane [61]. By using this approach, bilayer graphene FETs were reported with on/off current ratio of 100 at room temperature [61]. Yu et al. combined both of the above strategies to achieve on/off current ratio up to 3000 at room temperature by applying a vertical electric field and lateral constriction of charge carriers in bilayer graphene [21]. Vertical electric field induce a finite bandgap (~ 400 meV) in bilayer graphene by moving conduction band upwards and valance band downwards near Dirac point. This bandgap is estimated from equation 2.7.

$$I_{on}/I_{off} \propto \exp(E_g/k_B T) \quad (2.7)$$

Where bandgap $E_g = 2q\phi_{barrier}$ and $\phi_{barrier}$ is the Schottky barrier height at the contacts, T is the temperature and k_B is the Boltzmann constant [21].

Li et al. also extracted bandgap values from equation 2.7 in chemically derived ultrasmooth nanoribbons, and fitted into empirical form of E_g (eV) = $0.8 / [W$ (nm)], where W is the width of GNR [18]. Bandgap values are consistent with the expressions which concludes that on/off ratio increases exponentially as ribbon width decreases. The experimental bandgap values follows the theoretical calculation of armchair and zigzag nanoribbons which is shown in Fig. 2.8. Precise quantitative comparison of experimental data with theoretical data is difficult because the edge structure of nanoribbon, i.e. whether they are zigzag/armchair or mixed edged nanoribbons, is usually not specified [18]. Carrier mobility is lower in nanoribbon transistors compared to graphene transistors. For accurate estimation of carrier mobility, precise nanoribbon width, edge structure and gate capacitance determination and ohmic contacts to nanoribbons are required [63–65].

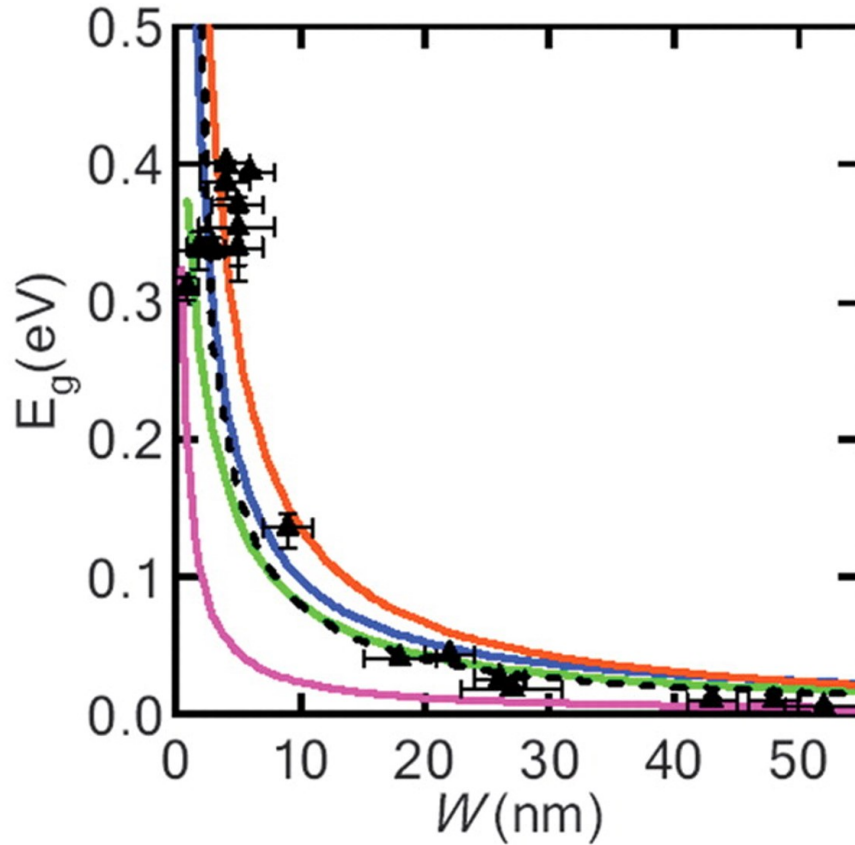


Fig. 2.8. Extracted bandgap values of GNR as a function of ribbon width. Symbol represents experimental data. The black dotted line is the experimental data in empirical form E_g (eV) = $0.8 / [W$ (nm)]. The purple, orange and blue solid lines show the bandgap dependence on width for three armchair families, extracted using first principle calculations. Green solid lines represents zigzag edged nanoribbons, extracted using local density approximation. This Fig. is adapted from reference [18,22].

2.3 Graphene Nanoribbon Synthesis Methods

Different graphene nanoribbon synthesis methods have been reported in the literature. Narrow and smooth graphene nanoribbons are synthesized by various methods and Field Effect Transistors (FETs) have been fabricated on all these GNRs. Bandgap, mobility and on/off ratio of these GNRs are reported in detail which we will review in this section.

2.3.1 GNR Fabrication by Lithography Technique

Lithography (mainly electron Beam Lithography) based patterning technique can be used for fabrication of narrow nanoribbons. But their large scale production by this

method is limited because of low throughput. CVD grown graphene [62] and epitaxial graphene on SiC [66] can be used for synthesis of GNRs. In 2007, Chen et al. fabricated 20 nm GNR FETs with 30 meV bandgap and they also reported that the minimum conductivity and transport properties are affected by boundary scattering and trapped charges in the substrate [27]. Hwang et al. used wafer scale CVD grown graphene for fabrication of back-gated GNR FETs by lithography technique and observed 0.1 eV bandgap opening by using differential conductance method [62]. In this GNR fabrication method, CVD graphene was transferred on 90 nm $\text{SiO}_2/\text{p}^+\text{Si}$ substrate. Hydrogen silsesquioxane (HSQ) e-beam resist was used for fabrication of 12 nm GNRs. Electron-beam evaporator was used for deposition of contact metals Cr/Au (5/100 nm). Schematic of back-gated device structure is shown in Fig. 2.9. HSQ was not removed from graphene as shown in Fig. 2.9(b).

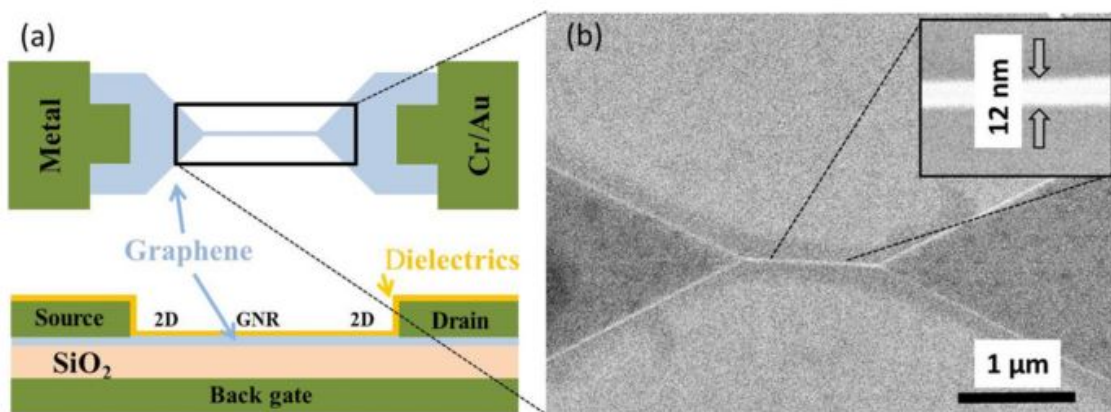


Fig. 2.9. (a) Schematic of back-gated nanoribbon transistor. (b) Scanning Electron Microscopy (SEM) image of the 12 nm nanoribbon, magnified view of nanoribbon is shown in inset. This Fig. is adapted from reference [62].

Electrical characteristics were measured in vacuum from room temperature to 4 K. Drain current as a function of gate voltage for 12 nm ribbon at different temperature is shown in Fig. 2.10(a). On/off current ratio is increased from 10 (at 300 K) to 10^6 (at 4 K) which indicates strong temperature dependency of transport gap [62]. This gate modulation behavior is quite distinct from graphene FET which does not show any gate modulation even at low temperature due to zero bandgap [27, 67]. A significant gate modulation is shown at low V_{DS} by varying gate voltage which appears due to shifting

of Fermi level. At low temperature, tunneling current is more dominant than thermionic emission current [62].

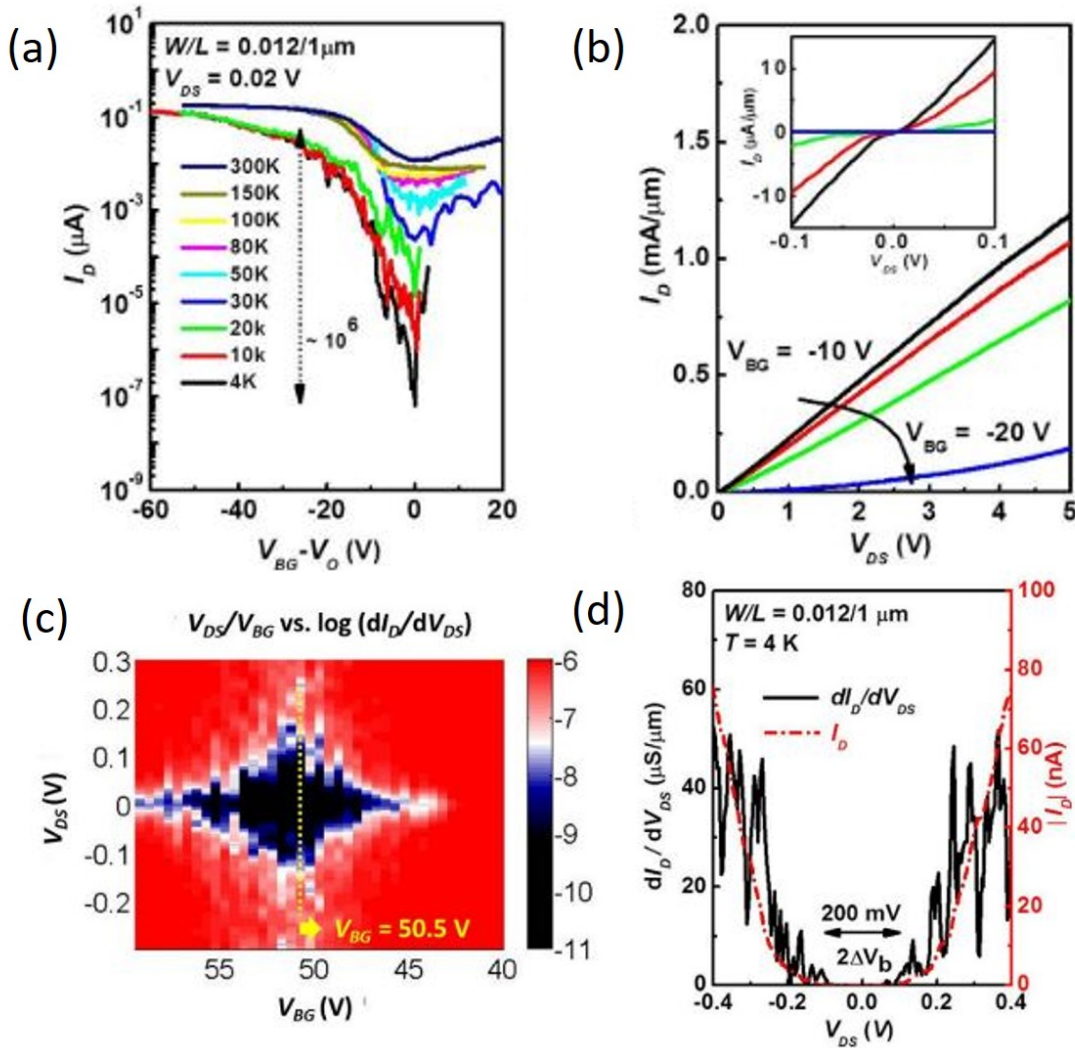


Fig. 2.10. (a) Transport characteristics of 12 nm wide back-gated GNR FET at various temperatures. (b) Output characteristics at 4 K. (c) Differential conductance map of a 12 nm GNR FET as a function of V_{DS} and V_{BG} at 4K. (d) Differential conductance and absolute drain current v/s V_{DS} at V_G 50.5 V. This Fig. is adapted from reference [62].

The quantum confinement in armchair nanoribbons create bandgap that is estimated by $E_g \sim 2\pi\hbar v_f/3W$, here $v_f \sim 10^8$ cm/s is the Fermi velocity which characterize the conical bandstructure of graphene and \hbar is the Planck's constant and W is the width of GNR [68]. For 12 nm width of GNR, $E_g \approx 0.1$ eV. Differential conductance map of GNR FET is shown in Fig. 2.10(c) as a function of V_{DS} and V_{BG} at 4 K. In this map, black and red color signify low and high conductance respectively. GNR gap is shown by dark diamond

shape. The extracted bandgap from differential conductance map is 0.1 eV which is close to that predicted by the theoretical model [68]. Recent study on nanoribbons describes that transport gap arise from hopping between localized states in nanoribbons [69]. This transport gap is an indication of change in density of states by quantum confinement. The differential conductance is proportional to density of states at low temperature and it gives 0.1 eV bandgap that can be deduced from Fig. 2.10(d) [62].

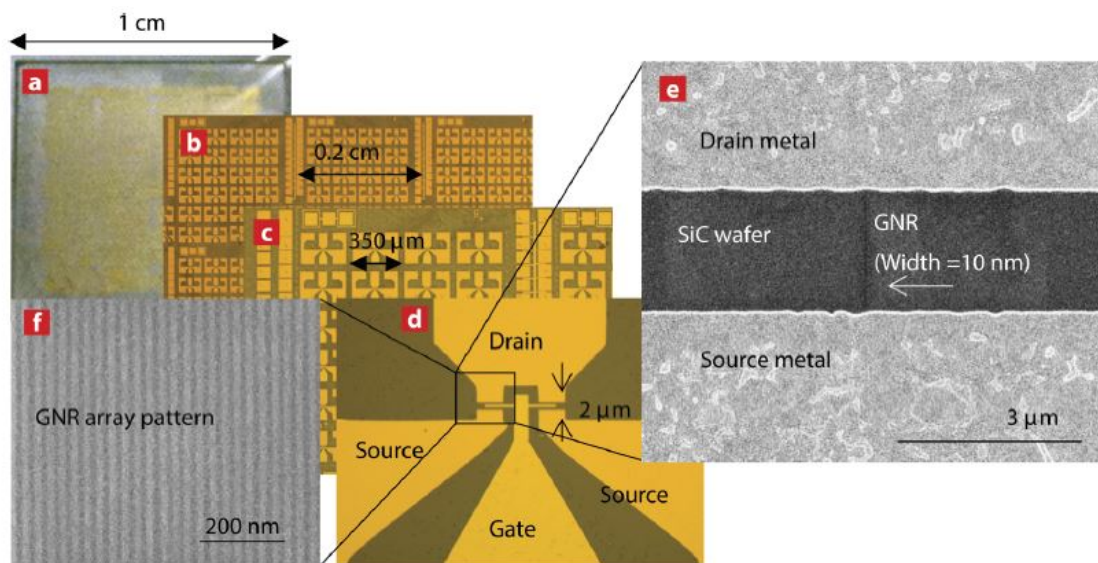


Fig. 2.11. (a)-(d) Optical images of epitaxial nanoribbon transistors on wafer size SiC substrate. (e) SEM image of GNR having 10 nm width with source and drain contact metal. (f) SEM image of HSQ array ribbon patterns, consisting of 13 nm GNR line width and 17 nm space, showing no deformation or collapse. HSQ was used as a mask to etch graphene during O_2 plasma etch process. This Fig. is adapted from reference [66].

Epitaxial GNRs on SiC substrate were achieved by nanowire template method [66,70]. Sprinkle et al. fabricated GNRs using photolithography and O_2 RIE etching [70]. In this work, the extracted mobility for 40 nm GNR was $2700 \text{ cm}^2\text{V}^{-1}\text{s}^{-1}$ and on/off ratio was 10 at room temperature but substantial energy gap was not calculated [70]. To correlate the experimentally measured transport properties with theoretical model of epitaxial GNRs, ~ 10 nm GNRs were patterned on large area epitaxial graphene on SiC by e-beam lithography [66]. The extracted bandgap was ~ 0.14 eV. Epitaxial graphene on SiC substrate has less residual charges than transferred CVD graphene [71,72]. Negative e-beam resist HSQ was used for patterning of sub-10 nm and ~ 10 nm GNRs. Top gate transistors were fabricated by e-beam lithography. Top gate dielectric of 30 nm Al_2O_3

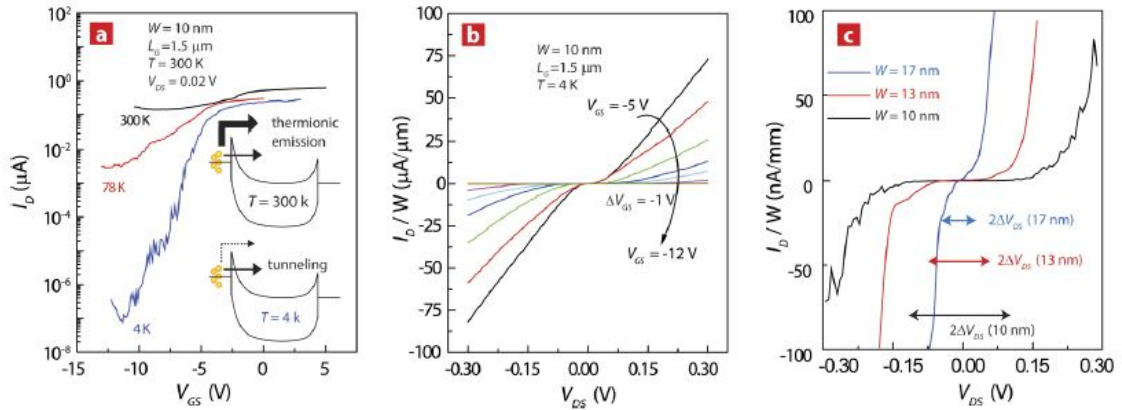


Fig. 2.12. (a) Drain Current as a function of gate voltage for 10 nm GNR FET at various temperatures. I_D is dominated by thermionic emission at 300 K and suppressed at 4 K. Band-to-band tunneling dominate at 4 K. (b) I_D versus V_{DS} at different V_{GS} showing clear on-off states. (c) I_D versus V_{DS} with fixed V_{GS} for different GNR width at 4 K. This Fig. is adapted from reference [66].

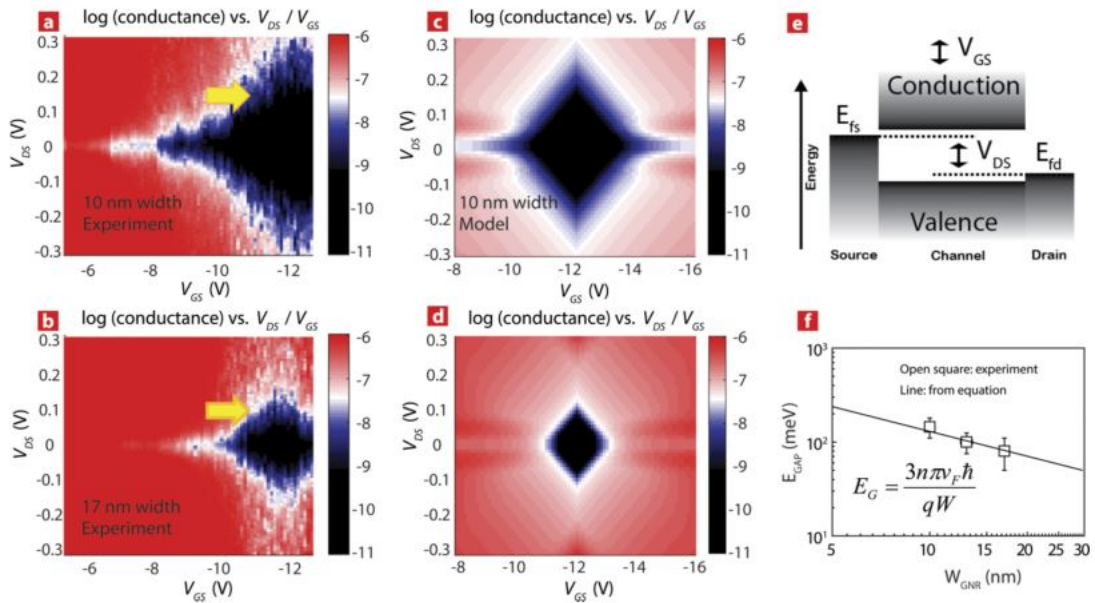


Fig. 2.13. The differential conductance map as a function of V_{DS} and V_{GS} of GNR width 10 nm (c) and 17 nm (d) are shown in (a) and (b) at 4 K respectively. Red and black color indicate high and low conductance in the map. (e) Energy band diagram model is based on the Schottky barrier. (f) Extracted band gap of GNR FET vs. width of GNR. The linear line was fitted using the energy band diagram model. This Fig. is adapted from reference [66].

and source-drain contact metals (Cr/Au-5/100 nm) were deposited by Atomic Layer Deposition (ALD) and electron-beam evaporation respectively. Device structure is shown in Fig. 2.11. Electrical characteristic of 10 nm GNR FET shows higher on/off ratio at 4 K in comparison of room temperature as shown in Fig. 2.12(a). Fig. 2.12(b) shows clear on-off states. Fig. 2.12(c) shows that as ribbon width decreases, low conductance window increases. Differential conductance map is a more comprehensive approach for quantitative measurement of bandgap. Conductance map as a function of V_{DS} and V_{GS} of two GNR FETs of width 10 nm and 17 nm are shown in Fig. 2.13. Red and black color show high (on-state) and low conductance (off-state) respectively, in the logarithmic scale map. In Fig. 2.13(a), at fixed drain voltage, transition from conducting to insulating state are observed in the $-8 \text{ V} < V_{GS} < -6 \text{ V}$ region. Schottky behavior of nanoribbon is observed in Fig. 2.13(a) and (b) after varying drain bias at fixed gate voltage. This concludes that GNR FET channel is like a traditional semiconductor with a substantial bandgap. Precise bandgap can be extracted by modeling of differential conductance map using transport equation of conventional semiconductor which also includes thermionic emission and tunneling current parameters [66].

Large number of similar width nanoribbons can be fabricated by lithographic technique but edge geometry and edge roughness can't be determined by lithography. To study more quantitatively GNR FET behavior, edge roughness and edge geometry must be known. Thus other synthesis methods are explored for fabrication of GNRs for digital applications.

2.3.2 GNRs by Unzipping of Carbon Nanotubes

Previous reports demonstrate that GNRs can be synthesized by unzipping of carbon nanotubes as CNTs have nanometer range of diameters [17, 33, 73]. In 2009, Jiao et. al developed a method of fabrication of GNRs by controlled unzipping of CNTs in longitudinal direction by plasma etching process. Schematic of production of GNRs from CNTs is described in Fig. 2.14. These GNRs have smooth edges and 10-20 nm width distribution [17]. Bottom gated GNR FETs were fabricated with Pd metal contacts (channel length $< 250 \text{ nm}$) [17]. These GNR FETs show p-type behavior because of O_2 physisorption from ambient. GNR FET with $\sim 16 \text{ nm}$ and $\sim 7 \text{ nm}$ widths have been reported. GNR transistor of $\sim 7 \text{ nm}$ nanoribbon shows on/off ratio > 100 (Fig. 2.15). GNR with 16 nm

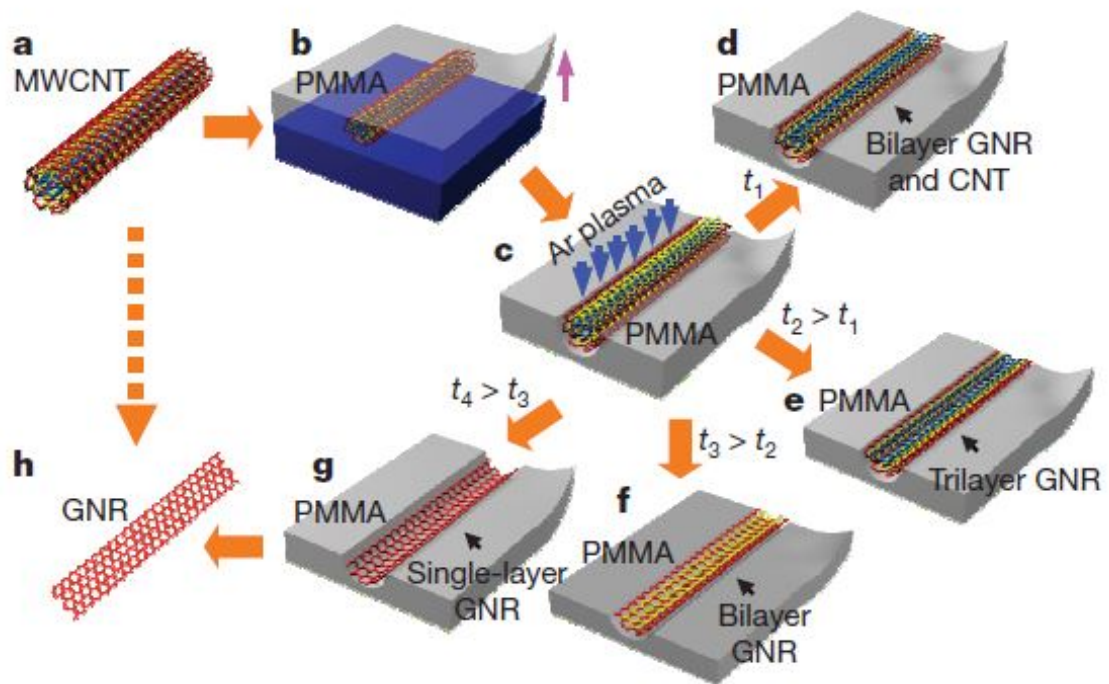


Fig. 2.14. Schematic of GNRs production from CNTs. (a) A pristine Multi Wall Carbon Nanotube (MWCNT) was used as the starting raw material. (b) Poly Methyl Methacrylate (PMMA) resist were coated on MWCNT/Si substrate. (c) PMMA-MWCNT film was peeled from the Si substrate, turned over and then exposed to an Ar plasma. (d-g) Etching time was varied: GNRs with CNT cores were obtained after etching for a short time t_1 - (d) tri-, bi- and single-layer GNRs were produced after etching for times t_2 , t_3 and t_4 , respectively ($t_4 > t_3 > t_2 > t_1$; e-g). (h) PMMA was stripped from nanoribbons. This Fig. is adapted from reference [17].

width shows weak gate modulation due to smaller bandgap. $I_{ds}-V_{gs}$ curve of GNR shows symmetric behavior of electron and hole transport that is similar to graphene. Estimated resistivity at Dirac point for 10-20 nm GNR FETs were 10-40 k Ω , similar to lithographically patterned GNRs. Mobilities of these GNR devices were 10 times lower than 2D graphene sheets because of edge scattering [17].

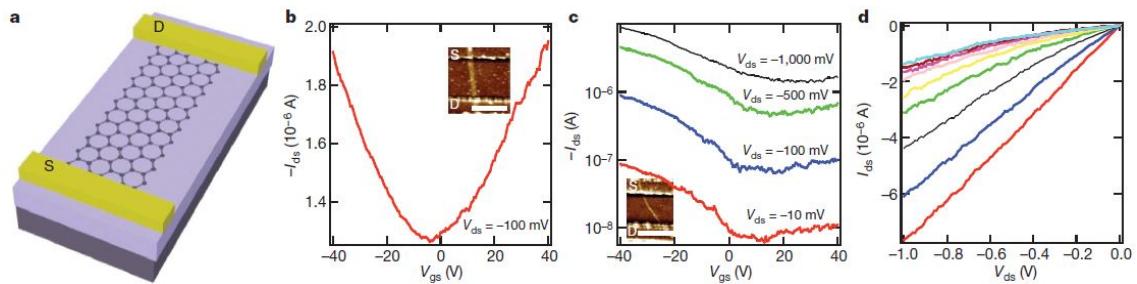


Fig. 2.15. (a) A schematic of GNR device. (b) Transfer characteristic of 16-nm-wide GNR device probed in vacuum after electrical annealing. Dirac point is located near $V_{gs} = 50$ V. Inset shows the AFM image of this device; scale bar is 200 nm. (c) I_{ds} - V_{gs} curves for 7-nm-wide GNR device at various biases probed in air. The on/off ratio is 10 for this device. (d) I_{ds} - V_{ds} curves for the device in (c) at gate biases V_{gs} ranging from 240 V (bottom) to 40 V (top) in steps of 10 V. This Fig. is adapted from reference [17].

2.3.3 GNRs Fabrication by Atomic Force Microscopy, Scanning Probe Lithography and Focused Ion-Beam Etching Techniques

GNRs fabrication have been demonstrated using Scanning Probe Lithography (SPL) [42], Atomic Force Microscopy (AFM) [43] and Focused Ion Beam (FIB) etching [74] techniques. In AFM technique, AFM tip cut the graphene by anodic oxidation process and produce GNRs [43]. SPL also can be used for fabrication of GNRs due to high resolution and chirality determination [42]. SPL fulfills all the need of GNRs like narrow width distribution, crystallographic orientation and minimum edge disorder. SPL has advantage over AFM, because in AFM, water meniscus (present nearby AFM tip (10-20 nm radius) induce oxidation in channel and has poor resolution. SPL has been used on transferred graphene on gold substrate [42]. Gold is a conductive and non-oxidative material and hence it is commonly used as a substrate for SPL. 100 mV bias voltage and 500 pA tunneling current parameters were used for imaging of 4.6 nm and 2.5 nm GNRs which is shown in Fig. 2.16(a) [42]. Y. Zhang et al. fabricated 20 nm GNR arrays by using focused ion beam (FIB) etching technique (Fig. 2.16(b)) [74]. Ga^+ ions were used for patterning of graphene for fabrication of GNRs. AFM, STM and FIB etching techniques can be used for fabrication of different width of GNRs but these techniques are time consuming and also can't be used at large scale.

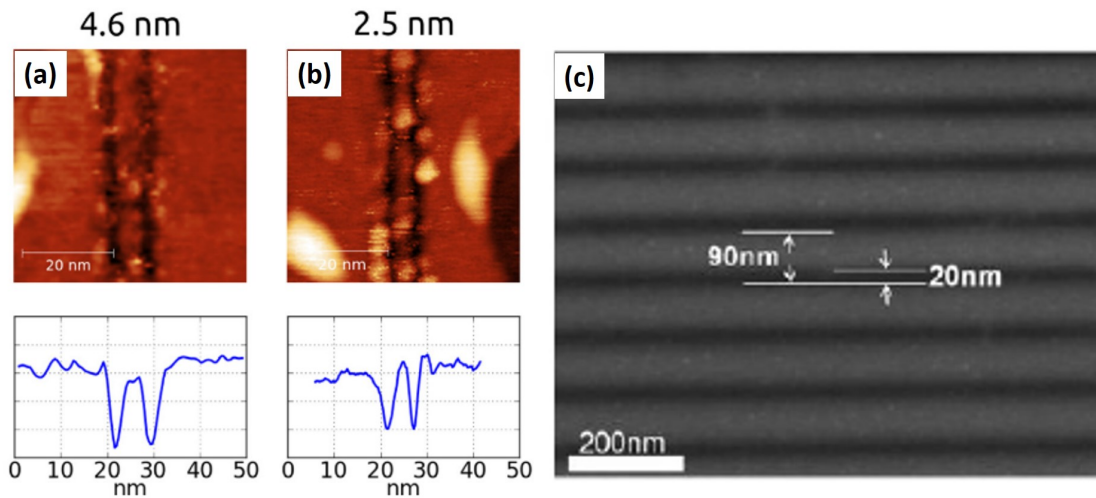


Fig. 2.16. (a,b) GNR cut in the zigzag direction with various width (4.6 and 2.5 nm) by SPL. Height profile of GNR is shown below figure (a) and (b) [42]. (c) 20 nm large arrays of GNRs by using FIB etching technique. This Fig. is adapted from reference [74].

2.3.4 Chemically Derived GNRs

Atomic structure of GNRs have been fabricated via bottom up chemical synthesis approach. In this approach, arm-chair GNRs ($N = 7$) were synthesized on epitaxial Au/mica substrate [75]. Thermal annealing of 10,10'-dibromo-9,9'-bianthryl monomers at 200°C make a linear polymer (polyanthrylene chain) and after that cyclodehydrogenation of polymer at 400°C produce $N = 7$ GNRs. Polyanthrylene height is approximately 0.85 nm. $N = 7$ ($N =$ linear row of atoms) armchair GNR shows 1.6 eV bandgap and $N = 9$ and 11 create smaller bandgap than $N = 7$. These narrow width (below 1 nm) and atomically smooth GNRs have desirable electronic properties. Bennett et al. fabricated GNR field effect transistors and the unique transport characteristics of sub-1 nm width GNRs were studied [59]. GNRs were transferred on SiO_2 substrate for device fabrication. First, PMMA was spin coated onto GNRs to make PMMA/GNR/Au/Mica stack. Concentrated hydrofluoric acid and Au etchant were used to delaminate mica and Au film. GNRs with PMMA resist were transferred on SiO_2 after DI water rinsing and resist was removed using acetone.

Bennett et al. fabricated three terminal devices with 10-15 nm average channel length using e-beam lithography (Fig.2.17(a)). Source and drain contact pads (Pd) were patterned in two steps (first- 30 nm, second- 10 nm) by optical lithography and e-beam

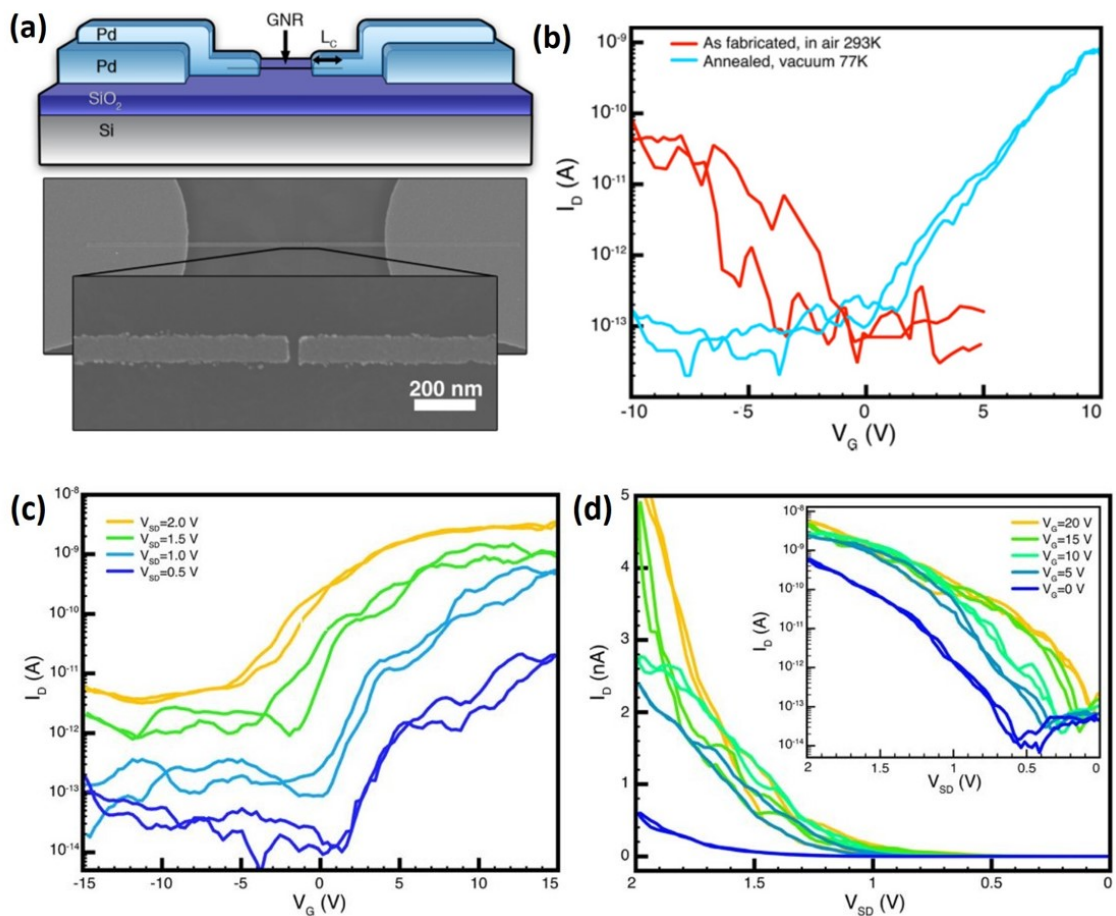


Fig. 2.17. (a) Schematic of device geometry. Below: SEM of the device is showing 100 nm wide contact pad with a 26 nm source drain gap. (b) Transport characteristic of a device at $V_{SD} = 1$ V in both air and under vacuum at 77 K. (c) Electrical characterization of a typical device post passivation, under vacuum, at 77 K. I_D as a function of gate bias at different V_{SD} . (d) Output characteristics at different gate bias, inset: same data presented in logarithmic scale. This Fig. is adapted from reference [59].

evaporation. Electrical characteristics were measured at 300 K and 77 K. 20-30 nm channel length devices show gate-modulated conductance (on current range - 10s of pA to few nA at 1 V V_{SD}). On-current range is low due to random orientation and position of GNRs [59]. I_D as a function of V_G shows p-type behavior in air ambient due to water, oxygen adsorption and PMMA residue on the contact and GNR [76, 77]. After vacuum annealing (300° C at 10^{-7} Torr), the molecular desorption curtailed contact metal work function that switch the device behavior from p-type to n-type and reduced the hysteresis effect (Fig. 2.17(b)) [78]. Another observed device was a short channel Schottky barrier device with 26 nm channel length. Gate modulation at 77 K of transport characteristic

and source-drain bias behavior are shown in Fig. 2.17(c and d). This device shows on/off ratio of 3.6×10^3 at $V_{SD} = 1$ V. Here, off current or leakage current is induced by tunneling of holes across the drain barrier which is strongly V_{SD} dependent (at larger V_{SD} , Schottky barrier width will decrease). Thus at larger drain bias, enhanced electric field induce tunneling through barriers that generate field emission which control the current flow. This effect increases on-current exponentially. It was concluded that Schottky barrier series resistance is much higher than the nanoribbon channel resistance. On/off ratio can be improved by using lower metal contact work function and via increasing the drain barrier [59].

2.3.5 Metal-Assisted Etched GNRs

Metal-assisted etching of graphene has been reported by using transition metals (Fe, Cu, Ni) [47]. These metals are used as a catalyst in the etching process which shows that etching of graphene depends on catalytic activity of metal nanoparticles. Ni has higher catalytic activity than Fe and Cu, as Ni has strong interaction with graphene. Similarly Cu has low melting temperature (1100°C) and low carbon solubility (catalytic order- Ni>Fe>Cu). These catalytic metal nanoparticles create both zigzag and armchair edges. Etching process has been employed on different substrates in Ar/H₂ environment at high temperature. Etching density and quality of GNRs are shown to be depend on type of substrate, H₂ concentration and etching temperature [47]. Campos et al. described that anisotropic etching of graphene by Ni nanoparticles at 1000°C preserve the chirality angles of 60° and 120° that have same crystallographic orientation (either armchair or zigzag) and 90° and 150° have different crystallographic orientation with respect to different edge chirality [79]. Chirality angle of etching is shown in Fig. 2.18. Quality of graphene does not change after etching as it was confirmed by Raman spectroscopy [79, 80].

Anisotropic etching is also subjected to substrate type like crystalline a-plane and r-planes of sapphire, ST-cut (ST = Stable, Temperature) quartz and SiO₂ [47]. Both planes of sapphire have crystalline surface and high degree of anisotropy so probability of anisotropic etching is high in this substrate rather in ST - cut quartz and SiO₂. Etching of graphene occurs in the same crystallographic direction of sapphire substrate at high temperature in 15% H₂/Ar ambient. For etching process, too low (7.5%) and too high

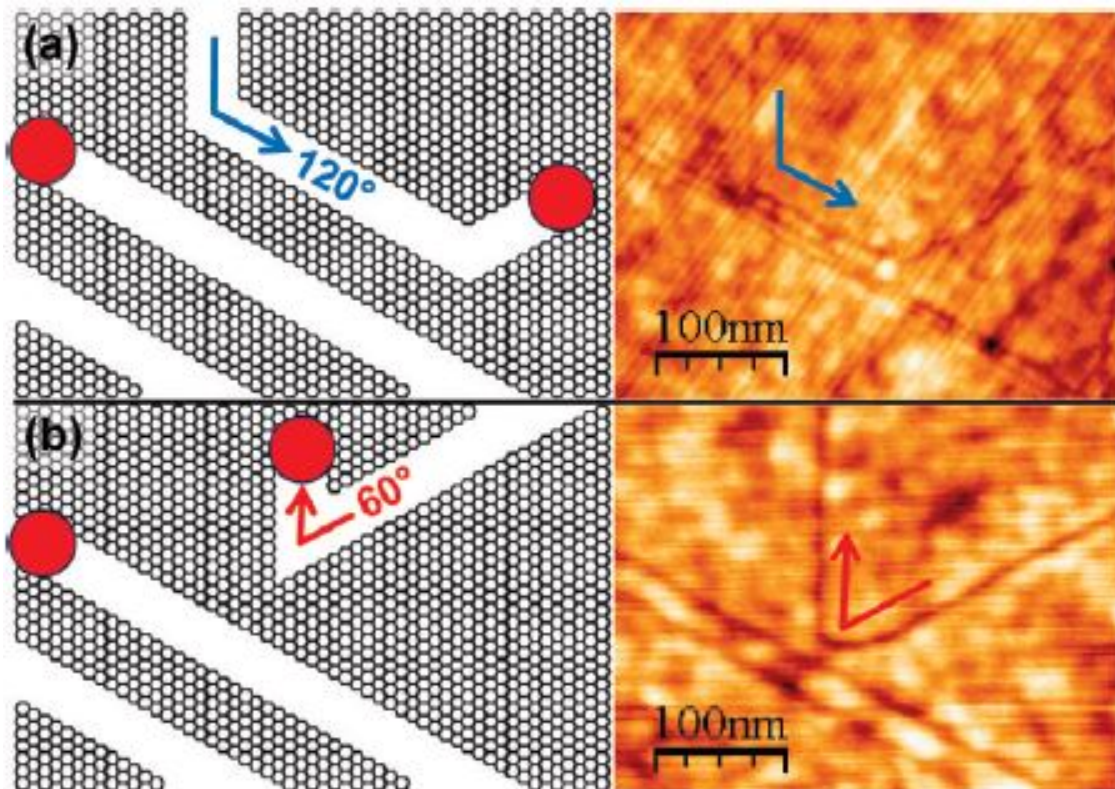


Fig. 2.18. (a) Left : schematic of GNR structures that shows 120° angle of trench by nanoparticles. Ni nanoparticles are denoted by red circles. Right : AFM images of GNR with 120° angle of trench. (b) Left : schematic of GNR structures that shows 60° angle of trench. Right : AFM images of GNR with 60° angle of trench. This Fig. is adapted from reference [79].

(50%) H_2 concentration are not suitable because too low concentration of hydrogen is insufficient for etching and too high concentration of hydrogen etch more graphene. 15% hydrogen was sufficient for etching of graphene to make GNRs. High etching density was observed at 1050°C for Ni nanoparticles which was higher than etching density at 1000°C and 1100°C for Ni nanoparticles. Etching density by Ni nanoparticles observed was 25 lines/ μm and average nanoribbon width was 25 nm [47].

Etched graphene were transferred on SiO_2 substrate for fabrication of bottom-gated multichannel devices [47, 60]. GNR arrays were patterned by EBL and remaining graphene were removed by oxygen plasma [60]. Source and drain electrodes (Cr/Au) were deposited by thermal evaporation. Electrical properties of etched GNRs were measured at room temperature in vacuum (8×10^{-4} Pa). Devices with low etching density area show low on/off ratio of $\sim 2-4$ and it depends on etching density. High etching

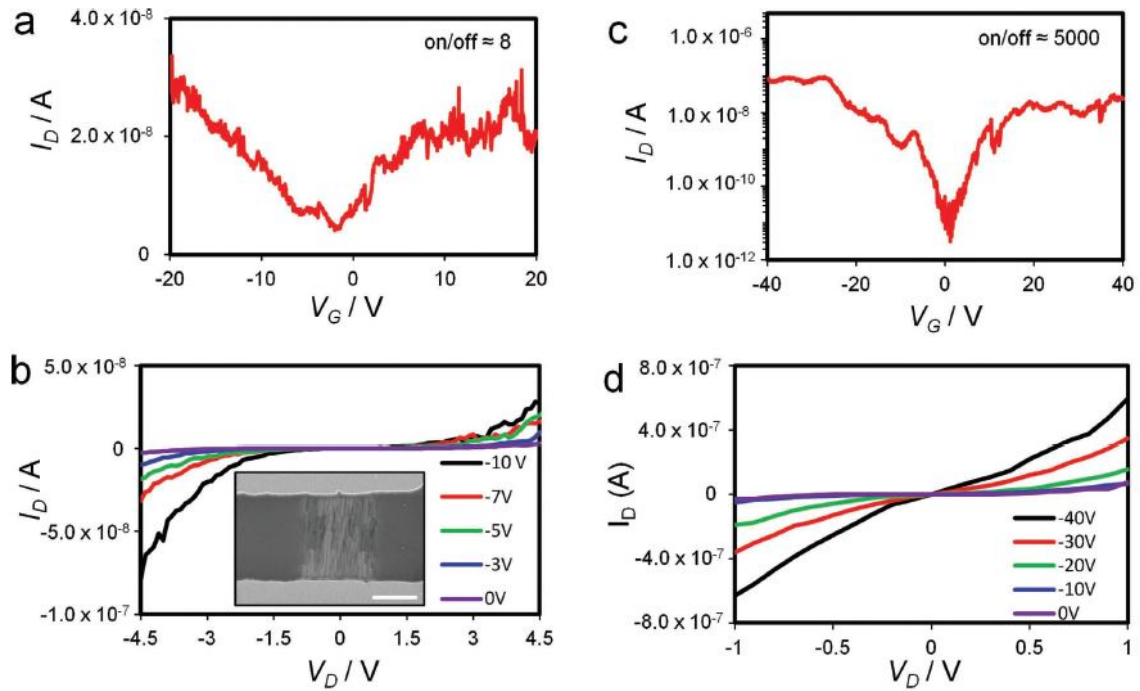


Fig. 2.19. (a) Transport characteristic and b) Output characteristics of optimum etched nanoribbon area. SEM image of device is shown in inset of figure (b) with $1 \mu\text{m}$ scale bar. (c) Transport and (d) Output characteristics of high etched density area of nanoribbons. This Fig. is adapted form reference [60].

density area gives slightly higher on/off ratio than less density etched area. On/off ratio is ~ 7 - 10 for optimum etched area (average ribbon width $\sim 19.3 \text{ nm}$) which is shown in Fig. 2.19(a). These characteristic values are slightly lower than previously reported lithographically patterned GNRs (half width of metal-assisted etched GNRs). This is the indication of good quality of GNRs by metal-assisted etching. High etching density area shows larger on/off ratio ~ 5000 that is shown in Fig. 2.19(c). Graphene nanoribbon width variation is the cause of high on/off ratio in some area and it concludes that these nanoribbons make a chain of quantum dots which induce a bandgap due to the Coulomb blockade effects [60]. Device performance can be improved by producing narrow width GNRs with smooth edges by metal assisted etching.

2.4 Reconstruction of Carbon Nanotubes, Graphene and Graphene Nanoribbons

Graphene's severe concern is the electrical breakdown or fracture of graphene which is a potential threat for practical applications of graphene. Fracture arises due to low fracture toughness (16 J/m^2) [36] even though graphene has ultra high mechanical strength 130 GPa and 1TPa Young's modulus [5]. Fracture of graphene is a pronounced issue due to brittle nature of graphene and inevitable flaws viz. holes, dislocations [39] and cracks which appears during fabrication of graphene devices [81]. Crack behaviours like crack speed [82] and crack propagation directions [83] have been investigated theoretically and experimentally but very few progress has been demonstrated on healing of cracks [84–86]. In literature, different types of fracture like irradiation fracture [87], chemical fracture [88], impact fracture [89], sonication fracture [40] and dynamic fracture [89] have been reported on the basis of theoretical calculations and experiments. Another reason of fracture or breakdown in graphene is the electrical stress of devices [90]. Thus reconstruction or healing of fractured graphene is essential for nanoelectronics applications. In this section, we will discuss healing of CNTs by e-beam irradiation and developments on reconstruction of graphene/GNRs.

2.4.1 Reconstruction of Graphene by High Energy Electrons in TEM

Experimental and theoretical work on reconstruction of graphene edges and joining of individual graphene sheets have been already reported [48, 85]. Reconstruction of graphene edges and joining of individual graphene sheets are achieved by in-situ Joule heating of GNRs in integrated Transmission Electron Microscope - Scanning Tunneling Microscope (TEM-STM) system [85]. Reconstruction of GNR edges by Joule heating process is shown in Fig. 2.20. Joule heating and e-beam irradiation vaporize the carbon atoms at GNR edges which crystallizes the defect edges to atomically smooth edges after annealing. According to modeling calculations, Joule heating or annealing process gives point defect annealing and edge reconstruction [85]. In Joule heating process, different voltages have been applied on defective GNR edges. Lower voltage ($<1.6 \text{ V}$) vaporize

the carbon atoms because of knock-on effects by electron beam irradiation [91]. Higher voltage (>1.6 V) give reconstruction-crystallization effects due to high temperature that is caused by Joule annealing. Joule annealing effect creates armchair and zigzag edges which has higher activation energy than other edge configurations [85]. The mixture of armchair and zigzag edges has metastable state due to energy penalty at the edge junctions which causes irregularity. Current flow and atomic vibrations are obtained due to Joule heating process. As a result, initial Joule heating gives point (localized) defects which are concomitant with large amplitude vibrations [85].

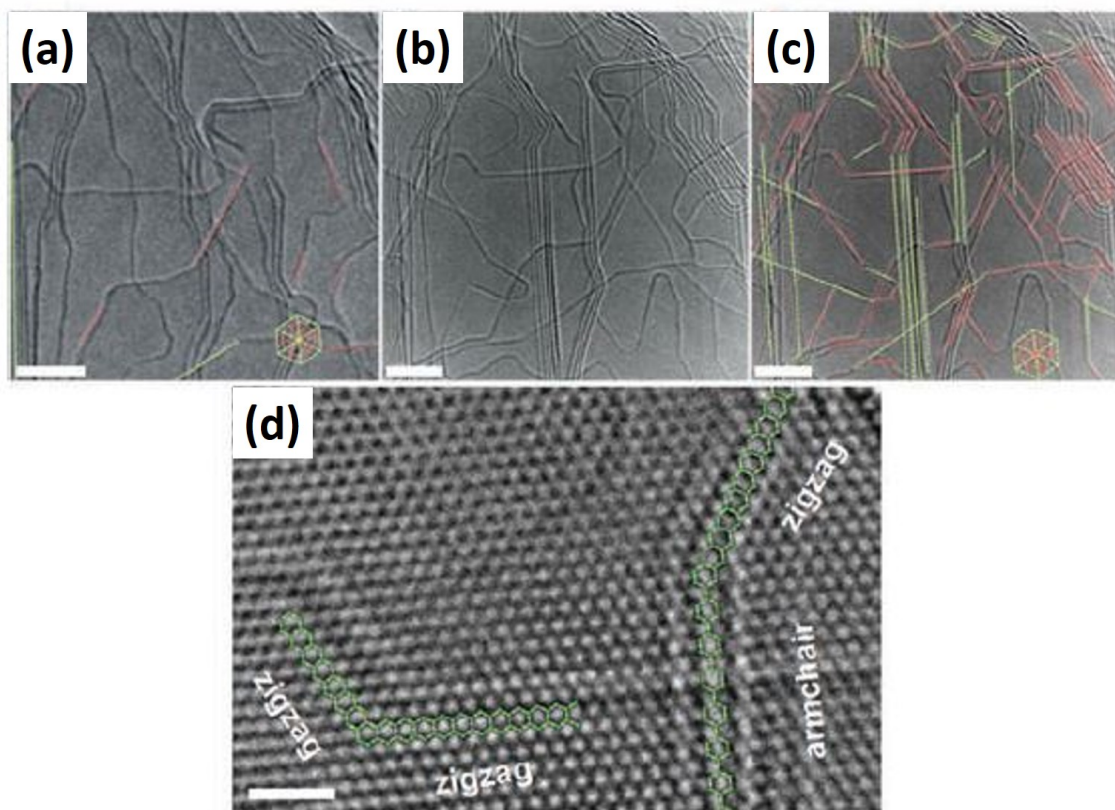


Fig. 2.20. (a) Graphene nanoribbons show very few zigzag (pink lines) and armchair edges (green lines) before Joule heating. (b, c) GNRs after 10 min. Joule heating at 1.6 V. Most of the edges are either zigzag or armchair edges, as shown in figure (c). (d) High-magnified view of the annealed sample is showing zigzag-armchair and zigzag-zigzag edges. Scale bars in (a), (b) and (c), 4 nm; in (F), 1 nm. This Fig. is adapted from reference [85].

Electronic states in zigzag edges are localized along their edges because of large electronic dispersion, induce current flow along zigzag edges in GNRs [23]. Very few

and longer length armchair edged GNRs are obtained by the nonlocal transformation mechanism. Zigzag edges are initially produced at high temperature because of localized mechanism. Molecular dynamic simulations explain that carbon atoms from armchair edges evaporates faster than zigzag edges because dissociation energy of C-C is lesser in armchair edges (6.7 eV) than zigzag edges (11 eV) [85].

Zou et al. demonstrate joining of individual graphene sheets (single and multilayer) in a TEM-STM holder inside a 200 KV field emission TEM [48]. Graphene sheets have been joined in "top-to-top" and "layer-to-layer" geometries by applying a voltage. "Top-to-top" layer geometry provides seamless joining. Joined graphene sheets have same electrical and mechanical properties similar to original graphene sheets. "Top-to-top" geometry of joining of graphene sheets fulfills the requirement of micro and nanodevices like desired parameters shape, size and configurations. Joining process of graphene sheets is shown by schematic diagram in Fig. 2.21 [48].

Due to high chemical activation energy of zigzag/armchair edges [92], graphene edges are reconstructed and assembled simultaneously. Dangling bonds are activated by operating electron energy and rearranged the carbon atoms in hexagon rings and in pentagon-heptagon pair. [51]. Seamless joining of graphene sheets has three steps: (1) local deformation and activation of dangling bonds at the edges due to current annealing, (2) new covalent bond formation between carbon atoms at the activated edges, and (3) rearranging the carbon networks for new graphene sheet edge formation. Graphene sheets were not fully damaged during this process that was confirmed by TEM images. After reconstruction of graphene sheets, electrical properties are similar to original graphene sheets. Both joining geometries of graphene sheets are shown in Fig. 2.22 [48].

Joining of graphene layers depends on the applied voltage because very low voltage is insufficient for activation of dangling bonds and high voltage remove all the carbon atoms rapidly from the graphene edges and it creates defects also. "Top-to-top" geometry needs lower activation energy than "layer-to-layer" geometry for joining of graphene sheets. "Layer-to-layer" joining needs higher activation energy for formation of hexagonal rings or pentagon-heptagon pairs in vertical carbon network which is higher than carbon atoms evaporation. As a result, shrinkage, demolition and evaporation of carbon atoms occur before rearrangements of carbon atoms (to form hexagonal rings or pentagon-heptagon pairs) in graphene layers. So "top-to-top" geometry is excellent for joining of

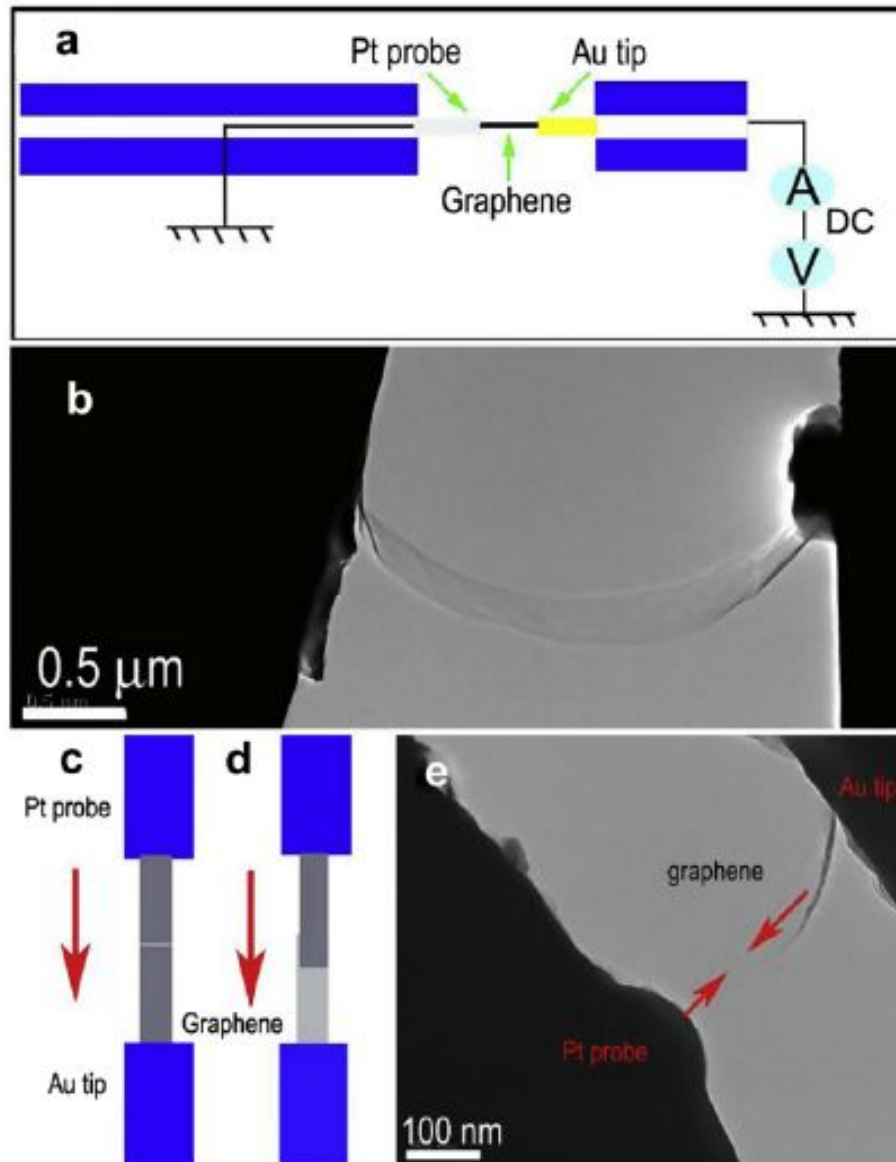


Fig. 2.21. (a) Schematic diagram of experimental setup for measurement of electrical properties of graphene in the TEM-STM holder. (b) TEM image of a monolayer graphene with Pt probe and Au tip. (c, d) Schematic picture of "top-to-top" and "layer-to-layer" joining geometries of graphene sheets. (e) TEM image showing the practical manipulation of a graphene sheet. This Fig. is adapted from reference [48].

graphene sheets rather than "layer-to-layer" geometry [48]. This has future implications on graphene applications like flexible devices, touch screen, LEDs and solar cells.

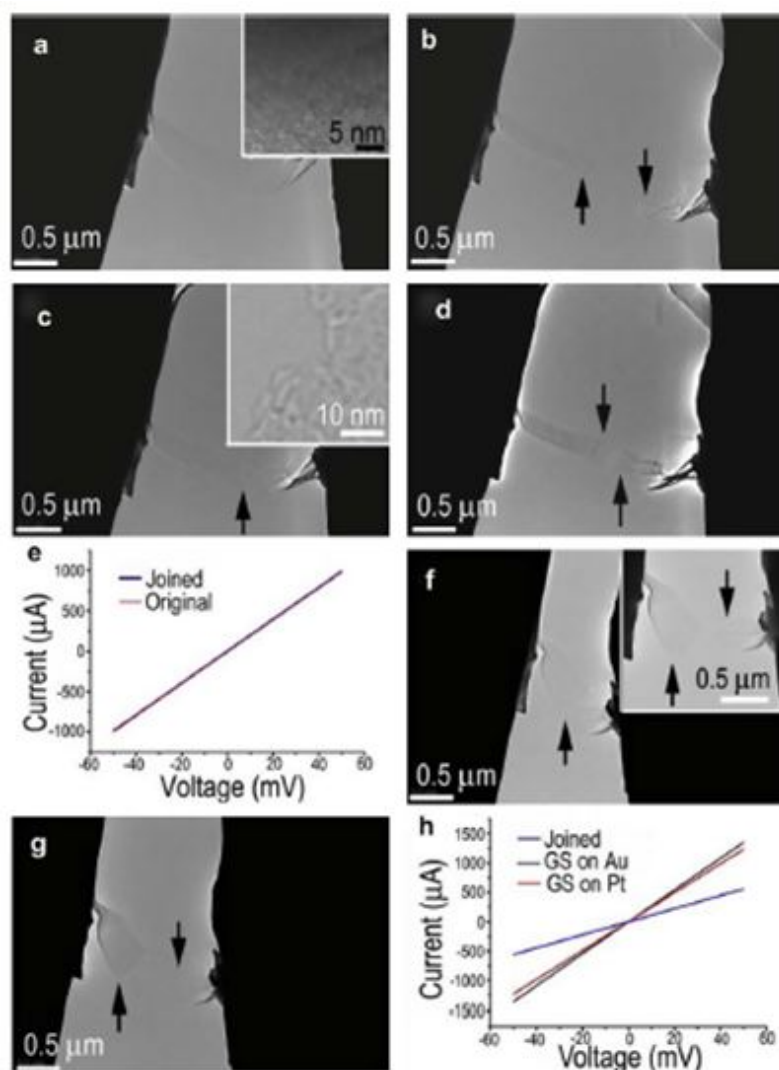


Fig. 2.22. Joining of individual single layer graphene with both joining geometries: (a) Graphene monolayer with Pt probe and Au tip. Inset is showing High Resolution Transmission Electron Microscopy (HRTEM) image of monolayer. (b) Two segments of graphene layer after applying a voltage. (c) "Top-to-top" joining geometry. (d) Same graphene sheet after cracks due to high applied voltage. (e) I-V characteristic of original and joined graphene layer. (f) "Layer-to layer" joining geometry. (g) Same joined graphene layer was broken again due to high biasing and in situ pulling process. (h) I-V characteristic of joined graphene layer and graphene layer at the Pt probe and Au tip respectively. This Fig. is adapted from reference [48].

2.4.2 Healing of Carbon Nanotubes by Low Energy Electrons in Scanning Electron Microscopy System

Carbon nanotubes as on-chip interconnects have extensive application in ultrafast nanoelectronic circuits because of high current carrying capacity (10^8 A/cm²) and high electrical conductivity [93, 94]. But Joule heating limits this property because of breakdown of tube after certain high voltages [95–97]. Healing of cracked tubes by e-beam irradiation has been reported in literature [98, 99].

Broken tubes were repaired by using low energy electrons (3-10 keV) in scanning electron microscope (SEM) system [98]. High energy electron beam (100-200 keV) and high energy ions (MeV) irradiation induce amorphization, kinking, bending, cutting or deformation in tubes [100–102] and damage the tubes [91]. Advanced, complex and expensive TEM system is needed for production of high energy electron beam and for high resolution. From application point of view, SEM is an easy and more feasible approach for joining of broken nanotubes rather than TEM. In SEM, mechanical manipulator is not required and ex-situ electrical measurement of irradiated CNTs can be performed. Kulshrestha et al. performed the electrical measurement before and after electrical joining of carbon nanotubes by using 3-10 keV in SEM [98]. Carbon nanotubes were broken after applying high voltage due to Joule heating effect. These broken tubes were repaired by applying 10 keV at broken sites of tubes for 2-5 mins. After rejoining of CNTs, current was less significant than pre-broken tube (Fig. 2.23) because of structural changes. But this current and resistance was improved by current induced annealing or by applying successive current sweeps as shown in Fig. 2.24. Current was improved due to graphitization at the healing site which was confirmed by the X-ray Photoelectron Spectroscopy (XPS).

Multiwall Nanotube (MWNT) diameter was increased after electron-beam irradiation because of deposition of amorphous carbon which is ascribed to Electron-Beam-Induced-Deposition (EBID). In this process, hydrocarbons dissociated and deposited at broken sites which comes from contamination in SEM. This e-beam irradiation process in SEM gives electrical and mechanical recovery of broken tubes followed by current annealing [98]. Shivani et al. also used the same method for joining of multiwall carbon nanotubes after breakdown but resistance was improved [99]. In this method, Platinum

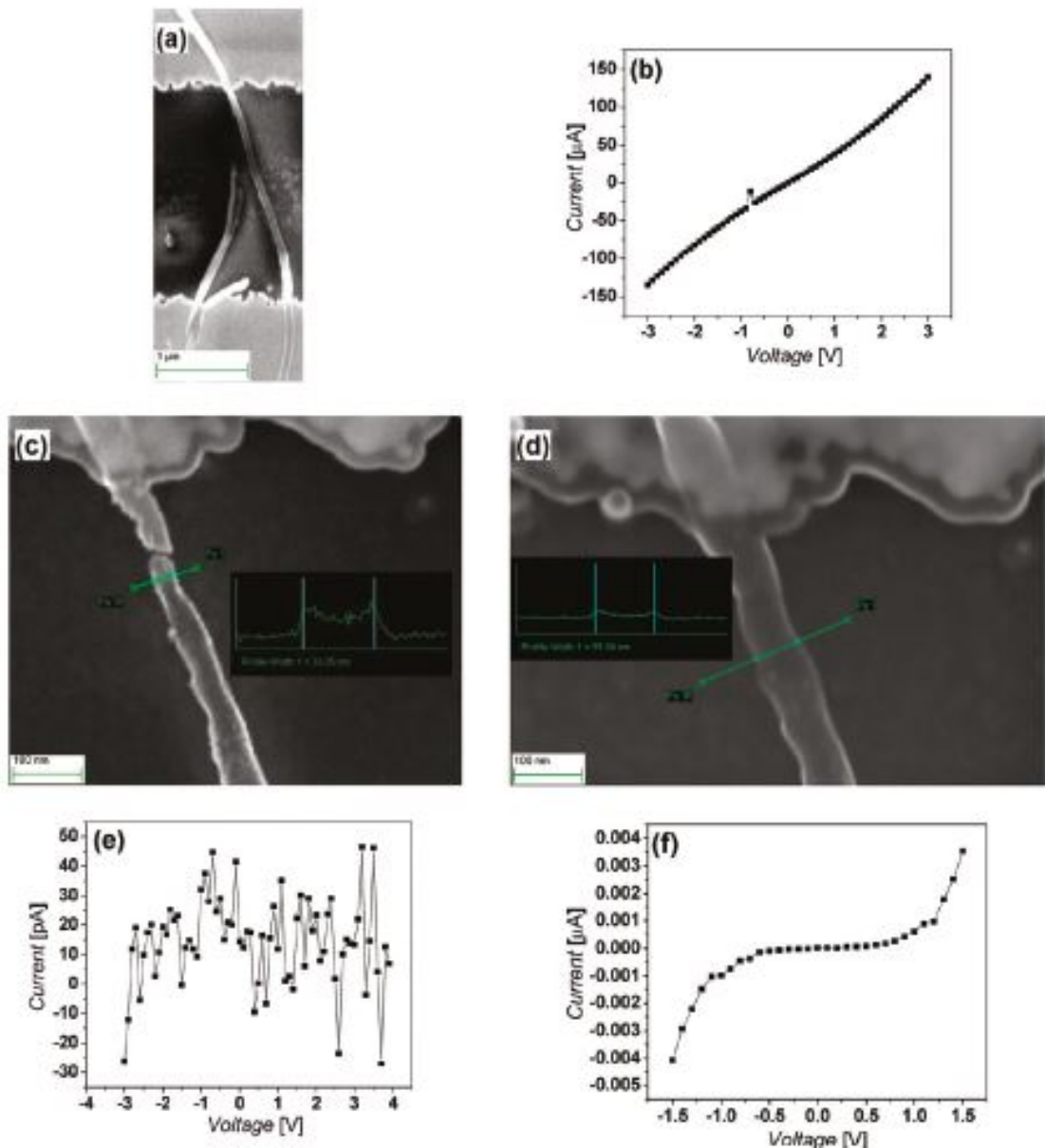


Fig. 2.23. (a) MWNT between contact pads. (b) I-V characteristic of the same tube. (c) SEM of broken tube after applying high voltage. (d) SEM image of same tube after repairing. (e,f) I-V characteristics after breakdown and after healing. This Fig. is adapted from reference [98].

(Pt) and Tungsten (W) were deposited at broken site of nanotube by using Gas Injection System (GIS) or EBID technique. Pt makes ohmic contact with nanotubes and it shows larger resistance values than W. These metal nanoparticles deform the nanotube at broken site and as a result resistance has been increased after joining. Restoration of resistance depends on broken sites of tubes, metal type deposition, metal work-function,

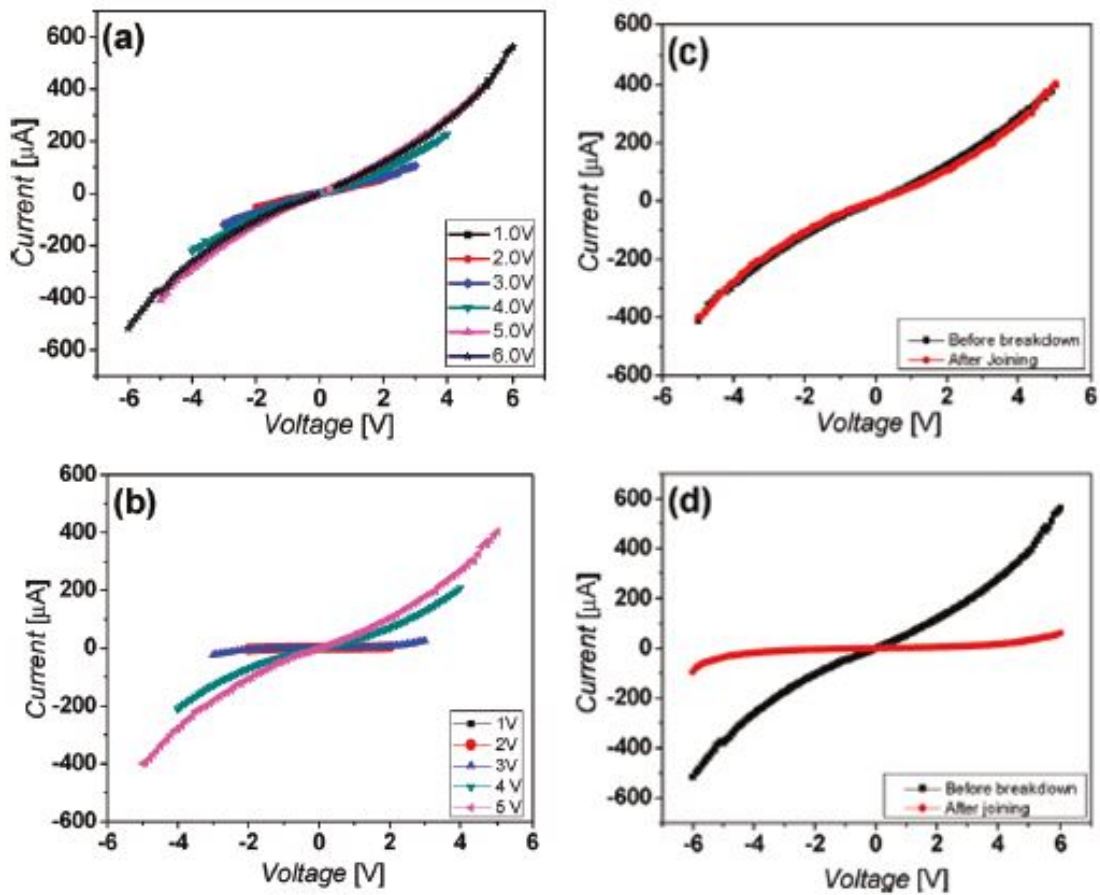


Fig. 2.24. (a) I-V characteristic of current annealed CNT before breakdown. (b) I-V curve after joining of tube. (c) Comparison of current values in the range -5 to 5 V before and after joining. (d) Comparison of current values in the range -6 to 6 V before and after joining. This Fig. is adapted from reference [98].

metal-nanotube contact and contact resistance of metal-nanotube contact. This healing approach for CNTs can be significant for interconnect applications.

2.4.3 Effect of Electron-Beam Irradiation on Graphene and GNR Devices

Electron-beam exposure is used for imaging (SEM and TEM) and e-beam lithography of graphene and graphene devices. Investigation of e-beam irradiation effects in graphene is important for graphene based electronics [103]. Previous studies have been reported on defect creation by e-beam irradiation in CNTs and graphite [104], and Raman spectroscopy of these defects in graphene [87, 105, 106].

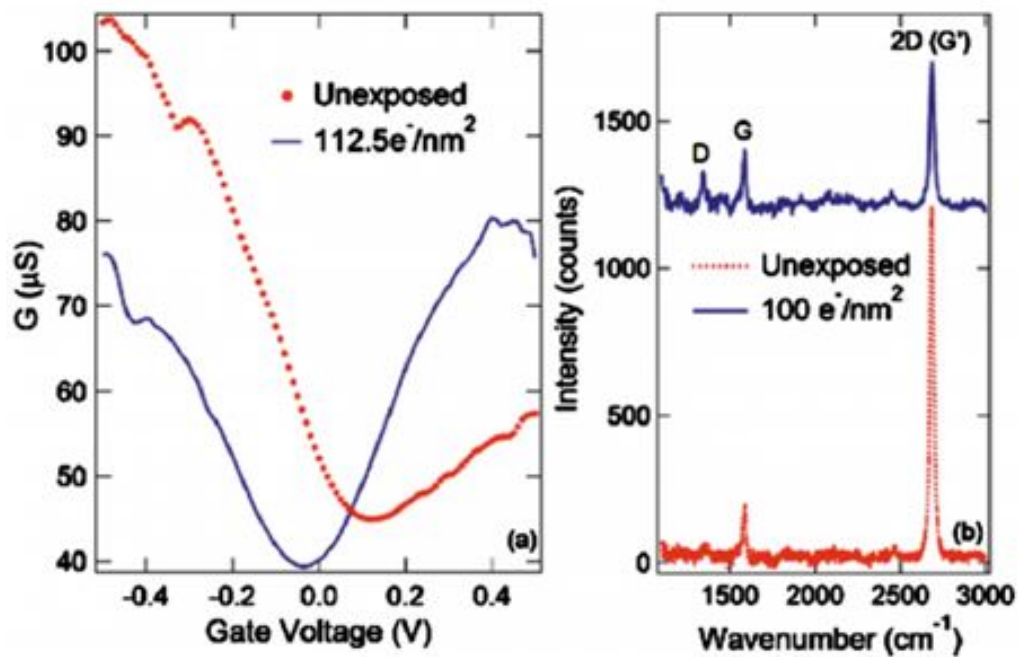


Fig. 2.25. (a) Conductance versus gate voltage before and after exposure for a suspended graphene. (b) Raman Spectrum before and after irradiation on same sample. This graphene was exposed in EVO 40 SEM system with 30 keV acceleration voltage and 0.15 nA current for 5 min. This Fig. is adapted from reference [87].

Electron-beam irradiation shifts the Dirac point to negative value in graphene due to interaction of e-beam with Si/SiO₂ substrate [87]. Electron-beam generates electron-hole pairs in which electrons are more mobile than holes. Charge Neutrality Point (CNP) is shifted to negative bias due to attraction of electrons to trapped holes in Si/SiO₂ interface. Dirac point shifting due to e-beam irradiation is shown in Fig. 2.25. A similar phenomena occurs in Metal Oxide Semiconductor Field Effect Transistor (MOSFET) where threshold voltage is shifted due to e-beam irradiation in MOSFETs [103]. Electron-beam irradiation also damage the lattice of graphene and induce defects and carrier scattering [105]. These defects can be reduced by using low energy e-beam and it deduce higher mobility, CNP towards zero and less residual carrier density. CNP and residual carrier density increase with the e-beam exposure dose. Effect of various exposure current doses in graphene devices are shown in Fig. 2.26 by electrical characteristics [107]. Fig. 2.26(a) shows that low exposure current dose has CNP closer to zero than moderate and high exposure current dose. Raman characteristic of high current dose provide red shift of G and 2D peak and ratio of 2D/G peak is reduced due to heavy doping of graphene [108]. D peak is

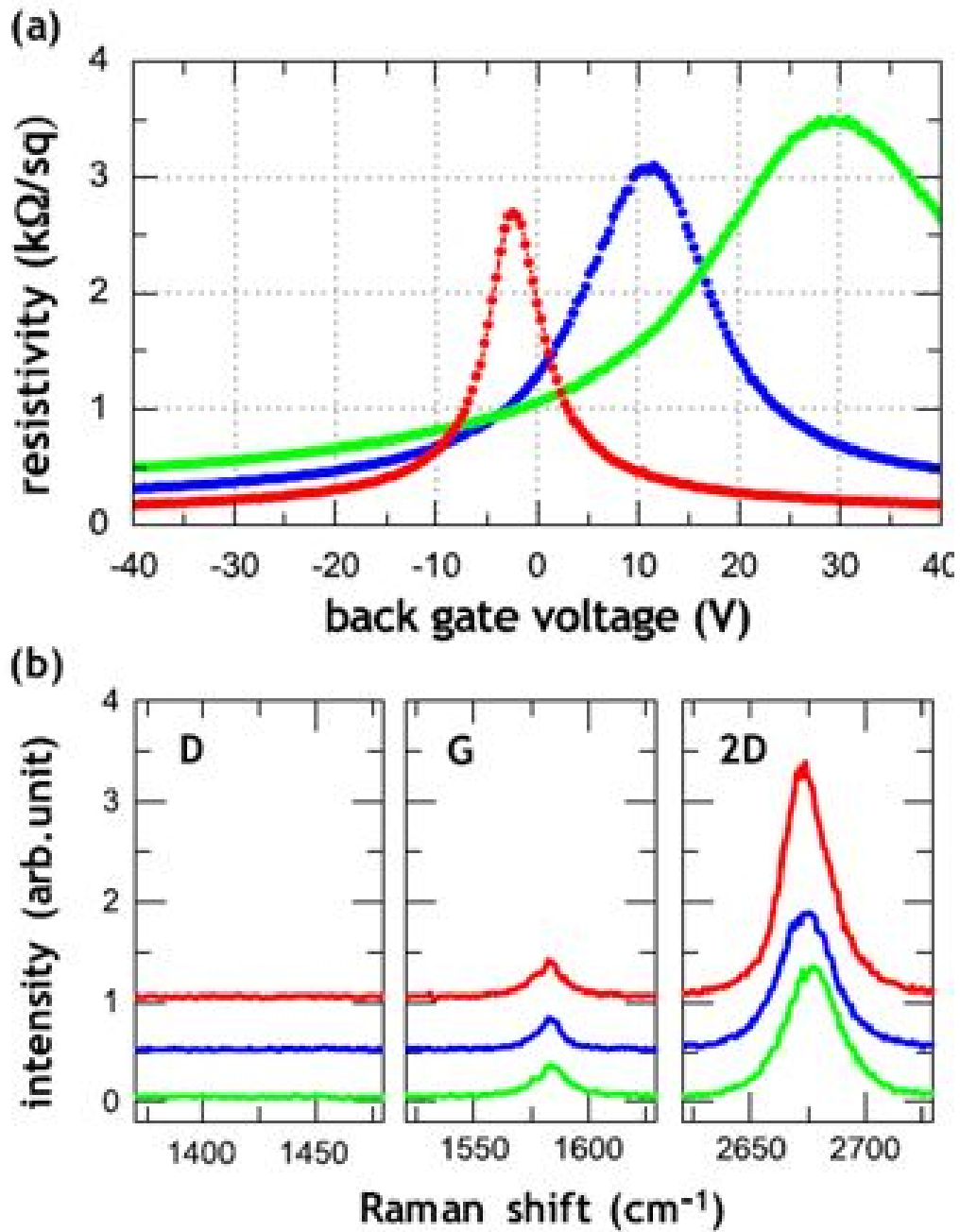


Fig. 2.26. (a) Electrical characteristics of low EBL exposure current (red), moderate EBL exposure current (blue) and high EBL exposure current (green). Low exposure current has better characteristics than moderate and high exposure current. (b) Raman Spectrum of the same devices. G and 2D peak have red shift due to increment of exposure current dose. This Fig. is adapted from reference [107].

not significant due to absence of structural defects or hydrogenation of graphene. E-beam exposure current range was 10 pA to 125 pA at energy of 20 keV and dose of $320 \mu Ccm^{-2}$ and 4 nm step size were used for EBL process [107].

Despite of less exposure dose, crystalline defects occur after EBL process due to radicals of polymer in the resist [109]. The resist is heated in EBL process during exposure which release radicals from polymer at interface with graphene. These radicals contain hydrogen which is released by the depolymerization of PMMA resist. Hydrogenation of graphene degrades the device performance [107]. Thus resist heating is concomitant to exposure dose. Formation of these radicals and trapping of radicals are shown in Fig. 2.27. These radicals were eliminated by Iso-Propyl Alcohol (IPA) cleaning after EBL process. Electrical characteristics of devices are preserved by screening layer of resist or polymer from the ambient effects like moisture. It has been confirmed with other hydrophobic materials [110–112]. Hydrophobic layer also increases mobility in graphene FETs [113]. Even, high temperature (400°C) vacuum or forming gas annealing can not eliminate hydrophobic layer of resist. Kang et al. demonstrate that low exposure current dose not affect the graphene device but resist heating induce the crystalline defects [107].

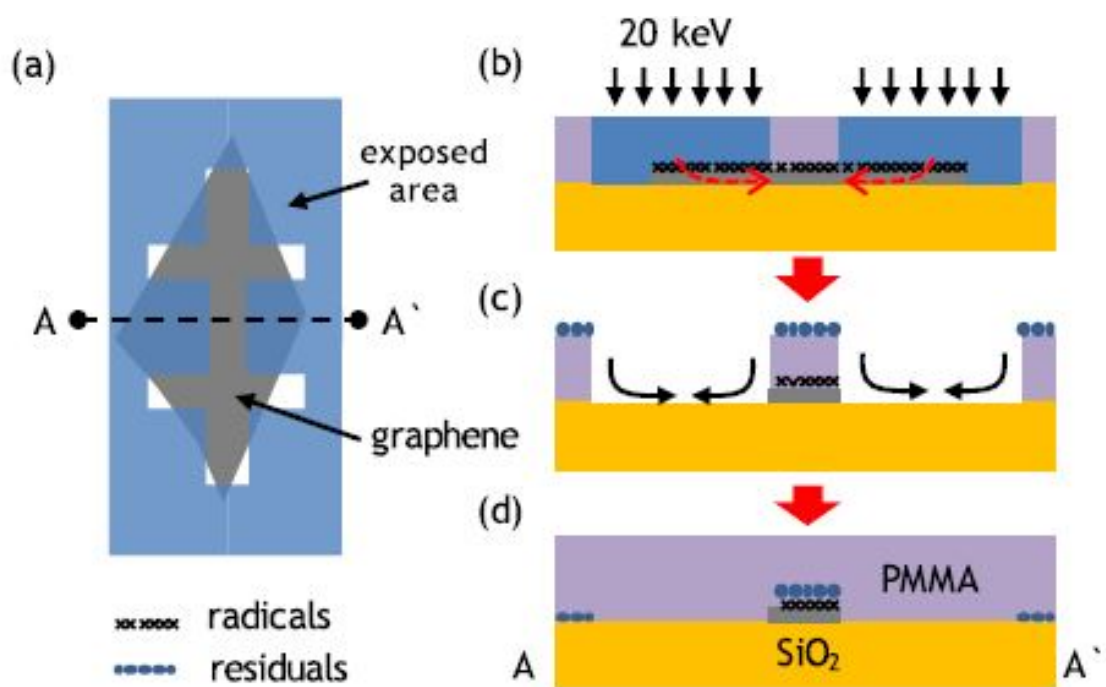


Fig. 2.27. Schematic diagram of resist residual formation and radicals trapping on active area of graphene device. (a) Top view of exfoliated graphene and e-beam irradiated area. (b) Resist radicals are transferred to unexposed graphene-PMMA interface due to e-beam exposure. (c) Irradiated area after development and plasma etching. (d) Second PMMA layer is spin coated and previous residual layer remain under this second PMMA layer which is solidified after baking. This Fig. is adapted from reference [107].

Raman Spectroscopy has been mostly used to study the structural modification in e-beam irradiated graphene [106, 114, 115] or formation of nanocrystalline and amorphous carbon [105]. Raman spectroscopy also analyze the magnitude of D and shift in G peak due to damage and strain which occurs because of e-beam irradiation [116]. Electrical measurements are essential to confirm modifications in transport properties of e-beam irradiated graphene because Raman spectroscopy is incapable to study all electron beam irradiation effects. CNP shifting and doping of irradiated graphene devices have been reported but other transport properties have not been studied in details [87, 117]. Electronic properties of irradiated graphene devices restored after repetitive electrical measurement due to electrical stress [118]. 10 keV electron beam energy was irradiated on graphene devices by using SEM tool. Contact resistance was improved from 200 k Ω to 90 k Ω and mobility 3600 V²cm⁻¹s⁻¹ to 3900 V²cm⁻¹s⁻¹. Device properties were reestablished by applying the consecutive gate voltage sweeps. Graphene-metal coupling effect is enlarged due to electrical stress and it leads to cleaning of channel. Adsorbates from air ambient act as p-dopants in graphene devices which shift the Dirac point towards positive bias. Dirac point shifting increase the contact resistance and reduce the carrier mobility [119–121]. In-situ electrical measurement (in SEM) of post irradiation devices give the lower resistance than air ambient measurement. Repetitive electrical measurement also decrease the hysteresis effect which is shown in Fig. 2.28 [118]. Hysteresis occurs due to the trapping of mobile electrons into gate oxide during e-beam irradiation but it was reduced by removal of electrons from graphene channel during repetitive voltage sweeps [122, 123]. Thus successive electrical measurement restore the channel conductance.

2.5 Breakdown Current Density of Graphene and Graphene Nanoribbons

Graphene and GNRs can be used for interconnect applications like CNTs due to high breakdown current density (10⁸ A/cm²) [35]. Graphene is an appropriate substitute of Cu wires in semiconductor applications due to higher current carrying capacity. It also has smaller resistivity than Cu wires [125]. But graphene nanoribbons has one serious concern that is the breakdown of devices after saturation of current due to resistive heating. After a certain voltage, resistance start to increase and current gets saturated leading to

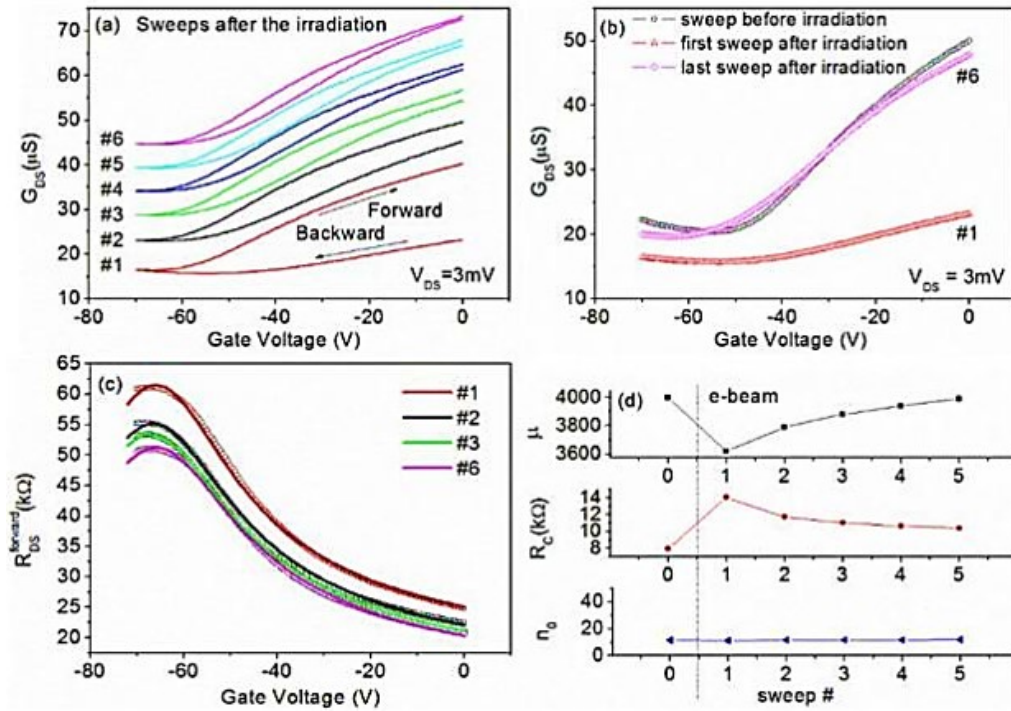


Fig. 2.28. Electron-beam irradiation effects on GFETs. (a) Six consecutive sweeps after e-beam irradiation. Hysteresis has been reduced after sixth sweeping. (b) First and sixth sweep of irradiated device compared with the unexposed device. (c) Experimental data values compared with modeling data [124]. (d) Summary of extracted mobility, contact resistance and carrier concentration. This Fig. is adapted from reference [118].

breakdown of the devices [126]. Contact metals introduce impurities which enhance the resistance value. As impurity density increases it causes the electron-phonon scattering. Impurity density is extracted from the Dirac point shifting [127]. Breakdown current of nanoribbons is shown in Fig. 2.29. It shows that after certain bias voltage, current get saturated and then breakdown take place [35].

Lee et al. reported a breakdown current density upto $4 \times 10^7 \text{ A/cm}^2$ in CVD graphene [90]. Here breakdown is also concomitant to resistive heating. Graphene wires of width in the range of $1\text{-}10 \mu\text{m}$ and length upto $1000 \mu\text{m}$ show ohmic behavior and its resistance linearly depends on wire length which is attributes to diffusive transport [90, 128]. After applying high bias, graphene get cracks in center of graphene length due to resistive heating [90]. The electrical breakdown density relation with resistivity is expressed as $J_{max} \propto 1/\sqrt{\rho}$ [129]. Breakdown current density decreases with the resistivity which is shown in Fig. 2.29(d). Breakdown current density in CVD graphene is less due to defects and high

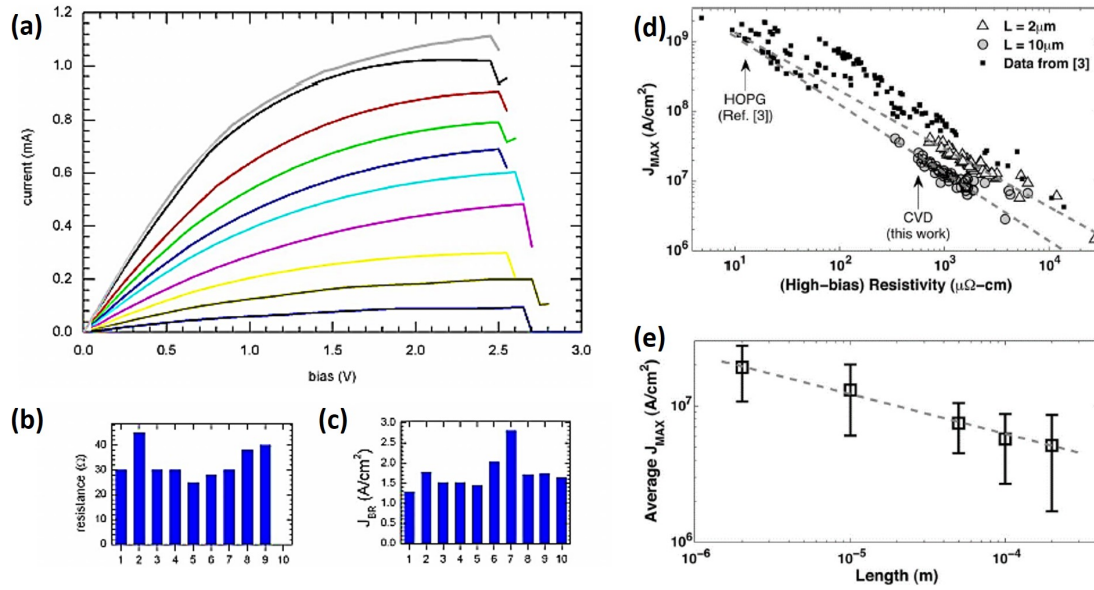


Fig. 2.29. (a) Current-voltage characteristic of 22 nm width GNR array of 10 GNRs which shows breakdown after certain bias voltage. (b,c) Resistance and breakdown current density (unit $\cdot 10^8$ A/cm 2) of 10 GNRs [90]. (d) Breakdown current density versus resistivity. (e) The average breakdown current density as a function of wire length. This Fig. is adapted from reference [35].

impurity density than HOPG. Fig. 2.29(e) shows that as wire length is reduced it gives higher breakdown current values [90].

2.6 Summary

The current status of understanding of the following topics, which are relevant to the work reported in this thesis are reviewed in this chapter.

1. Electronic structure and properties of graphene and graphene nanoribbons is discussed in this chapter. Bandgap opening in graphene and bandgap engineering parameters of nanoribbons are described.
2. Various synthesis methods of GNR and their electrical characteristics are reviewed in this chapter.
3. The breakdown causes of graphene and reconstruction of graphene nanoribbons by high energy electrons are reviewed briefly. Healing of carbon nanotubes by low energy e-beam is described.

4. The breakdown current density of graphene and nanoribbons is also discussed as it has important role for interconnect and nanoelectronic applications.

Chapter 3

Experimental Techniques Used in This Work

This chapter describe the methods and tools used for the fabrication and characterization in this thesis. EBL and sputtering were used for fabrication of graphene and GNR devices. These fabrication techniques are discussed in this chapter. The characterization techniques, namely optical microscopy, AFM, SEM and Raman spectroscopy are also described in this chapter which were used for physical characterizations of graphene and GNR devices. The electrical characterization tool Semiconductor Device Analyzer is also described which was used to measure the electrical characteristics of the devices.

3.1 Preparation of Graphene on SiO₂ Substrate

Graphene on SiO₂ substrate were prepared by two methods. First is the mechanical exfoliation method in which graphene was mechanically exfoliated on SiO₂ substrate by scotch tape using Highly Oriented Pyrolytic Graphite (HOPG). HOPG was purchased from Graphenea S.A. Graphene layers can be identified in optical microscope after exfoliation. Second method is the transfer of CVD graphene on SiO₂ substrate using Cu etchant [130]. CVD monolayer graphene on Cu foil was also purchased from Graphenea S.A. In this method, PMMA resist was spin-coated on graphene on Cu foil at 3200 rpm for 45 sec and baked at 175°C for 7 min. Subsequently PMMA/Graphene/Cu foil was kept in Cu etchant (CE-100) solution (Transene Co. Inc.) to etch-out Cu. Floated PMMA/graphene film was transferred in DI water by scooping. PMMA/Graphene film

was rinsed with DI water 6-7 times to remove residue of Cu etchant. After cleaning with DI water, PMMA/graphene film was transferred on SiO₂/Si substrate and kept for natural drying for 12 hours to remove water from the sample. Sample was kept in acetone at 60°C for 30 min. to strip-off PMMA resist and then kept in fresh acetone at room temperature for 10 hours to remove PMMA residues. Optical images of graphene on SiO₂ substrate obtained by both the methods are shown in Fig. 3.1.

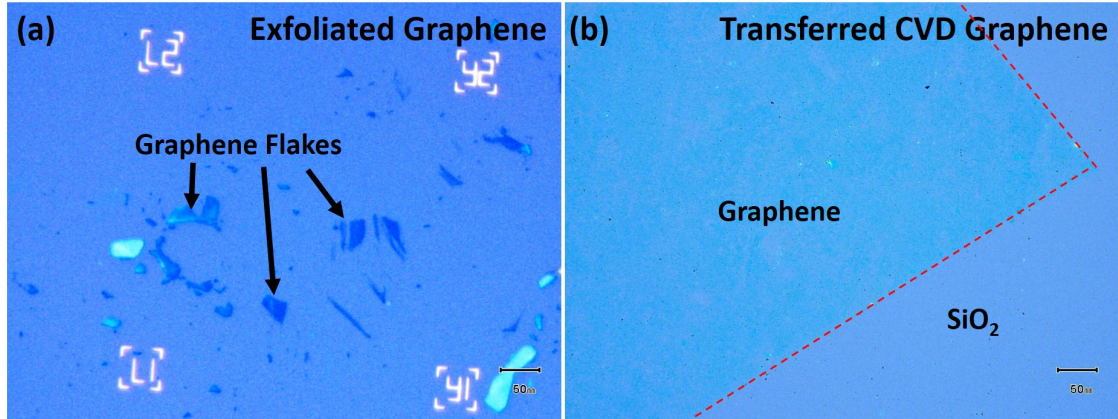


Fig. 3.1. Optical micrograph of (a) exfoliated graphene flakes on SiO₂ substrate, and (b) transferred CVD graphene. For identification of graphene boundary on SiO₂ substrate, red dashed line is drawn.

3.2 Electron-Beam Lithography

Optical lithography is not feasible at nanoscale level in our laboratory due to limitation of resolution by wavelength and numerical aperture [131]. Electron-Beam Lithography (EBL) is a widely used technique in laboratories and low volume production. The wavelength of an electron is described by the de Broglie equation [132].

$$\lambda = h/p \quad (3.1)$$

Here h is the Planck's constant and p is the momentum of electron. The electron's velocity in an electric potential U is given by

$$v = \sqrt{2qU/m_o} \quad (3.2)$$

Here, m_o is the rest mass of the electron and q is the charge of the electron. By using of equation 3.2, wavelength of electron can be expressed as [132]

$$\lambda = h/p = h/m_o v = h/ \sqrt{2m_o eU} \quad (3.3)$$

Electron is accelerated through several thousand volts in an EBL system. Electrons travel with a fraction of the speed of light. In SEM, the electron velocity with accelerating voltage 10 kV gives 20% fraction of the speed of light. In TEM, 200 kV electron velocity has 70% fraction of the light speed. So after accountability of relativistic effect, electron wavelength equation can be expressed as-

$$\lambda = (h/ \sqrt{2m_o eU})(1/ \sqrt{1 + eU/2m_o c^2}) \quad (3.4)$$

Here c is the speed of light. In this equation, first term is the non-relativistic while second term denotes relativistic correction factor. In SEM, 10 kV accelerating voltage has 12.3 picometer electron wavelength and 200 kV in TEM has 2.5 picometer wavelength of electron. In EBL, different accelerating voltage can be used for patterning.

EBL is a direct writing technique for patterning of nanostructures without using physical mask [133]. EBL system is the state of the art for nano and microscale devices because high resolution and patterning of nano-features (sub-10 nm) is attainable in EBL system. EBL system we have used (Raith 150^{Two}) is an integrated system for nanolithography and SEM imaging which produce the nanometer size patterns on resist by focusing e-beam on a certain position of the sample. Two types of e-beam sensitive resist, negative and positive resist can be used for writing of designs. The pattern or mask is designed using CAD tool or software in EBL system. The exposure of e-beam change the solubility of resist and subsequently resist is developed in a developer solution and resist is dissolved selectively in exposed region or non-exposed regions depending on the type of the resist. The resulting pattern on resist is transferred on substrate via etching or metal deposition followed by lift-off process. Electron-beam lithography step process is shown in Fig. 3.2 [133].

Fabrication of complex structure of nanoscales is also possible via iteration of number of lithography steps. For pattern writing, stage position is fixed for write field area

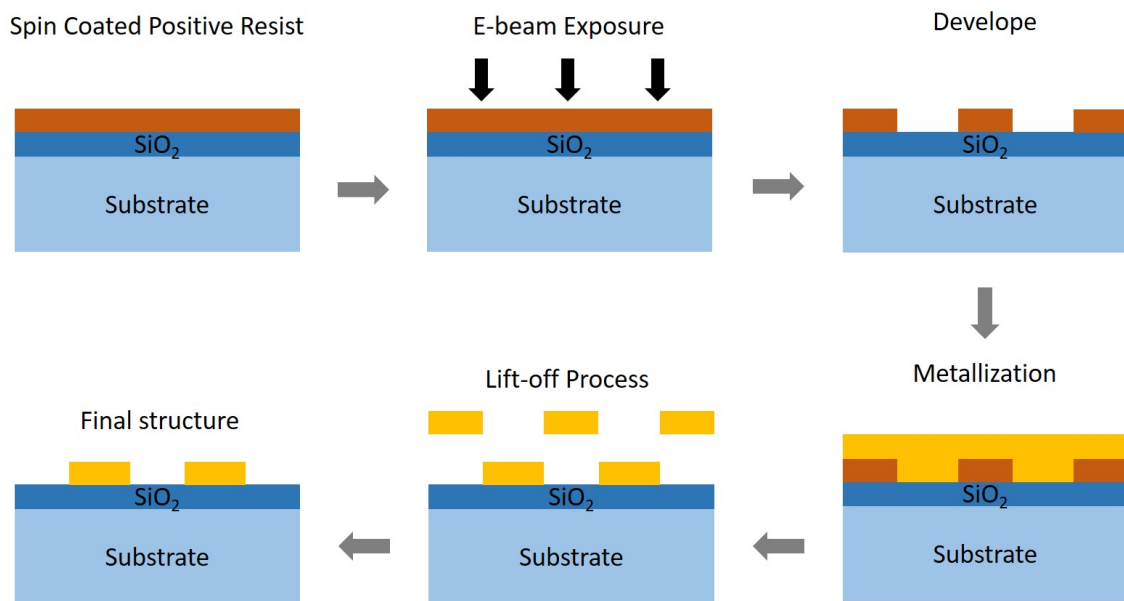


Fig. 3.2. Schematic description of an e-beam lithography process for patterning of metals.

(few μm to 1-2 mm). Stage moves one write field to another write field for pattern writing and e-beam is blanked out of the write field. Field stitching error between the write-fields is minimized by the laser interferometry stage position system which stitch each write field with nanoscale precision without overlapping. Proximity effect is a salient feature of EBL system. In this effect incident e-beam expose the undesired region near the pattern due to electron scattering from the resist and the substrates. Proximity effect make round corners of the design and modify the line width and gap spacing. High resolution, nanometer stitching error (few 10s of nm) and overlay accuracy is required to get desired patterns. Optimization of EBL parameters viz. exposure dose, energy, write field, resist thickness and developing time has to be precise for high resolution, pattern fidelity and defined exposure window of patterns.

Major components of typical EBL system and simplified ray diagram of round-beam electron lithography system is shown in Fig. 3.3 [134]. In EBL technique, microscope column generates electron beam. High-energy electron beam generated from column interact with atoms of the specimen. Example of designs which are patterned by e-beam lithography are shown in Fig. 3.4(a) and (b).

We used Raith 150 Two system for our work. Accelerating voltage 0.1 kV to 30 kV is used for imaging and patterning in EBL system. Step size of 40 nm and dose of $150 \mu\text{Ccm}^{-2}$ were used for patterning of devices in EBL. PMMA resist was used for patterning

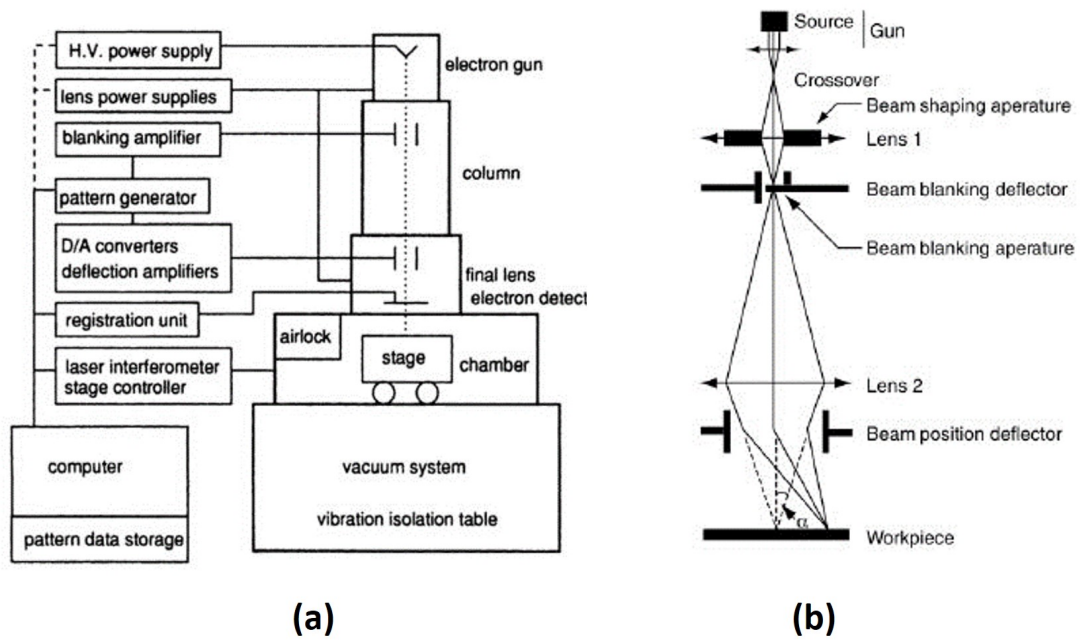


Fig. 3.3. (a) Block Diagram of major components of electron beam lithography system, adapted from reference [135]. (b) A simplified ray diagram of round-beam electron lithography system, adapted from reference [134].

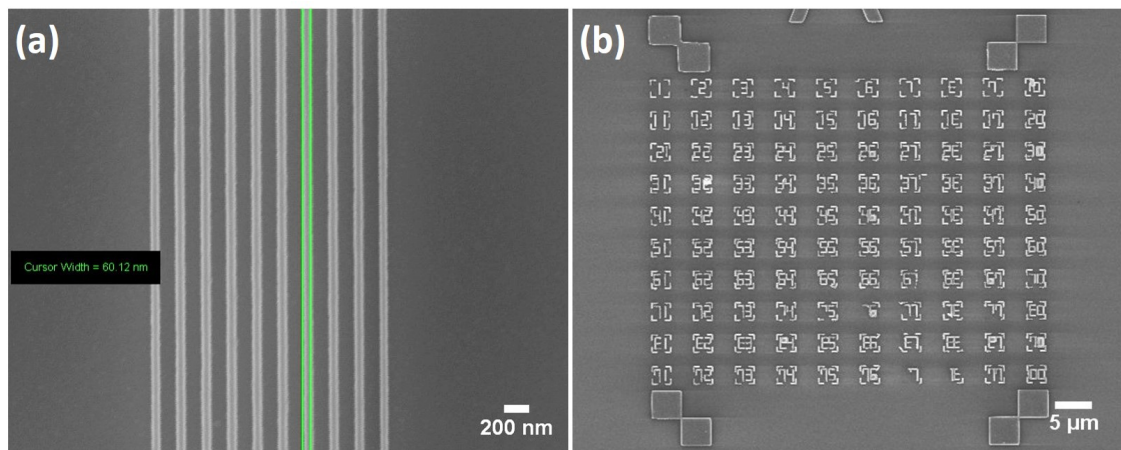


Fig. 3.4. (a) SEM image of 60 nm width array of lines patterned using Raith 150^{Two} lithography system. (b) SEM image of array of numbers which was patterned by Raith 150^{Two} system.

of contact pads in EBL. Electron beam lithography process steps is discussed in appendix A1.

3.3 Sputtering Technique

Sputtering is a physical vapor deposition technique for deposition of thin films of materials onto a substrate. In sputtering process, gaseous plasma is generated and ions from the plasma accelerate onto target source material [136]. Atoms are ejected from target material and travel in straight line and get deposited as a thin film onto substrate.

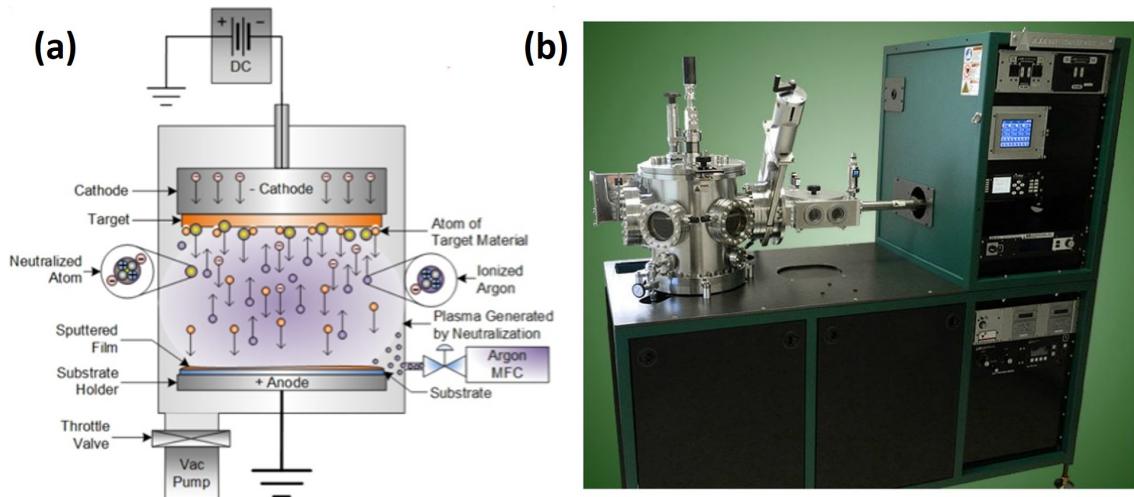


Fig. 3.5. (a) Schematic illustration of sputtering system (image is adapted from URL: <http://www.semicore.com/images/photos/diagram-dc-sputtering-process.png>). (b) Photograph of Orion sputter system, adapted from IIT Bombay Nanofabrication facility website (URL: http://www.cen.iitb.ac.in/slotbooking/GLIMPSE/197_GLIMPSE.pdf).

Sputtering is a good technique for deposition of thin films because of following reasons.

- Excellent film uniformity, for large areas also
- Good adhesion
- Thickness control and smoothness of surface
- Higher deposition rate than evaporation
- Stability of thin film

The energy source in sputtering are categorized into three categories (i) Radio Frequency (RF), (ii) Direct Current (DC) and (iii) microwave. These energy source maintain the plasma state in the chamber. DC sputtering is the best for deposition of conductive

materials like metals. In DC sputtering, metal deposition is easy to control and has low cost. RF sputtering is used for deposition of dielectric materials like SiO_2 and TiO_2 . RF source also can be used for metal deposition. RF sputtering has slower deposition rate than DC sputtering. RF sputtering has much higher power source cost. Major components of sputtering system is shown in Fig. 3.5(a) [136].

We used AJA international inc. Orion sputter system for deposition of Ti, Ni and Pt. Model of Orion sputter system which we used is shown in Fig. 3.5(b). Metal deposition was carried out in high vacuum of 10^{-7} mTorr. DC power of 150 and 100 watt were used for Ti and Pt deposition. RF power of 35 watt was used for Ni deposition.

3.4 Optical Microscopy

Graphene layers are clearly visible on 90 and 300 nm SiO_2 in optical microscopy [137]. Monolayer or few layer (2-3 layers) graphene are not visible on 200 nm SiO_2 but more than 10 layer of graphene are visible on 200 nm SiO_2 . Graphene layers are visible on SiO_2 in optical microscope under white light illumination. According to Fresnel theory, graphene contrast can be maximized on SiO_2 by using appropriate filters. Contrast of graphene as a function of wavelength is shown in Fig. 3.6 which is adapted from reference [137].

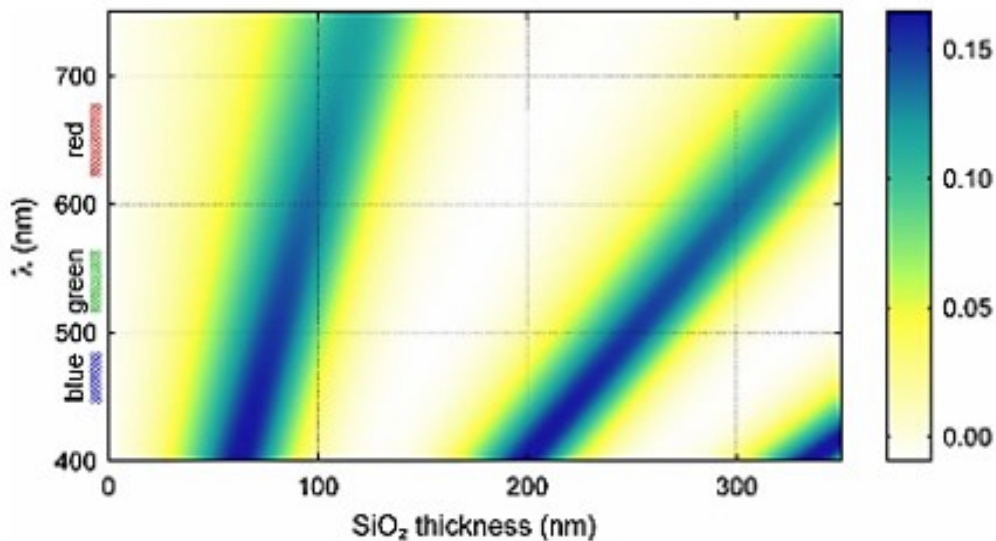


Fig. 3.6. Contrast of graphene as a function of wavelength, adapted from reference [137].

Monolayer graphene appears purple in color while graphite flakes give bluish contrast on SiO₂ in optical microscope [137]. Graphite flakes give more contrast than few layers of graphene in dark field and in bright field of optical images. Dark field and bright field optical images of graphene flakes are shown in Fig. 3.7.

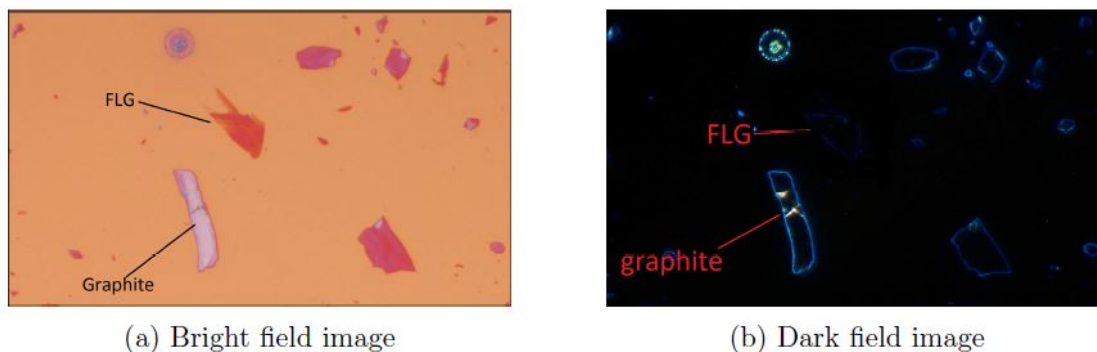


Fig. 3.7. Optical images of mechanically exfoliated graphene. (a) Bright field optical image. (b) Dark field optical image. Graphite flake boundary is glowing more than few layer graphene. This image is adapted with permission from Dawuth Pathan's thesis.

3.5 Scanning Electron Microscopy (SEM)

Scanning Electron Microscopy has been used as one of the primary characterization technique for our work. In our work, SEM analysis was done at typically low electron beam energy (3 - 5 keV).

The operating principle of SEM is shown in Fig. 3.8(a). The instrument used in this work (JSM-7600F FEG-SEM by Jeol Ltd) is shown in Fig. 3.8(b). SEM components are housed inside a vertical column evacuated by a combination of vacuum pumps. The electron gun acts as a source which is mounted at the top of the instrument. Electrons emitted from the source are accelerated to a typical voltage of 1-40 kV and then are focused to form a beam which is used for imaging and analysis. The electron from the source are produced either by thermionic heating or field emission. Because of the nature of source, SEM are usually categorized into two namely thermal SEM and Field Emission SEM (FESEM). The latter offers higher resolution, less electrostatic distortion and spatial resolution down to 2 nm.

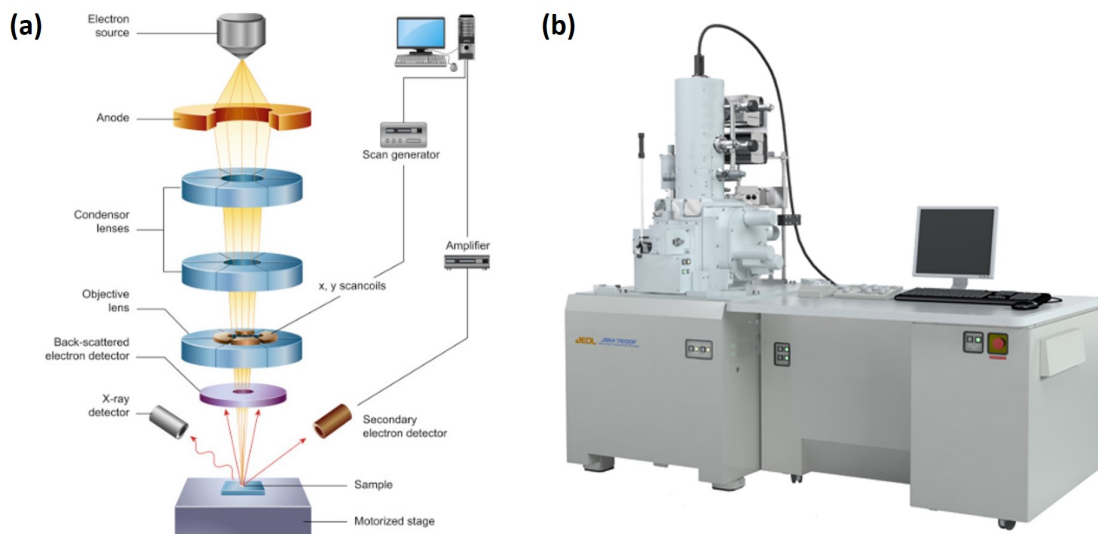


Fig. 3.8. (a) Principle of SEM instrument is shown by a schematic diagram. This image is taken from reference [138]. (b) Photograph of the FESEM instrument which is used for our work. This image is adapted from website of Jeol manufacturer (<https://www.jeol.co.jp/en/products/detail/JSM-7600F.html>).

In our work, we have used the FESEM for our analysis. In order to resolve a feature on the sample surface, the diameter of the beam must be smaller than the interested feature, and hence it is required to condense the electron beam. In order to achieve this, a series of electromagnetic lenses (also referred to as condenser lenses) are employed to focus the beam on the sample. The last of the lenses near to the sample, is called the objective lens. To refine the electron beam, variable apertures are used. For better resolution and good depth of field, small objective aperture size are used. The correct aperture size is subjected to the requirement of analysis and is chosen accordingly. As the beam is focused, the required deflection in the X and Y axes is caused by scanning coils. This makes the scanning of the sample in a raster fashion over the surface of the specimen. At the end of the column, sample are mounted into an evacuated chamber called sample chamber. It is housed with a variety of detectors that assist in imaging of the sample. When the incident electron beam is accelerated onto the sample, it interacts in elastic and inelastic fashion which gives different types of signals. In elastic interaction, the kinetic energy of the electrons is not affected and such scattering of electrons is called backscattering. These electrons are high in energy and helps in imaging and quantitative analysis of the sample. A Backscatter Electron Detector (BSD) inside sample chamber detects

such elastically scattered electrons. Backscattered electrons are subjected to the topography and composition of the sample, and gives an insight to the material's grain size and morphology. During the impact, the highly accelerated electrons transfer the energy to the atoms of sample and results in knocking off electrons from those atoms. These electrons are called Secondary Electrons (SE). A Secondary Electron Detector (SED) offers images which uses these inelastically scattered electrons. The images resolved from SED are independent of the material. Interaction of e-beam with specimen's surface is shown in Fig. 3.9(a). An example of SEM image of Pt nanoparticles is shown in Fig. 3.9(b). We used Raith 150^{Two} and JSM-7600F FEG-SEM by Jeol Ltd for this work. For SEM imaging, 3 keV in Jeol FEG-SEM and 5 keV in Raith 150^{Two} were used.

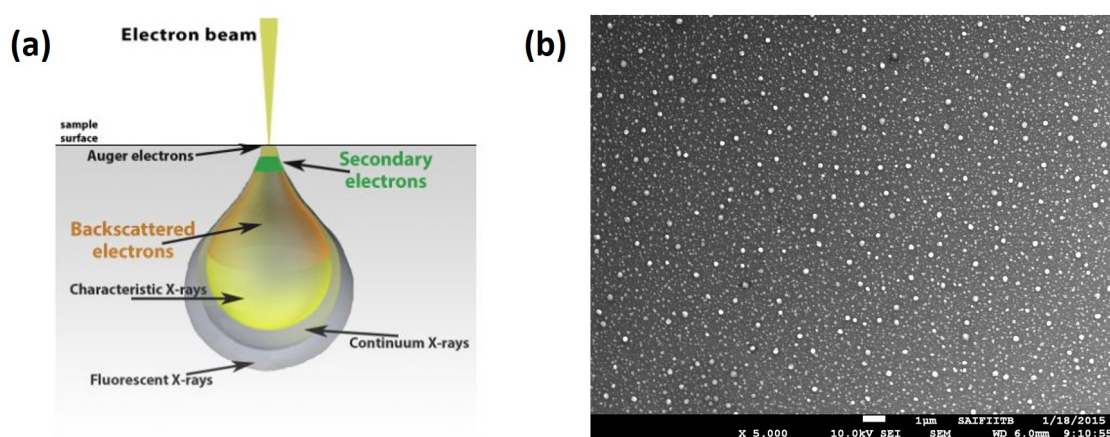


Fig. 3.9. (a) Schematic description of electron interaction with incident electron-beam. This image is adapted from Nanoscience Instruments Inc. website (URL: <https://www.nanoscience.com/techniques/scanning-electron-microscopy/>). (b) SEM image of Pt nanoparticles which is taken in FESEM tool.

3.6 Atomic Force Microscopy (AFM)

AFM is a type of scanning probe microscopy technique. AFM is a low throughput technique for capturing layers of graphene. AFM imaging is the second characterization technique after Raman spectroscopy to measure width and thickness of graphene and GNRs. AFM technique was developed to overcome drawback of STM. STM need conducting surface but AFM does not require conducting substrate. It can be used for various materials like polymers, ceramics, conductors and biological samples. AFM captures topogra-

phy image of a sample surface by measuring interaction force between a tip and a sample surface [139]. A typical AFM consists of a laser, a cantilever, a scanner and a 4-quadrant photodiode. Cantilever has a small tip (6-20 nm diameter) at free end which is typically made of Si or silicon nitride (Si_3N_4). The force between sample and tip depends on spring constant of cantilever and distance between sample and tip. This force can be described by Hook's law.

$$F = -kx \quad (3.5)$$

where F = force, k = spring constant and x = cantilever deflection. Probe with cantilever moves across the sample up and down, and these fluctuations are due to electrostatic, magnetic and vanderwaal interactions between the tip and the surface of the sample. These deflections are measured by the reflection of a laser beam. Topography image of surface is directly measured by the deflection of cantilver. Principle of AFM is shown in Fig. 3.10(a). AFM has two imaging modes, contact and non-contact mode. In contact mode, deflection of cantilever is kept constant while in non-contact mode, tip oscillates at resonance frequency and amplitude of oscillation is constant [139].

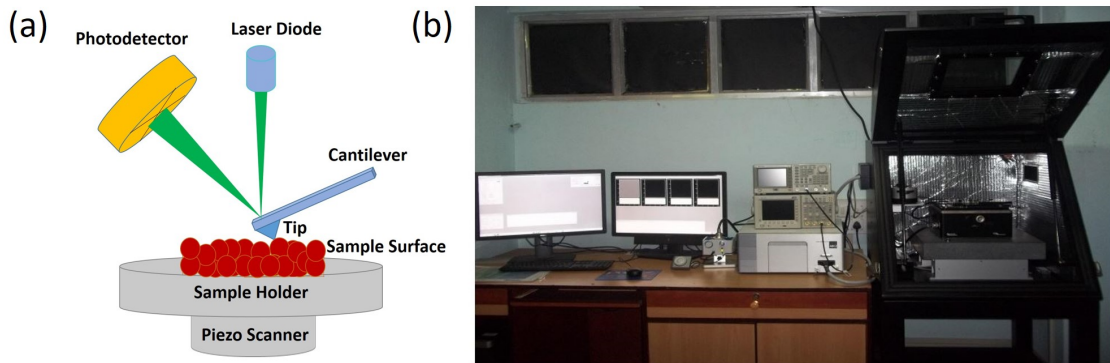


Fig. 3.10. (a) Schematic of principle of atomic force microscope. Image is taken from reference [139] (b) Photograph of Asylum/Oxford Instruments MFP3D Origin atomic force microscope. Image is taken from IIT Bombay Central Facilities website (URL: <https://drona.ircc.iitb.ac.in/ircc/NewFac/CentralFacilityIndex.jsp?facilityCode=EE003>).

AFM determine surface topography, size, texture, surface roughness and line profile features. We used Asylum/Oxford Instruments MFP3D Origin model for AFM imaging of our samples which is shown in Fig. 3.10(b). It has a maximum scan area of $90 \times 90 \mu\text{m}^2$

and minimum scan area is around 30 nm^2 . Maximum scan depth is $14 \mu\text{m}$ and minimum can be a few nanometres. It has capability of good external noise isolation. Example of AFM images of graphene and GNRs are shown in Fig. 3.11.

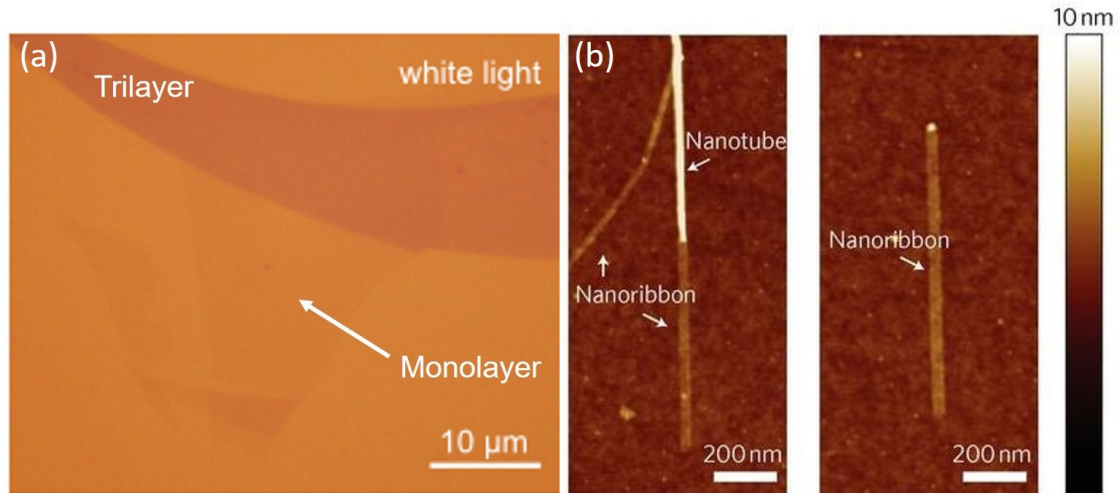


Fig. 3.11. (a) AFM image of monolayer and trilayer graphene. Source of image is Graphene Industries Ltd. website (URL: <http://grapheneindustries.com/Products>). (b) AFM images of carbon nanotubes and graphene nanoribbons [33].

3.7 Raman Spectroscopy and Imaging

Raman spectroscopy is a quick, high throughput and nondestructive characterization technique to identify graphene and GNR as compared to STM, AFM and TEM which are relatively time consuming and destructive techniques. Raman spectroscopy is based on the inelastic scattering of monochromatic light [141]. The monochromatic light (laser source) incident on the sample produce stoke and anti-stokes Raman scattered light. This provides information of electronic and vibrational states of the material. Each material has its unique Raman finger print. Difference between the incident and scattered light is measured in terms of Raman shift (cm^{-1}). Raman spectrum gives the information about material's property like crystallinity and order-disorder states, and amorphous states. In case of GNRs, Raman spectroscopy provide the information about edge disorders, number of layers, doping and type of nanoribbons (armchair or zigzag). Raman spectra of graphene shows two intense peaks, G band at 1580 cm^{-1} and 2D band at 2700 cm^{-1} as shown in Fig. 3.12(a). G band appears due to doubly degenerate zone center E_{2g} mode

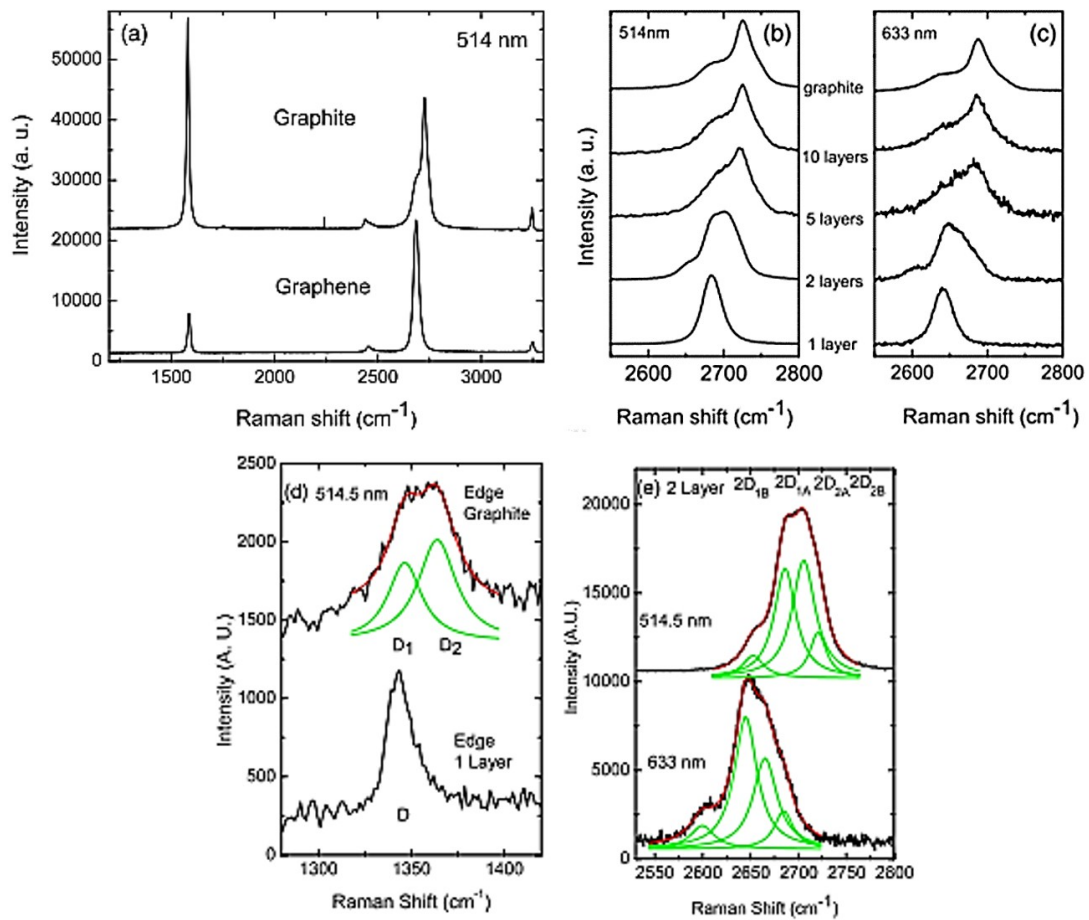


Fig. 3.12. (a) Raman spectrum of bulk graphite and graphene obtained using a 514 nm laser. (b,c) Raman spectra using 514 nm and 633 nm lasers with the number of layers. (d) D band at the edge of graphite and monolayer graphene (514 nm laser). (e) Four components of the 2D band are shown in bilayer graphene (514 and 633 nm) [140].

(in-plane motion of carbon atoms). These two bands appear only in pristine graphene. G band shifts to lower frequencies as increases the number of layers. Doping and strain effects influence the line width and frequency of G peak [141]. G band also gives red shifts due to heavy doping in graphene [108]. D band appears at 1350 cm^{-1} due to the lattice vibrations which occurs out of the brillouin zone center [142]. According to Thomsen theory, these defects arise due to intraband phonon scattering [143]. D' band also appears at $\sim 1620 \text{ cm}^{-1}$ in graphene due to Double Resonance (DR) process (intravalley process) [144]. DR process is a two-phonon process where two phonons excite with opposite momenta q and $-q$. Due to DR process $D + D'$ and $2D'$ peaks also appear at $\sim 2450 \text{ cm}^{-1}$ and $\sim 3200 \text{ cm}^{-1}$ respectively. 2D peak width, shape and position changes

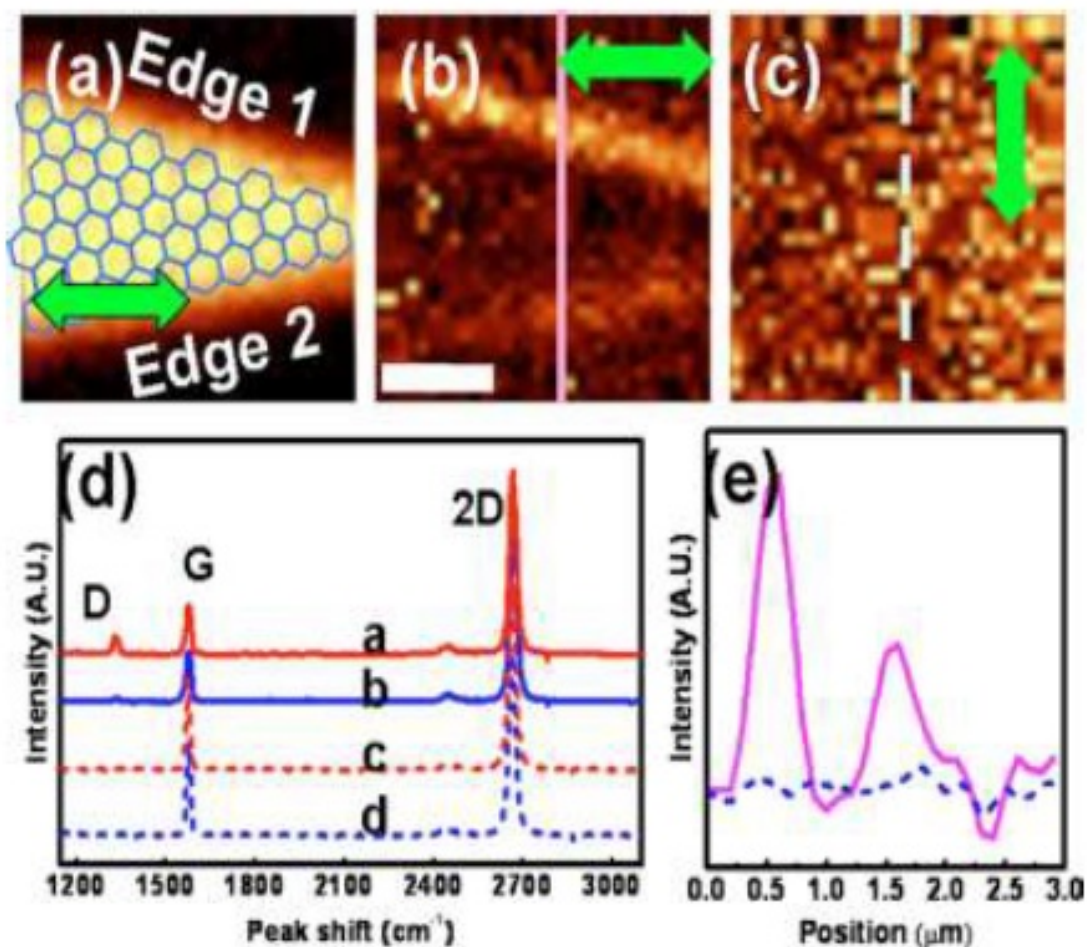


Fig. 3.13. (a) Raman mapping of G band intensity of armchair (edge 1) and zigzag (edge 2). (b,c) Raman imaging of D band intensity along horizontal and vertical polarization direction. (d) Raman spectra of edge 1 and 2 (a,b) due to horizontal polarization and (c,d) due to vertical polarization. (e) Spectra of D band intensity of b and c [80].

with the number of layers [140, 145]. The excitation or laser energy in the range of 1.2 - 4 eV was used for Raman measurements. Evaluation of 2D peak with 514 nm and 632 nm lasers are shown in Fig. 3.12(b,c). 2D line becomes much broader at 633 nm excitation as compared to 532 nm excitation. 2D peak is four times more intense than G peak in monolayer graphene. Higher intensity of G peak indicates higher number of graphene layers and correspondingly associated 2D band intensity decreases along with peak broadening. 2D peak in graphite is divided into two components, $2D_1$ and $2D_2$ that is $1/4$ and $1/2$ of G peak intensity and D peak also has 2 components D_1 and D_2 as shown in Fig. 3.12(d) [146, 147]. Bilayer graphene shows broader and upshifted 2D band than



Fig. 3.14. Photograph of Horiba LabRAM HR model of laser confocal Raman microscope which is used for Raman measurements. Photograph is taken from Horiba Ltd. website (URL: https://www.horiba.com/en_en/products/detail/action/show/Product/labram-hr-evolution-1083).

single layer graphene [148]. 2D band of bulk graphite is quite different with respect to graphene. Bilayer graphene has 4 components $2D_{1A}$, $2D_{1B}$, $2D_{2A}$ and $2D_{2B}$ that is shown in Fig. 3.12(e) [149]. $2D_{1A}$ and $2D_{2A}$ have higher intensity with respect of other two peaks. Intensity of lower frequency $2D_1$ peaks decrease with the increment of number of layers. Raman spectrum of more than 5 layers is indistinguishable with bulk graphite.

Raman imaging localize the number of layers, defects and edges of graphene. Edge chirality depends on D peak that is also strongly related to laser polarization [80]. Raman imaging of armchair and zigzag edged graphene is shown in Fig. 3.13. Polarized Raman of graphene in Fig. 3.13(b,c) reveal that D peak intensity is different in arm-chair and zigzag edges. D peak is more intense in armchair edges and less intense in zigzag edges because DR process is more prominent in armchair edges while in zigzag edges DR process is vanished [80]. G and D band intensity of edge chirality vary with polarization angles that is shown in Fig. 3.13(d,e). Horizontal polarization has prominent D peak intensity while D peak is negligible in vertical polarization [60, 150]. This study emphasize that Raman spectroscopy is a practical approach for determination of edge chirality of graphene and nanoribbons.

We used HR800-UV confocal micro-Raman spectrometer for analysis of graphene and graphene nanoribbons. It has 532 nm laser source (Ar-ion laser) with 5 mW power. Photograph of the Horiba model of laser confocal Raman spectrometer is shown in Fig. 3.14. It has Olympus BX41 microscope with confocal collection system. Two excitation sources (a) 532 nm (maximum power - 50 mW) and 633 nm (maximum power - 20 mW) are available in this system. It has XYZ mapping capability with XY stage (X = 75 mm, Y = 50 mm, step size = 50 nm) and z stage (min step = 0.1 μm).

3.8 Semiconductor Device Analyzer

Semiconductor device analyzer is the new generation one box solution for the all Direct Current (DC) / Alternating Current (AC) electrical characterization and for analysis of semiconductor devices. It provide the current - voltage (I-V) and capacitance - voltage (C-V) characterizations, and analyse is quick and accurate. Semiconductor device analyzer integrates all the measurement resources in one semiconductor parametric test box. Evaluation of I-V and C-V characteristics of devices is very quick and easy in semiconductor parameter analyzer without integration of multiple resources like power supply, LCR meter, switching matrix, voltage and current meter. Initially semiconductor parameter analyzer was designed only for measurement of semiconductor devices but now its superior performance allows I-V and C-V characterization of different materials and devices. Semiconductor parametric test has measurement capability of lowest current upto femto ampere and highest capacitance upto μF . The Source Measure Unit (SMU) is the basic component of parameteric analyzer which integrates the voltage/current source and voltage/current meter in a single module. Two types of SMU configuration is designed for current-voltage measurement. Source I and measure V SMU configuration is a static combination of current source with parallel voltmeter which gives high-impedance current. Another SMU configuration, source V with measure I consist voltage source with an ammeter in a series and it provides low-impedance voltage source. These configurations annihilate the voltage drop between the test cables or SMU connections which is exhibited in Fig. 3.15(a) and (b). Fig. 3.15(c) demonstrate the simplified configuration of switching matrix with SMU connections for I-V and C-V measurements. Compliance limits the maximum current and maximum voltage which appears across the devices and

ment parameters step size, integration cycle, compliance value and voltage range can be varied by using GUI interface software. It has capability of characterization of complex devices quickly with 100s of application tests and each data is stored automatically in a unique built-in database after measurement with different test conditions. The workspace ensure the security of data information and saved application test can be performed later with different devices. Keysight B1500A analyzer is a quick and versatile tool for I-V and C-V measurement of devices.

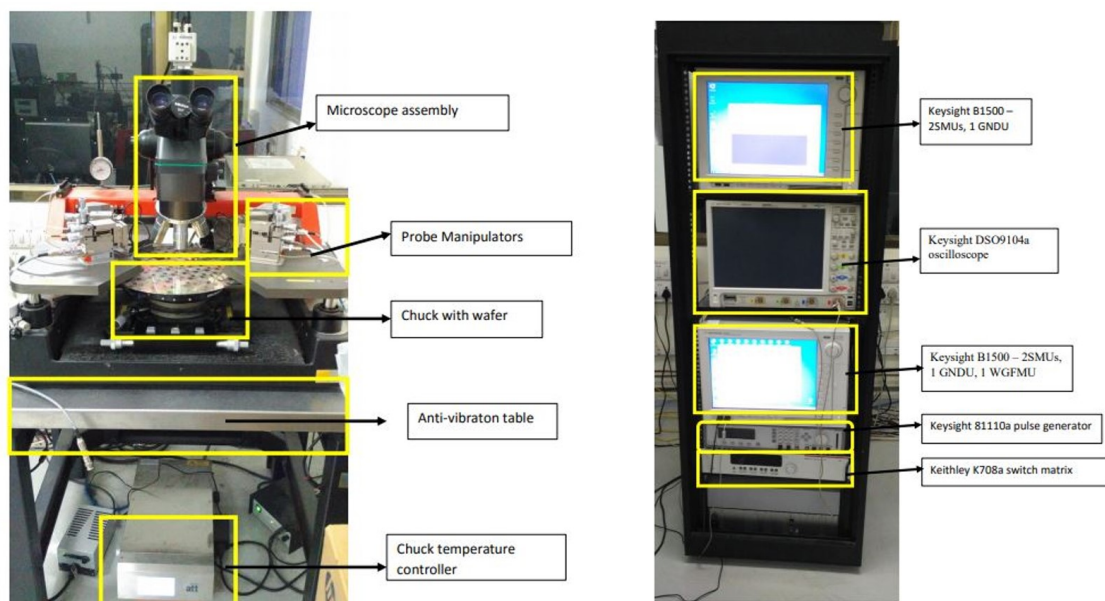


Fig. 3.16. Measurement setup of Agilent B1500 Semiconductor Device Analyzer for I-V and C-V characterization at different temperature. Photograph is taken from IIT Bombay Fabrication Facility website (URL: http://www.cen.iitb.ac.in/slotbooking/GLIMPSE/125_GLIMPSE.pdf).

For low temperature measurement, cryogenic probe station (cXCRX-4K) was used. Lowest temperature of 6 K was used for I-V characterization of our nanoribbon devices.

3.9 Summary

This chapter describe the experimental and characterization techniques used in this work. Preparation of graphene on SiO₂ substrate for device fabrication is described. The device fabrication techniques electron beam lithography and thin film deposition sputtering reviewed briefly. Physical characterization techniques optical microscopy, SEM, AFM,

Raman spectroscopy and Raman mapping are discussed in this chapter. These techniques were used for characterization of graphene and graphene nanoribbon devices. The semiconductor device analyzer is also described which were used for electrical characterization of devices.

Chapter 4

Graphene Nanoribbon Transistors with High I_{ON}/I_{OFF} Ratio and Mobility

In this chapter, we report on the fabrication of GNR transistors by Pt catalyzed etching along crystallographic directions. Transistors were characterized at room temperature and also at 6 K. Excellent I_{ON}/I_{OFF} ratio and carrier mobilities are demonstrated. We have benchmarked our data to those reported in the literature. It is seen that the performance parameters we have obtained are the best reported so far for catalytically etched GNRs and superior to those etched by other techniques. This indicates the high quality of edges of the GNR etched by Pt catalytic etching.

4.1 Synthesis of Metal Nanoparticles

Transition metals such as Fe, Cu, Ni and Pt act as a catalyst for etching of graphene [151]. These transition metal nanoparticles can be used for catalytic etching of graphene at high temperature. High temperature is required for etching of graphene due to high dissociation energy of carbon-carbon bonds (478 kJ/mole) in graphene [47]. Metal nanoparticles weaken the carbon-carbon bonds, dissociate the H_2 molecules into two H radicals and catalyze the formation of C-H bonds [152, 153]. CH_4 is formed at the end of this sequence and released to the ambience of the reaction chamber. For catalytic etching of graphene, size of metal nanoparticles must be in the range of 5-100 nm. In this work, Ni and Pt nanoparticles were synthesized by electroless plating and sputtering followed by thermal annealing.

4.1.1 Synthesis of Metal Nanoparticles by Electroless Plating

Ni nanoparticles were synthesized by electroless plating method using Ni plating solution ($\text{NiCl}_2 \cdot 6\text{H}_2\text{O}$ (30 g/l) + NH_4Cl (50 g/l) + $(\text{NH}_4)_2\text{HC}_6\text{H}_5\text{O}_7$ (65 g/l) + $\text{NaH}_2\text{PO}_2 \cdot \text{H}_2\text{O}$ (10 g/l)) [154]. First, Ni plating solution, which is green in color, was heated at 90°C . Ammonium hydroxide was added slowly to Ni plating solution till green color changed into blue color. Graphene transferred on SiO_2 sample was kept in this solution for 30 sec and rinsed with DI water. Cluster of nanoparticles were observed on graphene samples in SEM which is shown in Fig. 4.1(a). Residue of solvent was also observed on surroundings of nanoparticles. Rectangle shaped metal nanoparticles of size 100 - 220 nm were observed as shown in Fig. 4.1(b). These large nanoparticles are not suitable for graphene etching as they are not likely to diffuse on surface, and due to solvent residue contamination. Thus electroless plating method may not be used for synthesis of metal nanoparticles for our application.

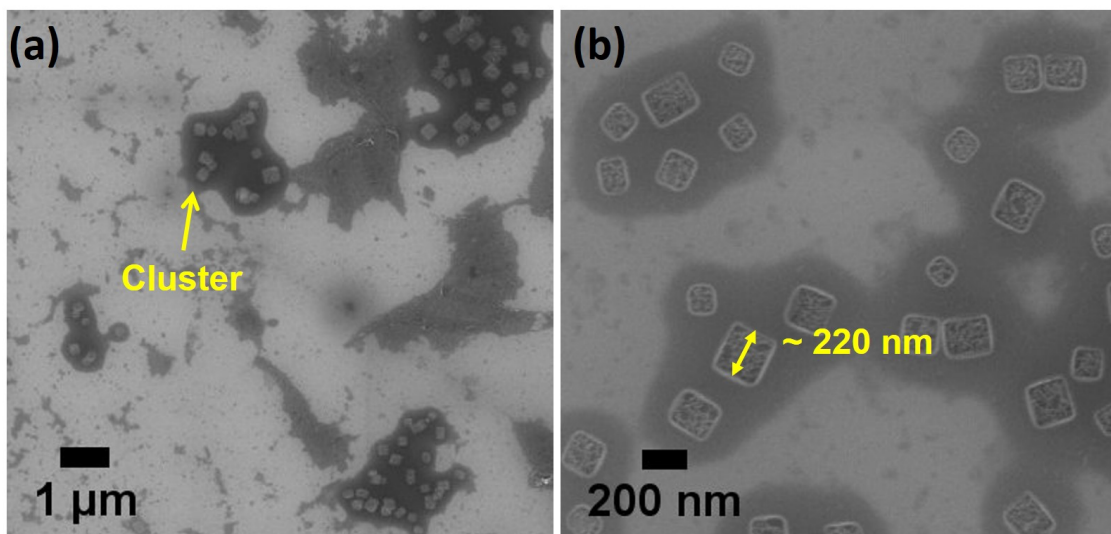


Fig. 4.1. (a) SEM images of clusters of Ni nanoparticles. Solvent residue is also visible around clusters of nanoparticles. (b) Ni nanoparticles are seen to be of rectangular shape and have size in the range of 100 - 200 nm.

4.1.2 Synthesis of Metal Nanoparticles by Sputtering and Thermal Annealing

In this method, a thin film of Ni (3-5 nm) was deposited on SiO₂ substrate by RF sputtering at 35 W (5 min.) in high vacuum of 2×10^{-7} mTorr. After thin film deposition, sample was annealed at 500°C in Ar : H₂ in the ratio of 70 : 30 ambient for nanoparticles synthesis. Nanoparticles with size of 5-150 nm were uniformly distributed on SiO₂ substrate which is shown in Fig. 4.2.

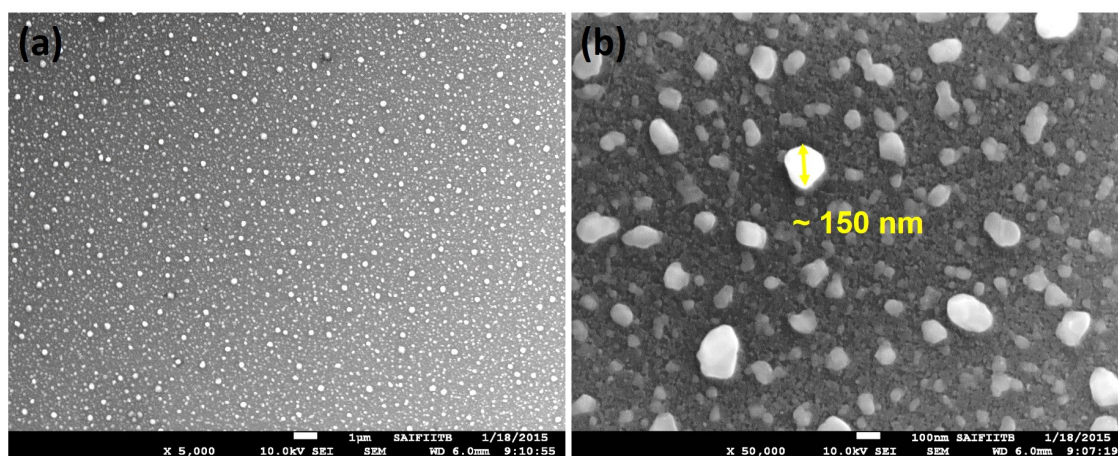


Fig. 4.2. (a) SEM image of Ni nanoparticles synthesized by sputtering. (b) 5-150 nm size of Ni nanoparticles. 150 nm size of Ni nanoparticle is shown by yellow marker.

Out of these two synthesis methods, sputtering followed by annealing method is a better method than electroless plating for our application. Sputtering followed by annealing method produce smaller size of nanoparticles with uniform distribution which is required for etching of graphene. Thus sputtering followed by annealing method was used for synthesis of Ni and Pt metal nanoparticles in subsequent work.

4.2 Why Pt-assisted Etching of Graphene

The narrow width and regular smooth edges of GNRs are difficult to obtain in practice. Top - down methods like STM lithography [42], unzipping of carbon nanotubes by strong acid treatment [44], and patterning of graphene by electron beam lithography [45] damage the GNRs and edges of GNRs. Edge distortions in GNR could lead to lower carrier mobility. Thus bottom-up approaches like chemical synthesis [46] and metal catalyzed

anisotropic etching using Ni, Fe, Cu [47] have been explored for fabrication of GNRs with smooth and achiral edges.

In anisotropic etching, transition metals are used as catalyst nanoparticles at high temperature for etching of graphene. It is essentially an exothermic reaction, which is the reverse reaction of the CVD graphene growth. In CVD growth, methane gas dissociates to carbon and hydrogen at high temperature, and makes graphene sheets on metal substrates. Here, etching process is driven by hydrogenation reaction and produce methane by reaction of hydrogen with carbon, the carbon being absorbed by metal nanoparticles from graphene edges [47, 79]. This catalyst activity depends on carbon solubility in the metals. Pt offers several advantages compared to Cu, Ni, and Fe for this application. Carbon solubility is higher in Pt than in Ni, Fe and Cu [47, 155]. Pt nanoparticles do not remain on graphene surface after etching because of physisorption. Ni nanoparticles stick on graphene surface due to chemisorption. Pt-C interface has greater misfit than Ni-C interface that will induce the breaking of bonds [156, 157]. Pt is not easily oxidized, making the process easier to control and reproduce.

4.3 Fabrication of GNR Field-Effect Transistors

CVD graphene on copper foils (purchased from Graphenea S.A.) were transferred using Cu etchant on to 90 nm SiO₂ thermally grown on Si (p-type, (100) surface orientation). Graphene was also prepared by mechanical exfoliation from highly oriented pyrolytic graphite on identical substrate. Subsequently e-beam sensitive resist is spin coated and rectangular windows were opened in the resist by e-beam lithography (Raith 150^{Two}). Ultra-thin films of Pt (2 nm) and Ni (2 nm) were deposited by RF sputtering. After a lift off process to obtain 1 μ m wide Pt and Ni lines, samples were annealed at 500°C in H₂ + Ar in ratio of 30 : 70 to form Pt and Ni nanoparticles. The top view schematic of GNRs fabrication by electron beam lithography is described in Fig. 4.3.

The process flow is summarized in Fig. 4.3 using Pt for illustrations. Pt nanoparticles can be seen in Fig. 4.4(b). These metal nanoparticles etch or cut the graphene at high temperature (1050°C) in H₂ + Ar ambient. The metal-assisted etching process is the catalytic hydrogenation of carbon at high temperature where Pt or Ni dissociate the carbon from graphene edges and produce methane by reaction of carbon with hydrogen.

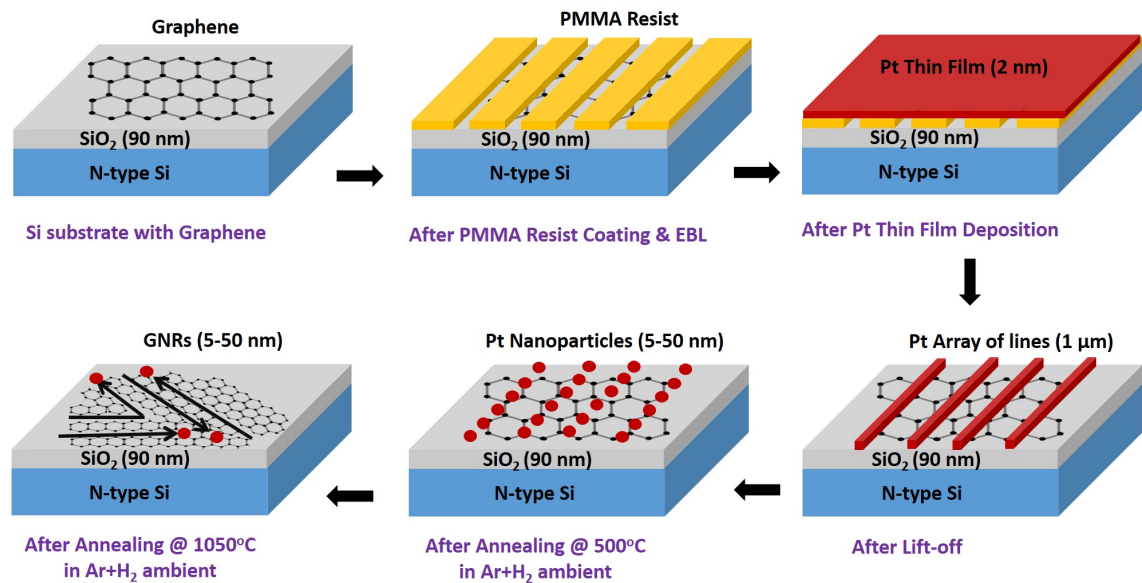


Fig. 4.3. Schematic of GNRs fabrication by electron beam lithography.

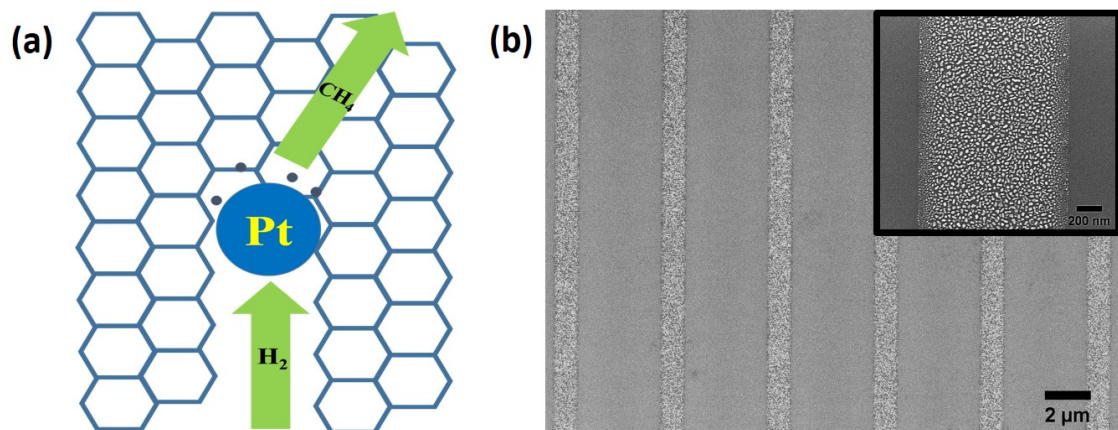


Fig. 4.4. (a) Cartoon of cutting of graphene by Pt nanoparticles. (b) Array of 1 μm linewidth of Pt nanoparticles after annealing at 500°C.

This mechanism is represented in Fig. 4.4(a). If the metal crystal is sufficiently small, it has high surface area and high mobility at high temperature on SiO₂ and other dielectrics. This effect would result in patterning of the graphene by metal nanocrystals at high temperature.

The bottom-gate transistors were fabricated by electron-beam lithography. The locations of the graphene nanoribbons were identified by SEM imaging using the Raith 150^{Two} system. Source - drain contact structures were then defined for the identified GNRs. The source-drain electrodes (Ti-10 nm/Au-50 nm) were patterned on GNRs by lift-off process.

These metals were deposited using a 6-target e-beam evaporator at very high vacuum (5×10^{-7} mTorr).

4.4 Results and Discussion

Catalytic etching by Pt was compared in both CVD (Fig. 4.5(a)) and exfoliated graphene (Fig. 4.5(b)). Figure 4.5(a) shows that etching is randomly oriented in CVD graphene. In CVD graphene, etching may happen along the grain boundaries or damaged lines arising due to adhesion problem with SiO_2 , cracks, and foldings that arise during transfer process, etc.

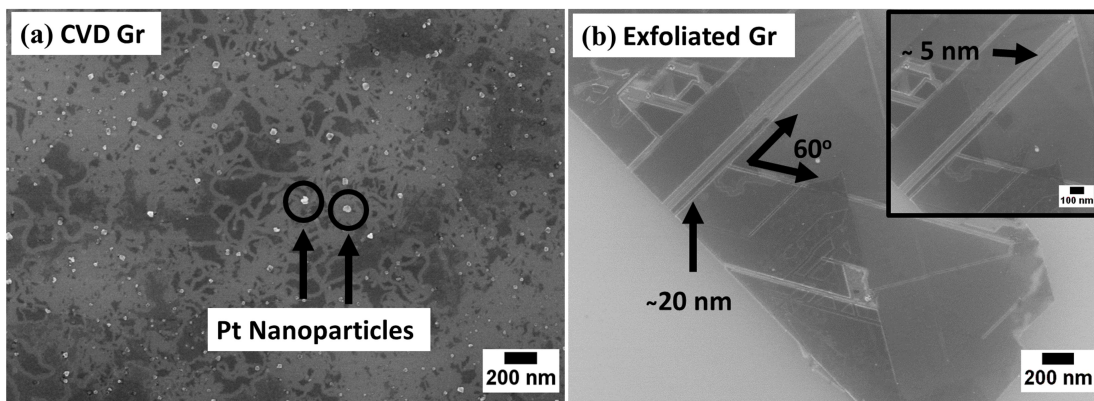


Fig. 4.5. SEM image of (a) etched CVD graphene (b) Etched exfoliated graphene show sub-10 nm and ~ 20 nm GNRs (shown by black arrows). Pt nanoparticles also shows etching in 60° crystallographic orientation angle.

Large crystal domains and careful transfer processes would be desirable if the catalytic etching has to be employed for large scale synthesis of GNRs using the CVD route. Pt was not removed after etching process because Pt nanoparticles density is less near the edge of GNR and some GNRs does not have Pt nanoparticles on the edges of graphene nanoribbons which is shown in Fig. 4.6. The initial width of Pt lines was $1 \mu\text{m}$.

We observed difference between nanoribbons etched using Ni and Pt nanoparticles as shown in the Fig. 4.7. It may be noted that Pt etches graphene without leaving residues unlike Ni. This is because Ni is chemisorbed on graphene whereas Pt is physisorbed [157]. The solubility of carbon in metals are directly related to catalytic reaction (metal-catalyzed gas-carbon reactions). From the previous reports on metal catalyst reactions

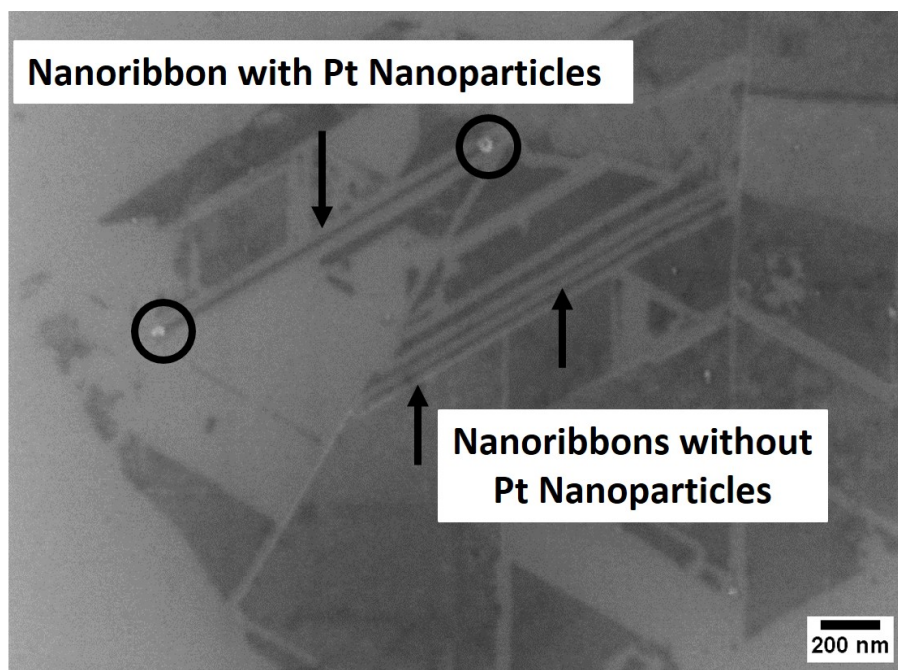


Fig. 4.6. SEM image of etched exfoliated graphene. One nanoribbon with two Pt nanoparticles (black circle with arrow) at the edges is shown and other three nanoribbons do not have any nanoparticles at the edges shown by black arrows.

with graphite, carbon dissolves in metal from the edges of graphite because the edge atoms of graphite are unsaturated and active [157]. Thus, carbon solubility is an important factor for etching of graphene and it depends on temperature also. Solubility of metals increase with the temperature and high temperature is needed for breaking of carbon-carbon bond. Palladium has closer value of solubility to Pt, so Pd can also be used as a catalyst [155].

AFM of etched CVD graphene (Fig. 4.8) was also performed to study etching of CVD graphene. It was observed that etching is randomly orientated in CVD graphene due to wrinkles and grain boundaries. The movement of nanoparticles is restricted because the nanoparticles are located at the grain boundaries and wrinkles.

In exfoliated graphene, etching proceeds along crystallographic orientations (30° , 60° , 90° , 120° and 150°) due to low density of defects. At certain locations, it is seen that two nanoparticles etch graphene along parallel lines leading to the formation of nanoribbons. In Fig. 4.9(c) sub-10 nm nanoribbons can be observed. Etching in specific orientation (zigzag or armchair) occur because Transition Metal (TM)-zigzag/armchair interface is more stable than other interfaces. This is because zigzag and armchair edges have all

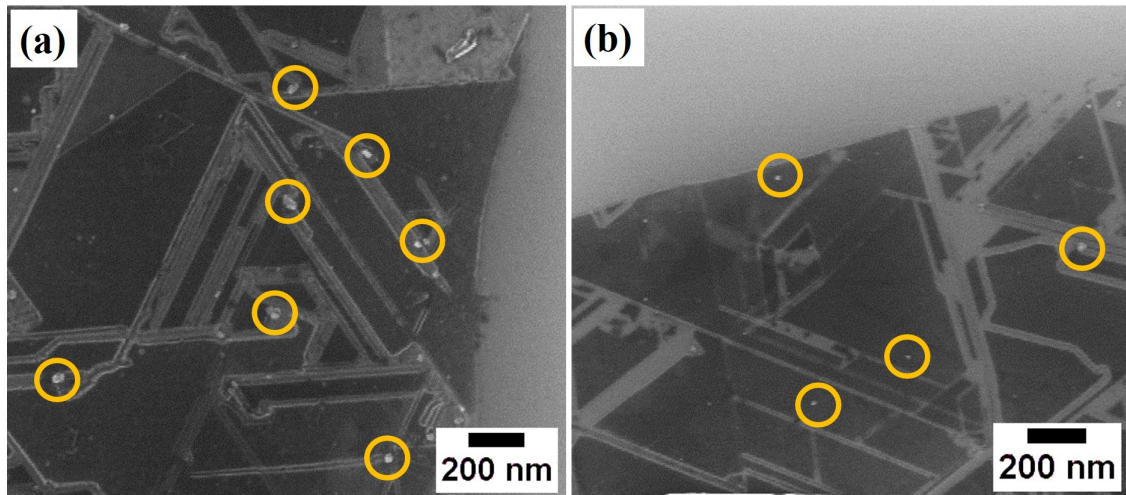


Fig. 4.7. SEM image of etched exfoliated graphene by (a) Ni nanoparticles and (b) Pt nanoparticles. Nanoparticles are highlighted by yellow circles.

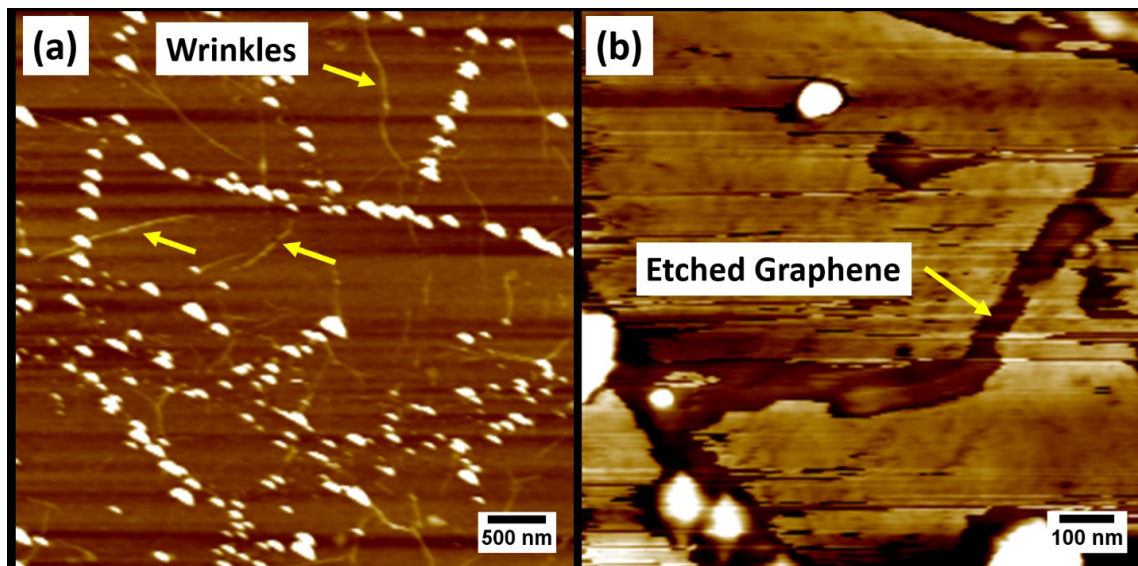


Fig. 4.8. AFM image of etched CVD graphene. (a) Wrinkles of CVD graphene are shown by yellow arrows. (b) Etched graphene area is shown by yellow arrow. The etching of CVD graphene is randomly orientated. White particles are Pt nanoparticles.

atoms in a straight line (a strong bonding between armchair (zigzag) edge atoms with TM surface). So, nanoparticles should be aligned in armchair and/or zigzag directions along graphene channel [158]. Another reason of cutting of graphene in armchair and zigzag directions is because Pt-graphene interface is more stable than hydrogen terminated graphene edges at high temperature. The overall reaction rate of the catalytic hydrogenation of carbon is limited by the reaction of carbon with platinum that results in the

breakage of carbon - carbon bonds and the removal of a carbon atom from the graphene lattice.

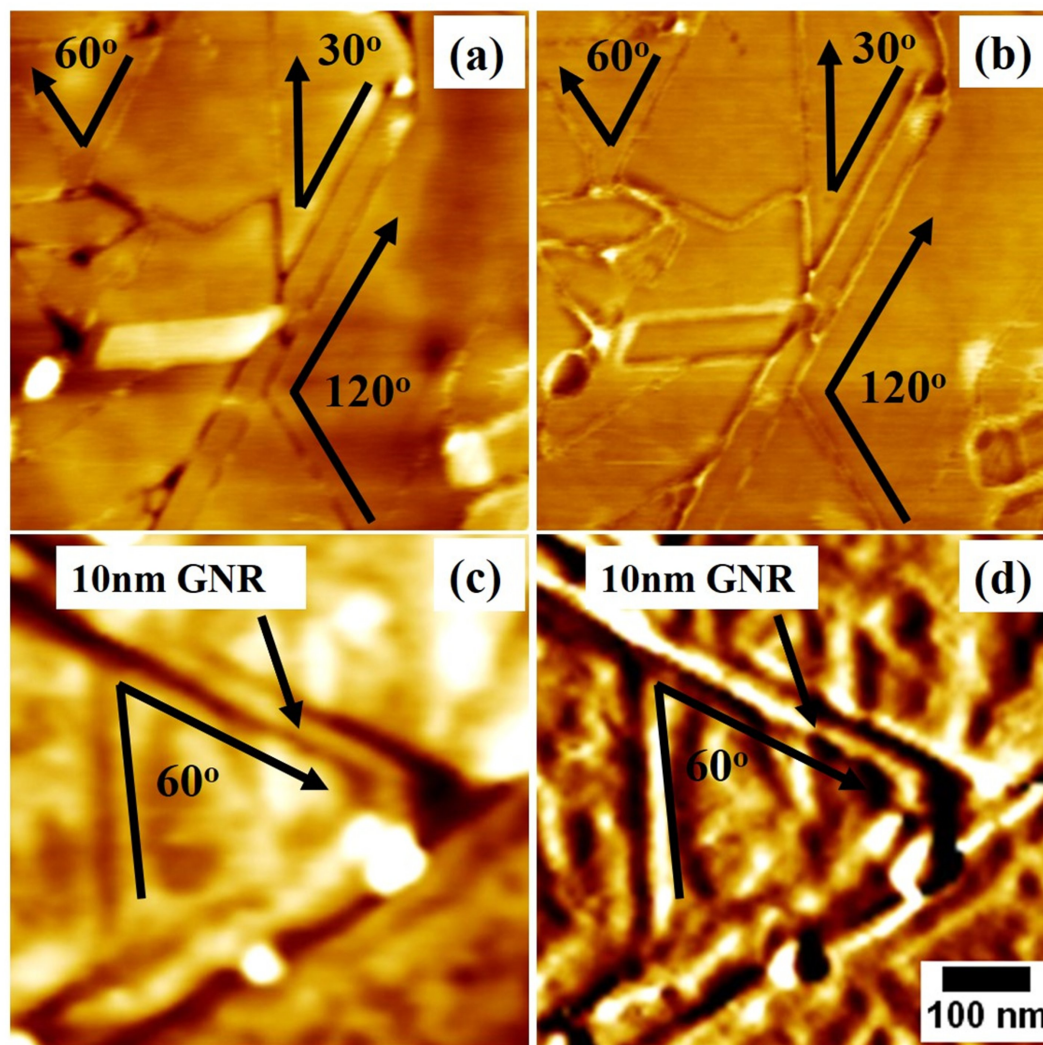


Fig. 4.9. Pt nanoparticle assisted etching of graphene (a) AFM topography image of etched graphene that shows chirality preserving angles 30° , 60° and 120° . (b) AFM phase image of etched geometric nanostructures. (c) AFM topography image showing chirality angle 60° and 10 nm GNR. Pt nanoparticles do not cross previously etched trenches or region. (d) AFM topography image of etched trenches. White particles are Pt nanoparticles.

Pt require 2.23 eV activation energy for catalytic hydrogenolysis of carbon at high temperature [80]. During this catalytic reaction, nanoparticles make trenches on graphene surface which has the width equal to nanoparticle diameter (5 - 50 nm). Fig. 4.9(a) and 4.9(b) show the AFM topography and phase images respectively, and confirms chirality

angles of 60° and 120° . Trenches also produced connected geometries. Interestingly, 10 nm or sub-10 nm Pt nanoparticles do not intersect their etching lines. Instead the nanoparticles turn as they approach other nanoparticles as shown in Fig. 4.10. This is attributed to Coulomb interactions between the metal nanoparticles that are charged due to the graphene-metal work function difference [79]. Nanoparticles etch two edges at different times and sometimes etch at the same time and make nanoribbons.

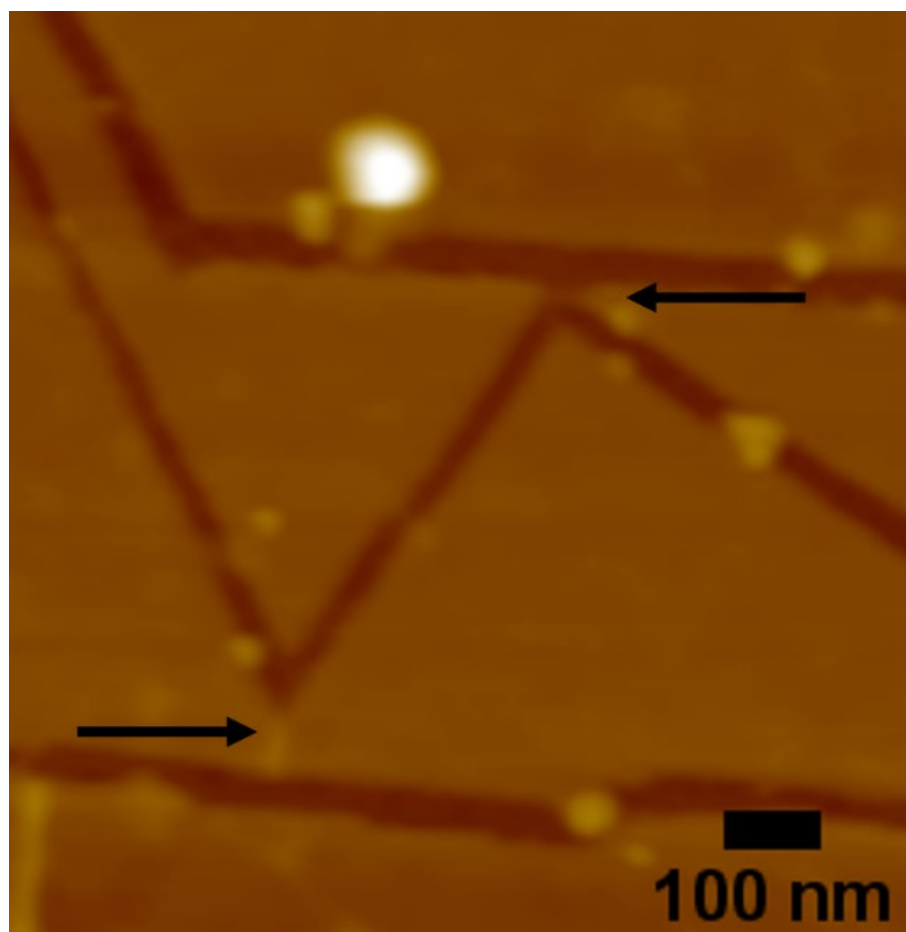


Fig. 4.10. AFM image of etched graphene. The black arrows are showing that nanoparticles do not etch previously etched trench and turn away from it. The etched trench turns away in nanometer distance because of Coulombic interactions. White particles are Pt nanoparticles.

Pt nanoparticles along 60° or 120° angles, move along symmetric directions (same crystallographic orientations along equivalent directions $[1\ 1\ \bar{2}0]$ have both edges, either armchair or zigzag) as is shown in Fig. 4.9(c). Chirality angles 30° , 90° and 150° have different crystallographic orientations along $[1\ 0\ \bar{1}0]$ (one edge armchair and another one zigzag) [80]. Thus, in our case chirality is preserved by Pt nanoparticle etched GNR

edges. Etching density strongly depends on the etching temperature and H₂ concentration. The reason of high etching temperature requirement is higher dissociation enthalpy of carbon-carbon bond in graphene (478 kJ/mole) than C - H bond in CH₄ (435 kJ/mol) [47]. H₂ concentration was optimized for obtaining GNRs. Low concentration of H₂ (5% H₂) was found to be insufficient for etching of graphene. When the concentration was high (50% H₂) large area of graphene was found to be etched. An optimum was found at 30% H₂ concentration.

In this etching process, graphene is etched along particular crystallographic directions by nanoparticles. The atomic level controlling of etched graphene edges is the key advantage of crystallographic etching. During this catalytic reaction, nanoparticles make trenches on graphene surface which has the width equal to nanoparticle diameter (5 - 50 nm). Pt catalyzed reaction rate or rate of methane production is proportional to the surface area of the catalyst metal nanoparticles. High surface area of catalyst nanoparticles catalyze more C-H bond formation. Larger size nanoparticles channeled at higher speeds, indicates limited surface reaction rate [159, 160]. There is no correlation between nanoparticles width and graphene nanoribbon width. Small size nanoparticles (2-20 nm width range) make smaller cutting width than larger nanoparticles size (>20 nm). The cutting width increase with the nanoparticle size and follow the parabolic path after 20 nm nanoparticle size [161].

Raman spectroscopy was performed before and after etching process and the results are shown in Fig. 4.11(a). Raman spectrum was taken before the formation of contacts. 532 nm Ar-ion laser was used for Raman measurement and laser spot size was 1 μm . The Raman spectrum of etched graphene shows D peak (1350 cm⁻¹). In general, D-peak appears because of defects, grain boundaries and armchair edges of graphene [149, 150, 162]. Raman spectrum of GNR has polarization dependence (Fig. 4.11(b)) [60]. D-peak intensity increase when incident laser light is polarized parallel (VV configuration) to the direction of nanoribbons and decrease when incident laser light is polarized to normal GNR direction (VH configuration) [150]. Thus, here the D-peak intensity increased most likely due to the edge effect of GNRs, and not from defects. It was also observed that 2D peak intensity was resilient to Pt catalyzed etching.

We have performed the Raman mapping of etched exfoliated and CVD graphene. D-band mapping of etched exfoliated and CVD graphene are shown in Fig. 4.12. The

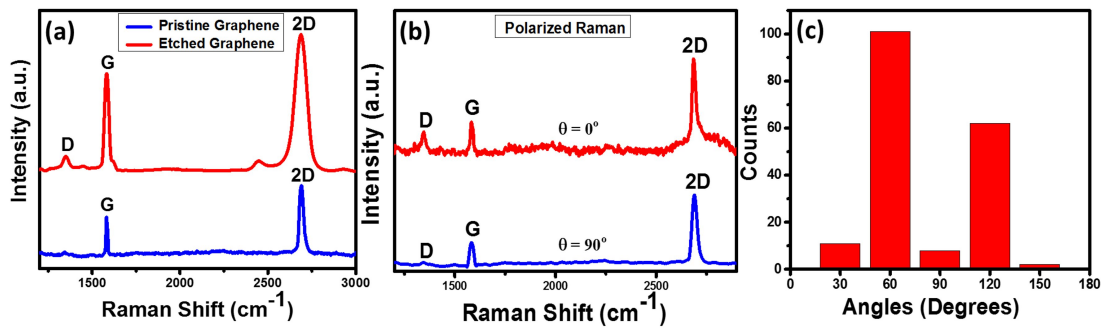


Fig. 4.11. (a) Raman spectra of pristine graphene before etching and after Pt catalyzed etching. (b) Polarized Raman spectra of etched graphene. (c) Statistics of angles that preserve crystallographic orientations. Most of the trenches make 60° and 120° angles that have identical crystallographic orientations (zigzag or armchair).

D band intensity has correlation with edge chirality. The armchair edge has stronger intensity than zigzag [80]. In D-band mapping, higher D-band intensity (magenta color) is shown by black arrows and less intensity is shown by red color. Other areas like light blue color show etched graphene area. In etched CVD graphene (Fig. 4.12(a)), large magenta area indicates random orientations of etching and less magenta area of exfoliated graphene indicates the specific orientational etching. Higher intensity of D band indicates the armchair edge signature and less intensity might be due to zigzag edges. Precise determination of edge chirality of etched graphene by mapping is difficult because nanoribbons are closely spaced. So, these etched graphene nanoribbons are with a mixture of armchair or zigzag edges.

The characteristics of the transistors fabricated with the GNR as channel are shown in Fig. 4.13 and 4.14, along with the SEM images of the transistors. The transistor shown in Fig. 4.13(c) has GNR with a width of 15 nm. The device shows nonlinear characteristics with low conductance at room temperature. The I_{ON}/I_{OFF} ratio depends on temperature that can be expressed as $I_{ON}/I_{OFF} \propto \exp(E_g/k_{BT})$ [66]. I_{OFF} is relatively high at room temperature due to thermionic emission. Thermionic emission current is suppressed at low temperature and the dominant leakage mechanism would be tunneling. At low temperature, electrons tunnel through the barrier which form at the contact [66]. At the contact, electrons tunnel through the GNR gap or hop through the defect states and that enhance the I_{ON}/I_{OFF} ratio [18, 66]. The transistor shows an I_{ON}/I_{OFF} ratio of 600 at room temperature. The output characteristics show negative slope as the drain voltage

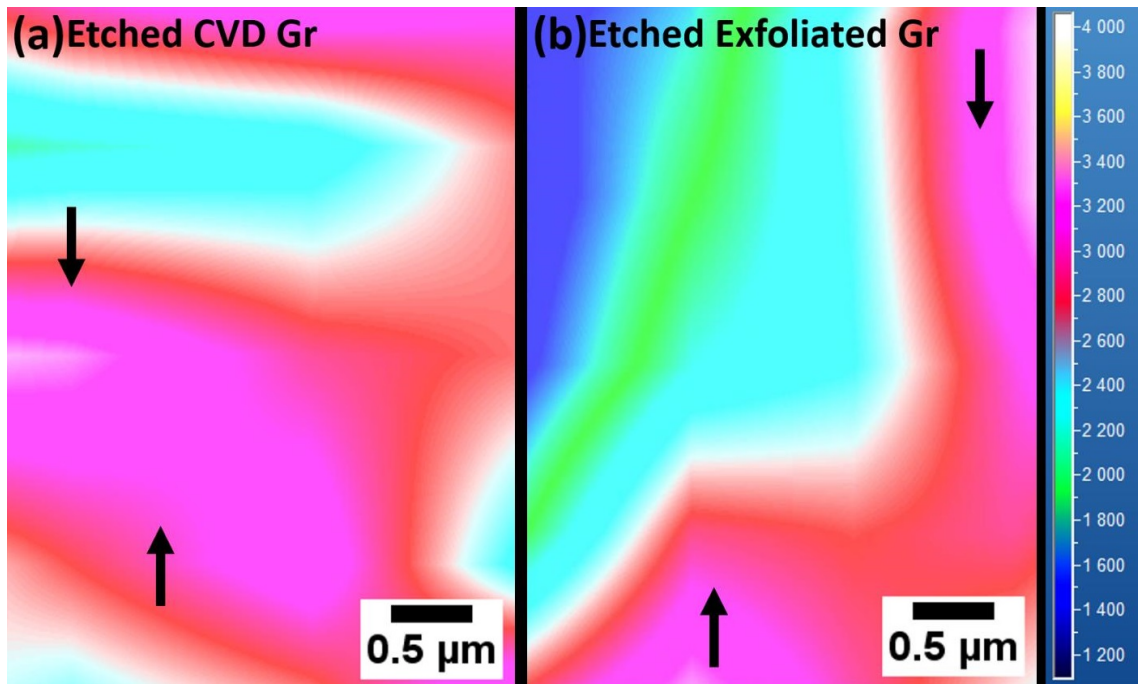


Fig. 4.12. D-band Raman Mapping of etched CVD and exfoliated graphene. Black arrows are showing higher D-band intensity (magenta color) and less intensity is shown by red color.

increases. This could be due to charge traps in the oxide due to short channel length [163] or self-heating effects which can be a result of contact thermal resistance and phonon boundary scattering [164, 165].

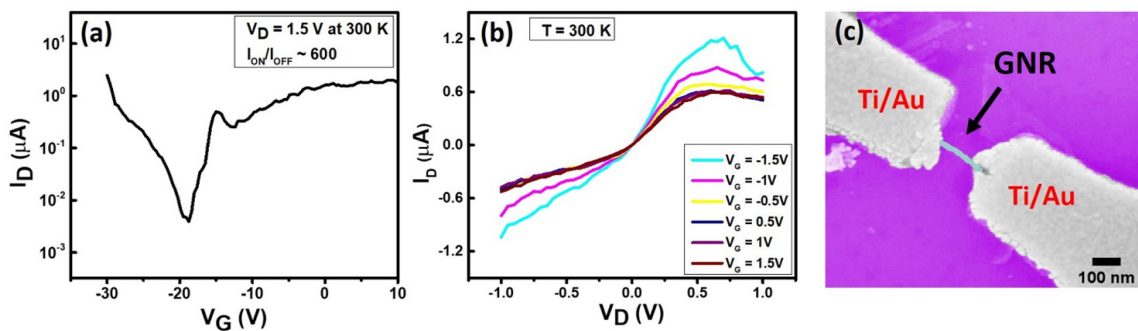


Fig. 4.13. (a) Transfer characteristic (drain voltage 1.5 V) and (b) output characteristics of ~ 15 nm wide GNR. Transfer characteristic shows ~ 600 on/off ratio. (C) SEM image of device with Ti-Au electrodes. The channel length is 110 nm.

Fig. 4.14 shows the characteristics of a transistor with GNR of width of 18 nm at 6 K. Fig. 4.14 (a) shows substantial gate modulation at low V_D due to Fermi level movement controlled by back gate voltage. Electron mobility of $400 \text{ cm}^2/\text{Vs}$ and hole

mobility of $1100 \text{ cm}^2/\text{Vs}$ were extracted. I_{ON}/I_{OFF} ratio of 2×10^7 is calculated from Fig. 4.14(a). These results are benchmarked to the results reported in the literature, in Table 1.

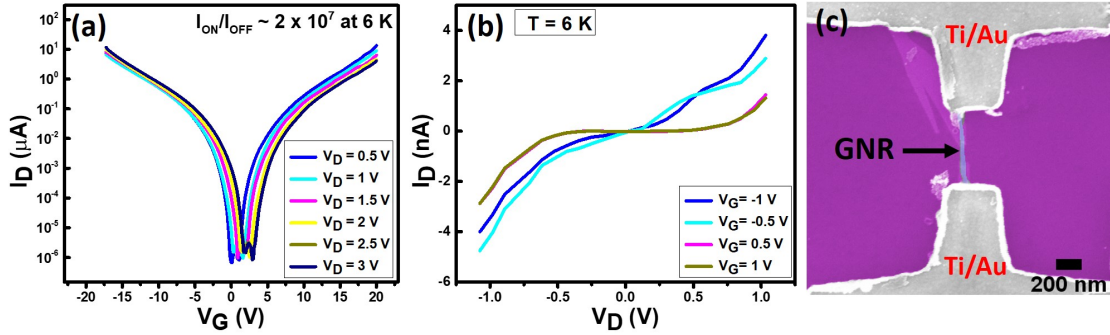


Fig. 4.14. (a) Drain current as a function of gate bias at different drain voltages for $\sim 18 \text{ nm}$ wide GNR device. Transfer characteristic shows high on/off ratio of 2.2×10^7 . (b) Drain current as a function of drain voltage. (c) SEM image of device with Ti-Au electrodes. The channel length is 500 nm .

We characterized the I_{ON}/I_{OFF} ratio of few GNR transistors at 6 K for various ribbon widths (Fig. 4.15). The I_{ON}/I_{OFF} is seen to increase exponentially as the ribbon width decrease below about 22 nm . From this, it can be concluded that the effect of confinement in graphene nanoribbons would appear below 22 nm width at 6 K . The trend is consistent with that reported by X. Li et al. [18], though the values obtained in our experiment are much higher for I_{ON}/I_{OFF} and smaller for the critical width of the nanoribbon. Li et al. synthesized graphene nanoribbons by sonication of graphite in 1,2-dichloroethane (DCE) solution of poly(m-phenylenevinylene-co-2,5-dioctoxy-p-phenylenevinylene) (PmPV).

Bandgap of various width of GNRs were also extracted at different temperature using $I_{ON}/I_{OFF} \propto \exp(E_g/k_B T)$ [66] which is shown in Fig. 4.16. At low temperature 6 K , intrinsic bandgap values of GNR enhanced because of hopping through localized states. The bandgap decreases as ribbon width increases in Fig. 4.16 which confirms the theoretical predictions [22]. So, this is also an indication of the high quality with low defects of GNRs that preserve electrical characteristics of graphene.

For theoretical calculation of hole and electron mobilities of nanoribbons, many fitting parameters are needed for Density Function Theory (DFT) and Non-equilibrium Greens Function (NEGF) calculation for GNR device. Bandgap engineering and quantum

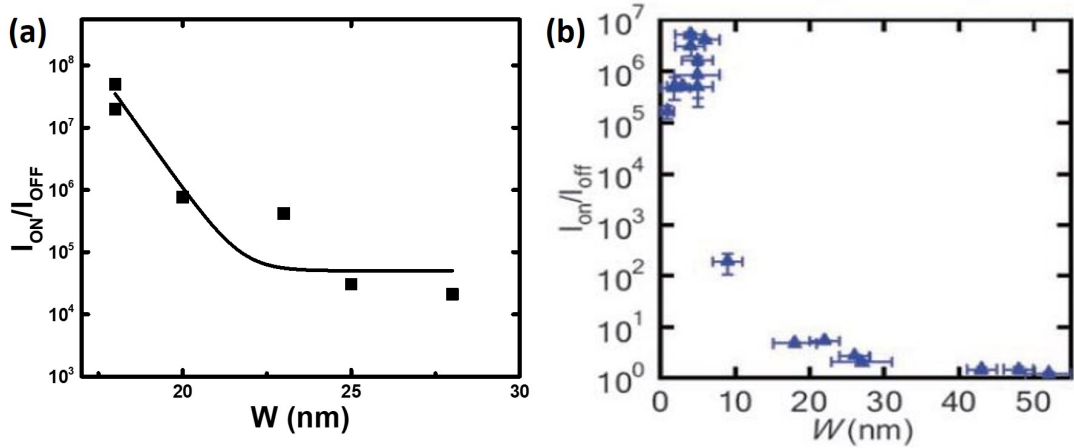


Fig. 4.15. (a) Device performance of graphene nanoribbon field effect transistors. The I_{ON}/I_{OFF} ratio of various ribbon widths for $V_D = 0.5$ V at low temperature 6 K. (b) Data from Li et al. [18].

transport approach could be needed for mobilities calculation. It is complex to be modeled because of iterative process and its takes longer time for computations.

To the best of our knowledge, the carrier mobility of GNRs have been calculated to study scattering mechanism by using theoretical modelling. In literature, carrier mobility has been calculated at room temperature for wide nanoribbons and at low temperature for sub-10 nm GNRs [166, 167]. Our work, reports high mobility of 18 nm GNRs at low temperature. Direct Transconductance Method (DTM) was used for the extraction of mobility. In DTM, mobility is extracted from the gate voltage dependent transconductance.

$$\mu_{DTM} = g_m L / (W V_{ds} C_g) \quad (4.1)$$

where $g_m = dI_{ds}/dV_g$ is transconductance and the mobility μ_{DTM} is the field-effect mobility. L and W are the channel length and width. C_g is the gate capacitance [168]. For comparison of experimental and theoretical mobility of GNRs, we compared the room temperature mobility of GNRs with mobility reported in the literature. The experimental mobility has comparable value with theoretical mobility (Fig. 4.17) [166, 167, 169, 170].

The carrier scattering study is essential to improve transport properties of GNRs. But, there is no experimental study on scattering mechanism of GNRs at different temperature till now. The analytical study of all scattering mechanisms namely surface im-

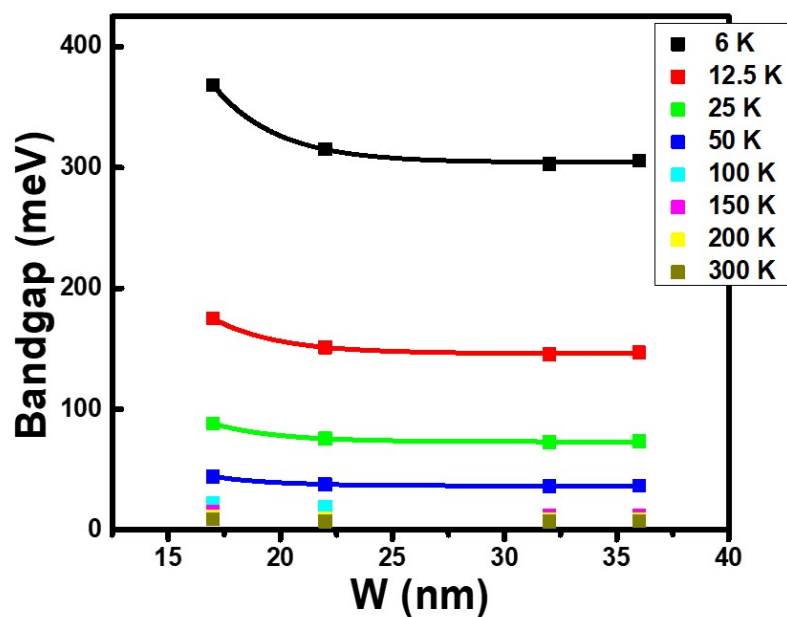


Fig. 4.16. Bandgap as a function of ribbon width at different temperature.

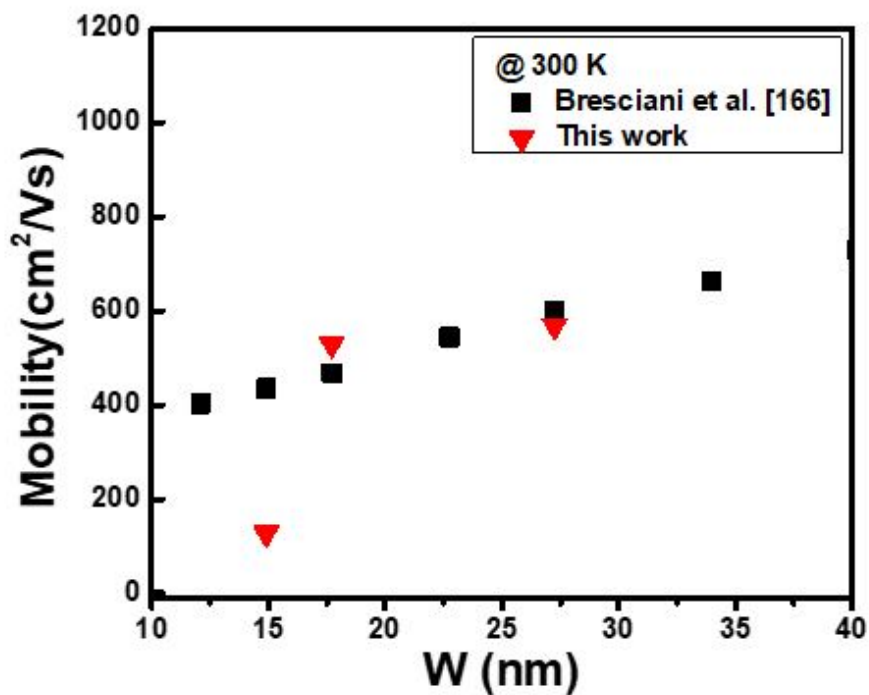


Fig. 4.17. The mobility of GNRs as a function of width of nanoribbons. Mobility of GNRs decrease with ribbon width because of edge scattering and acoustic phonon scattering.

purity scattering, acoustic phonon and Line Edge Roughness (LER) scattering in 3 and 5 nm GNR have been reported at different temperatures as a function of mobility [167]. The surface impurity scattering and acoustic phonon scattering limit the mobility at room temperature, and LER scattering dominates at low temperature and is felt in the absence of surface impurity. The LER scattering is more sensitive in ribbon width less than 5 nm [166, 171]. The detailed scattering mechanism of GNRs wider than 5 nm have not been addressed in the literature. Theoretical study of scattering mechanisms dominant in the width regime experimented in this thesis could be under taken in the future.

In this work, high quality of GNRs may be arising due to the etching of the graphene along crystallographic directions. I_{ON}/I_{OFF} ratio is a figure of merit (FOM) indicative of the bandgap. However, for transistor applications, mobility is also a very important performance parameter, which can be negatively influenced by the edge roughness of the GNR. A careful study of Table 1 indicates that the I_{ON}/I_{OFF} and the mobilities we have obtained are among the highest values reported for GNR devices patterned by metal assisted etching. Also, the performance of our devices exceeds those of GNR patterned by other techniques. These results are in tune with the high quality of the GNR assessed using Raman spectroscopy studies.

4.5 Summary

We have demonstrated high performance graphene nanoribbon transistors. Two metal nanoparticle synthesis methods, electroless plating and sputtering followed by annealing are described. In our work, metal nanoparticles (Ni and Pt) were prepared by sputtering and annealing method over electroless plating due to smaller size nanoparticles formation with uniform distribution by sputtering and annealing. GNRs were prepared by Ni and Pt-assisted etching of exfoliated graphene using hydrogen at high temperature. Pt-assisted etching is better than Ni-assisted etching due to higher carbon solubility and physisorption of Pt on graphene. The etching behavior were compared in exfoliated and CVD graphene. No GNRs were observed in CVD graphene. GNRs with width of sub - 10 nm and 10 - 20 nm were obtained in case of exfoliated graphene. SEM is used for understanding of etching behavior of graphene. The crystallographic orientations of etched graphene and width of GNRs are extracted from AFM techniques. Raman imaging of CVD and exfoli-

Table 4.1: Comparison of various GNR transistor characteristics reported in the literature using different fabrication methods. GNR devices fabricated using Pt nanocrystal-assisted etching shows better performance than previously reported GNR devices. DSA - Direct Self Assembly, CDL = Carbon Dimer Lines, NA - Not Available.

Fabrication Method	GNR Width (nm)	Channel Length (μm)	I_{ON}/I_{OFF}	Mobility Extraction method	Mobility (cm^2/Vs)	Transport Gap (eV)	Reference
EBL	10	2	10^6 (4 K)	DTM	800-1000	0.14	Hwang et al. [66]
EBL	12	1	10 (RT), 10^6 (4 K)	NA	NA	0.1	Hwang et al. [62]
Chemical Bottom-up Approach	30	0.9	87.5 (RT)	NA	0.0012	NA	Passi et al. [172]
Etchant Free Transfer from Au	N = 7 CDL	0.06	10^3 (RT)	NA	NA	NA	Ohtomo et al. [173]
DSA Lithography	6	NA	100 (RT)	NA	10	NA	Jeong et al. [174]
Chemical Solution Synthesis	5	0.210	6×10^6 (RT)	DTM	100-200	<0.4	Li et al. [18]
Ni Nanostructure	23	1	16 (RT), 10^4 (13 K)	NA	NA	0.0585	Kato et al. [175]
Ni Nanocrystal Catalyzed Etching	19	1.65	5000 (RT)	DTM	1.35-6.78	NA	Ago et al. [60]
Pt Nanocrystal Catalyzed Etching	18	0.5	600 (RT), 2×10^7 (6 K)	DTM	400 (electron), 1100 (hole)	0.08	This Work

ated graphene are compared to identify the chirality of graphene nanoribbon edges. High quality of the GNR demonstrated by detailed Raman spectroscopy analysis is validated by superior electrical performance, namely high I_{ON}/I_{OFF} ratio and carrier mobility. The graphene nanoribbon width is not controllable using this technique. This process is not scalable because nanoribbons formation is random and can't be used for mass manufacturing of nanoribbon devices. Our objective is to obtain the cleaned edges of high quality nanoribbons by crystallographic etching of graphene by Pt nanoparticles.

Chapter 5

Reconstruction of Fractured Graphene and GNRs by Thermal Treatment in Methane Gas and by Electron-Beam Irradiation

Graphene has high potential for electronic applications due to its remarkable properties like high charge carrier mobility ($200,000 \text{ cm}^2/\text{Vs}$ at 300 K) [3], high tensile strength (130 GPa) and high Young's modulus (1TPa) [5]. But graphene also has low fracture toughness (16 Jm^2) like a brittle solid [36]. Fracture is a severe concern for practical applications of graphene. Fracture of graphene is caused by irradiation, chemical and physical processes used for device fabrication, topography in underlying substrates [34] and electrical breakdown [90]. GNRs exhibit semiconducting behaviour which is defined by edge configurations (zig-zag and armchair). Bottom-up engineering is a promising approach to alter the shape, structure and edge configuration of graphene and GNRs. Graphene and GNRs have high current carrying capacity (10^8 A/cm^2) and high thermal conductivity, and hence are considered for replacing copper in on-chip interconnect applications [35, 125]. However, graphene and GNR have limitation of current transport due to self-heating which leads to breakdown [176]. The healing of fractured graphene and graphene nanoribbons is desirable for electronic applications [32, 48, 85].

The experimental and theoretical work on healing and reconstruction of graphene and GNRs edges were already reported [48, 85]. Jia et al. reported on the reconstruc-

tion of graphene by Joule heating and electron-beam (e-beam) irradiation in an integrated transmission electron microscope - scanning tunnelling microscope system [85]. Kulshrestha et al. [98] and Dhall et al. [99] repaired broken CNTs by e-beam irradiation in scanning electron beam systems. Reconstruction of graphene using electron beams is an attractive technique for site specific repair of damaged devices. However this is not a scalable approach for large area applications due to the low throughput. Further, electron beam systems tend to be expensive.

In this work, fracture was induced by electrical stress and it was healed by e-beam irradiation, and methane gas exposure. Reconstruction methods of fractured graphene explored in this thesis shown by a simplified ray diagram in Fig. 5.1. Fractured graphene is reconstructed by 2 methods but it is categorized in three parts - methane gas exposure, e-beam irradiation and e-beam irradiation with methane gas exposure. Electron-beam irradiation and e-beam irradiation with methane gas exposure is combined in one section of this chapter. Graphene reconstruction was confirmed by AFM, SEM and Raman Spectrum. The electrical measurement ensures restoration of current before and after graphene reconstruction.

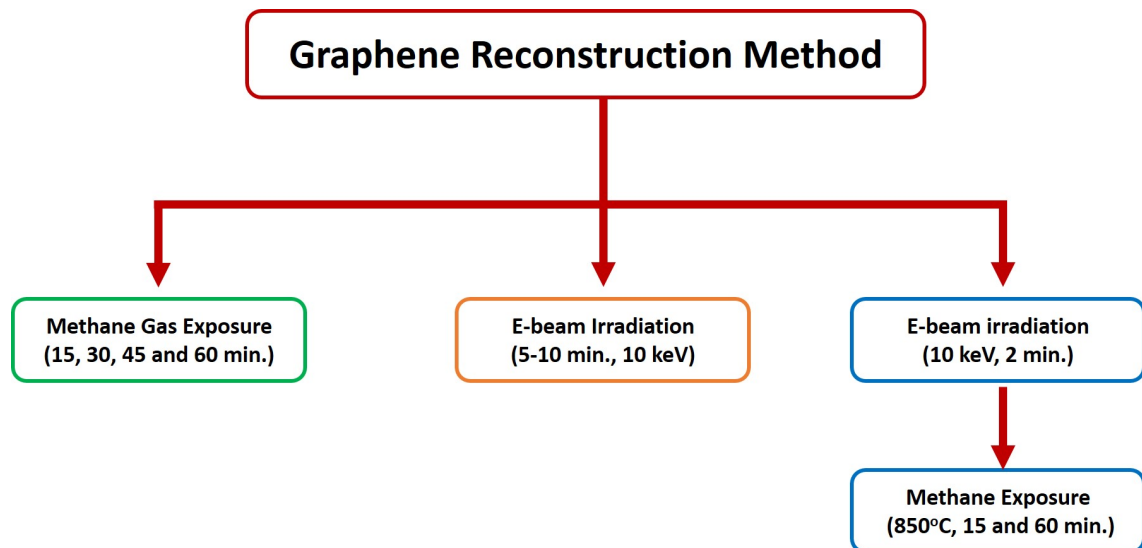


Fig. 5.1. A simplified ray diagram of graphene reconstruction methods investigated in this work.

5.1 Reconstruction of Graphene by Methane Gas

Exposure

In this section, we report the reconstruction of broken graphene by high temperature treatment in methane gas. Graphene was fractured using electrical stress. Graphene reconstruction was confirmed by electrical measurements, SEM, AFM and Raman spectroscopy.

5.1.1 Fabrication of Graphene Devices

RCA cleaned n-type Si wafers (orientation (100), resistivity < 0.005 ohm cm) were oxidized by dry thermal oxidation process to obtain 100 nm SiO₂. Graphene flakes were exfoliated on SiO₂/Si by mechanical exfoliation method using HOPG. The SiO₂ surface was cleaned using argon plasma (RF, 50 W, 5 min.) before exfoliation of graphene for good adhesion.

Graphene flakes on SiO₂ surface were identified using an optical microscope (Olympus Corporation, MX61). The electrodes on graphene flakes were patterned by electron beam lithography (EBL, Raith 150^{Two}) using PMMA resist. The metal contacts (Ti/Pt - 10/40 nm) were deposited on the wafer by DC sputtering at a pressure of 5×10^{-7} mTorr, and at a power of 150 W for Ti and 100 W for Pt. The PMMA resist was removed during a lift-off process.

After deposition of metal contacts to make two-terminal devices, current - voltage (I-V) measurement of devices were performed using a semiconductor device analyzer (Agilent B1500). Voltage across the device was increased until the graphene breaks down due to resistive heating. After breakdown, the devices were split into two groups A and B, and processed and characterized as depicted in Fig. 5.2. Group A devices were exposed to methane gas (100 sccm) in a tube furnace at 850°C for 15, 30, 45 and 60 min. I-V measurements were performed again using the semiconductor device analyzer. Group B devices were characterized using a SEM (Raith 150^{Two} at an accelerating voltage of 5 kV), an AFM (Asylum/Oxford Instruments MFP3D Origin) and a micro Raman spectrometer (Horiba Jobin Yvon HR800-UV, 532 nm Ar-ion laser, 1 μ m laser spot size and 5 mW power). These devices were subsequently exposed to methane gas (100 sccm) in a tube

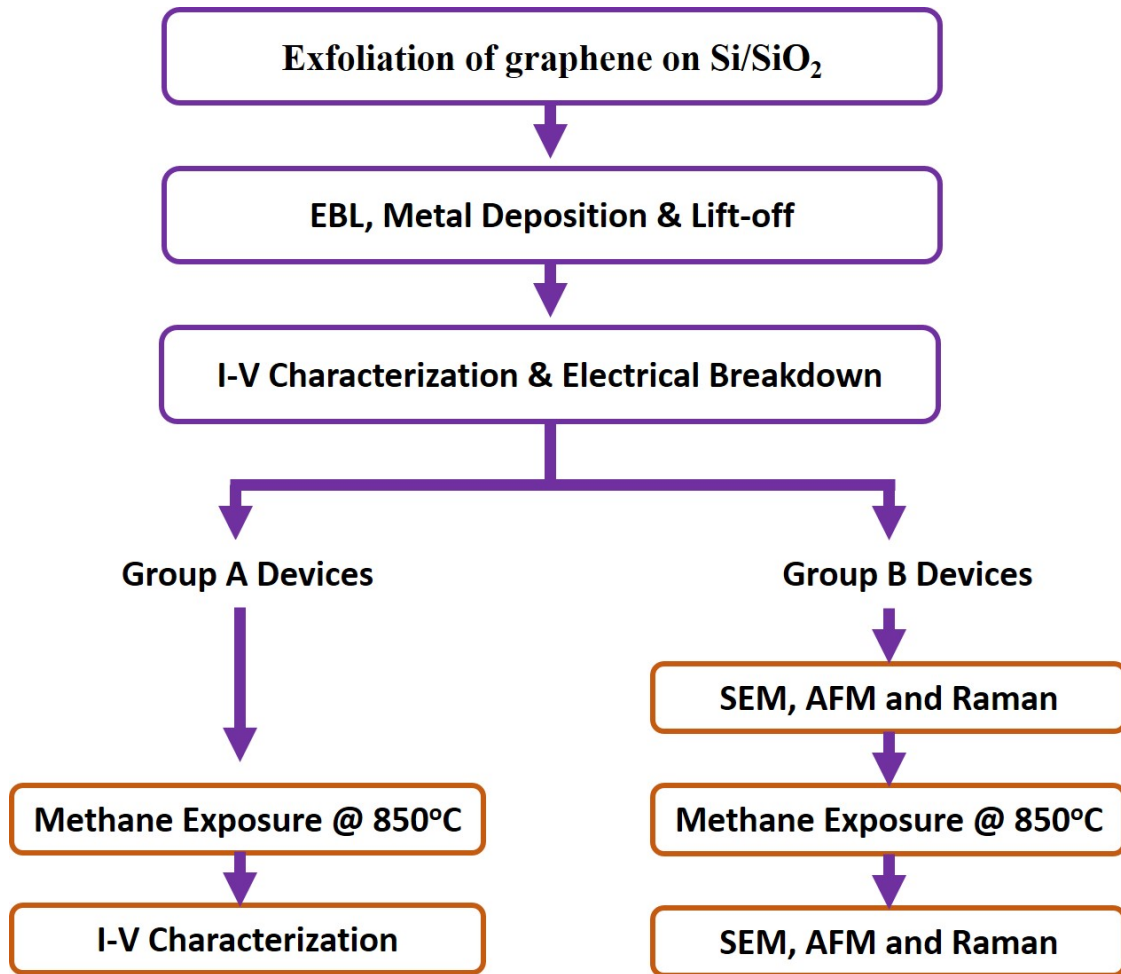


Fig. 5.2. Process sequences used for fabrication and characterization of two groups of devices.

furnace at 850°C for 15, 30, 45 and 60 min. The devices were again characterized using SEM, AFM and Raman spectrometer.

5.1.2 Results

Fig. 5.3(a) shows the I-V characteristics of one of the group B devices. This particular device breaks down at a voltage of 6.65 V. The breakdown voltage of graphene is in the range of 4 to 7 V in our devices. Inset of Fig. 5.3(a) shows the SEM images of the device before and after breakdown.

Fig. 5.3(b) shows the AFM image of a device after breakdown. The breakdown result in cracking of the graphene perpendicular to the flow of current in the device. The breakdown is due to resistive heating. Graphene channels have width in the range of 20

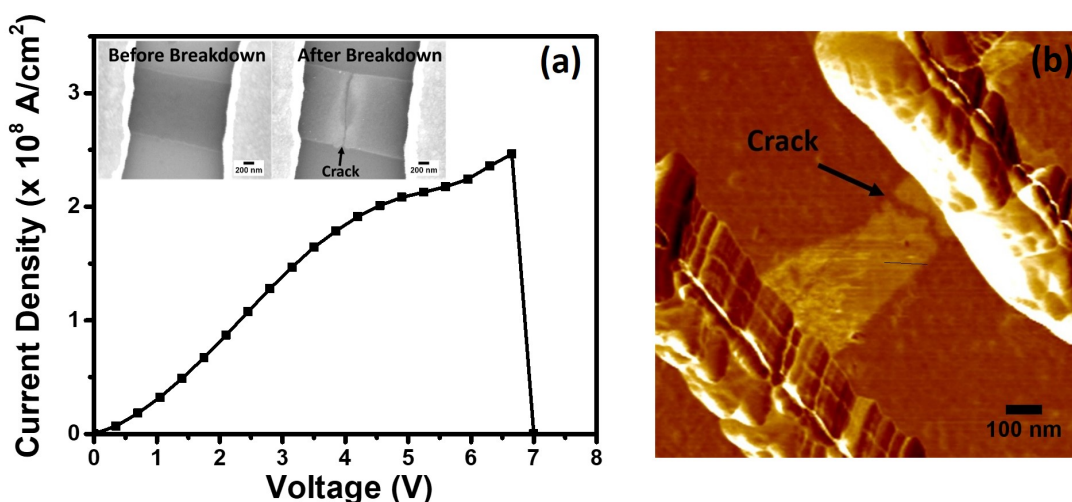


Fig. 5.3. (a) Measured I-V characteristics of a graphene device showing electrical breakdown. Insets show SEM images of the graphene before and after electrical breakdown. (b) AFM image of a device after breakdown.

nm - $1\ \mu\text{m}$ and length in the range of $300\ \text{nm}$ - $1\ \mu\text{m}$. The breakdown current density of the device shown in Fig. 5.3(a) is $2.5 \times 10^8\ \text{A}/\text{cm}^2$, which is higher than the value reported for CVD graphene ($4 \times 10^7\ \text{A}/\text{cm}^2$) [90]. CVD graphene has higher defect and impurity density than mechanically exfoliated graphene obtained from HOPG.

Fig. 5.4(a) shows the I-V characteristics before breakdown, after breakdown and after 15 min. of methane gas exposure of a device in group A, and Fig. 5.4(b) shows the same for another device of group A after 30 min. of methane gas treatment. The current is seen to be restored after 30 min. of methane treatment, suggesting that the thermal treatment has reestablished the electrical connection between the two segments of the broken graphene. The current after the treatment is seen to be higher than the pre-breakdown value. However the current was not restored completely for the 15 min. treatment suggesting insufficient reconstruction. Thermal treatment of 45 and 60 min. are more than sufficient to dissociate carbon from methane and react with cracked graphene edges. The current-voltage characteristics of 45 and 60 min. of methane gas treatment are shown in Fig. 5.4(c, d). The electrical characteristic of repaired graphene in Fig. 5.4(c) and (d) are also showing that graphene was not only fully restored but also it increases the current value more than pre-breakdown value. The current was in the range of picoamperes, the noise floor of the measurement system, after breakdown of all devices, as shown in Fig.

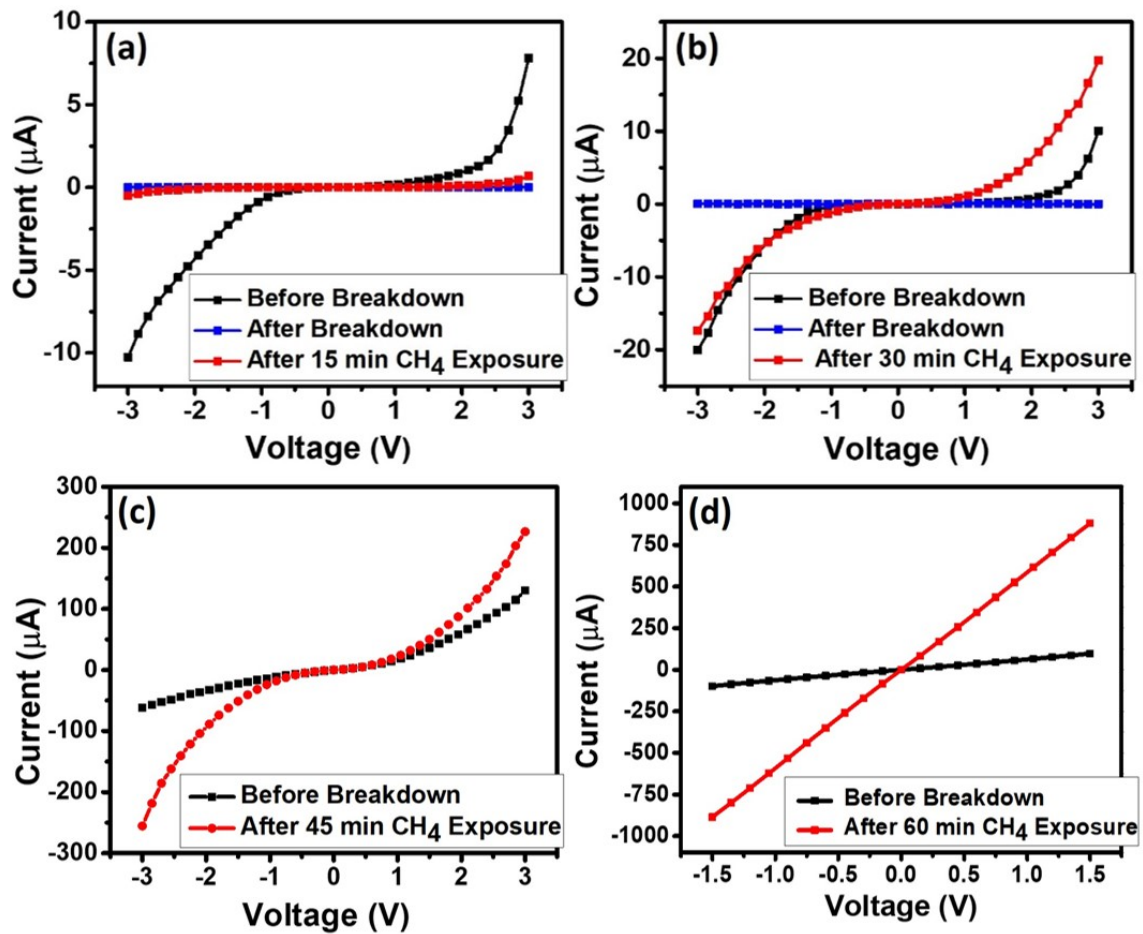


Fig. 5.4. (a) I-V characteristics of group A devices before breakdown, after breakdown and after 15 min. of thermal treatment in methane. Current is not fully restored after 15 min. of methane exposure. (b) Current-voltage characteristics after 30 min. of thermal treatment in methane. (c) Current-voltage characteristics before breakdown and after 45 min. of thermal treatment in methane gas. (d) Comparison of current values before and after 60 min. of methane treatment.

5.5(a). Fig. 5.5(b) shows the ratio of the current after reconstruction to the current before breakdown, both currents measured at 3 V, as a function of methane exposure time. The methane gas exposure times of 45 and 60 min. are more than sufficient to restore the current conduction through the graphene.

Fig. 5.6(a) shows the SEM of a group B device after breakdown. A crack is clearly visible in the graphene. Fig. 5.6(b) shows the SEM of a group B device after methane exposure.

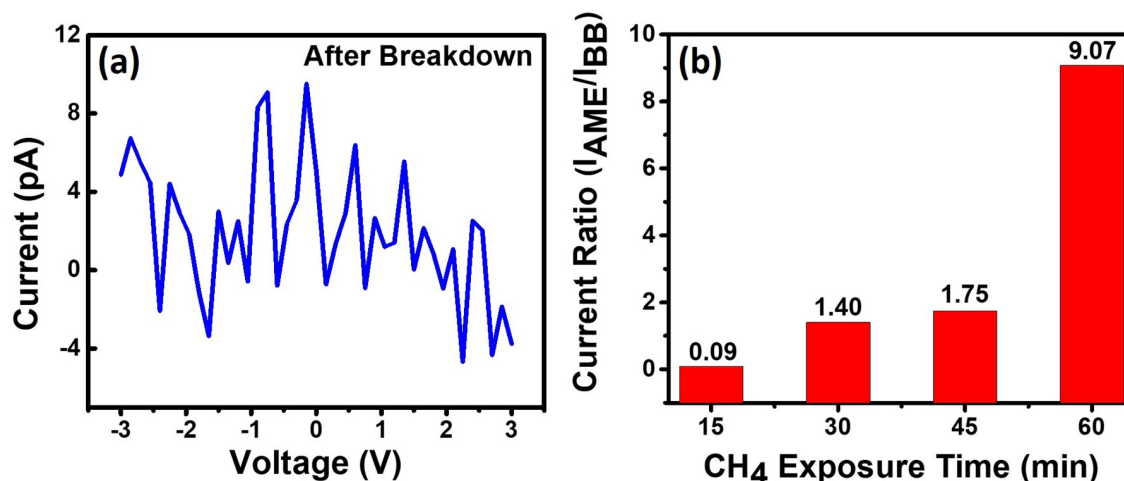


Fig. 5.5. (a) I-V characteristics of a device after breakdown. The current is in the range of picoamperes, the noise floor of the measurement system, after breakdown. (b) Ratio of current after methane gas exposure to the current before breakdown (both the currents measured at 3 V) as a function of methane exposure time. I_{BB} - Before Breakdown current, I_{AME} - After Methane Exposure current.

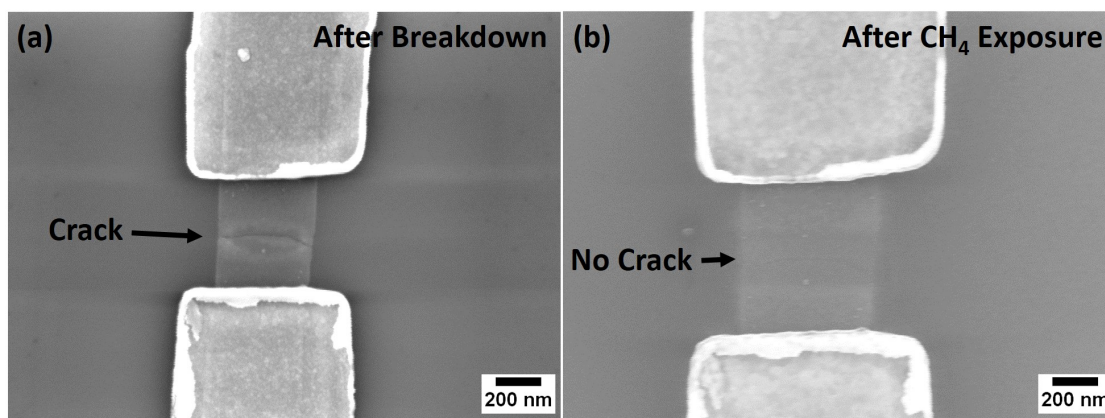


Fig. 5.6. (a) SEM of graphene showing crack after breakdown and (b) SEM image of reconstructed graphene. Crack is healed after CH₄ exposure.

The crack is seen to be repaired after methane exposure. Based on the analysis of several AFM and SEM images, most of the cracks have width in the range of 5 - 50 nm. A small crack is shown in Fig. 5.7(a), which is healed after methane exposure (Fig. 5.7 (b)). But few graphene samples show large width of fracture after breakdown as shown in Fig. 5.7(c). The width of the crack in this case is approximately 120 nm. Such large cracks are also seen to be reconstructed after methane exposure as shown in Fig. 5.7(d).

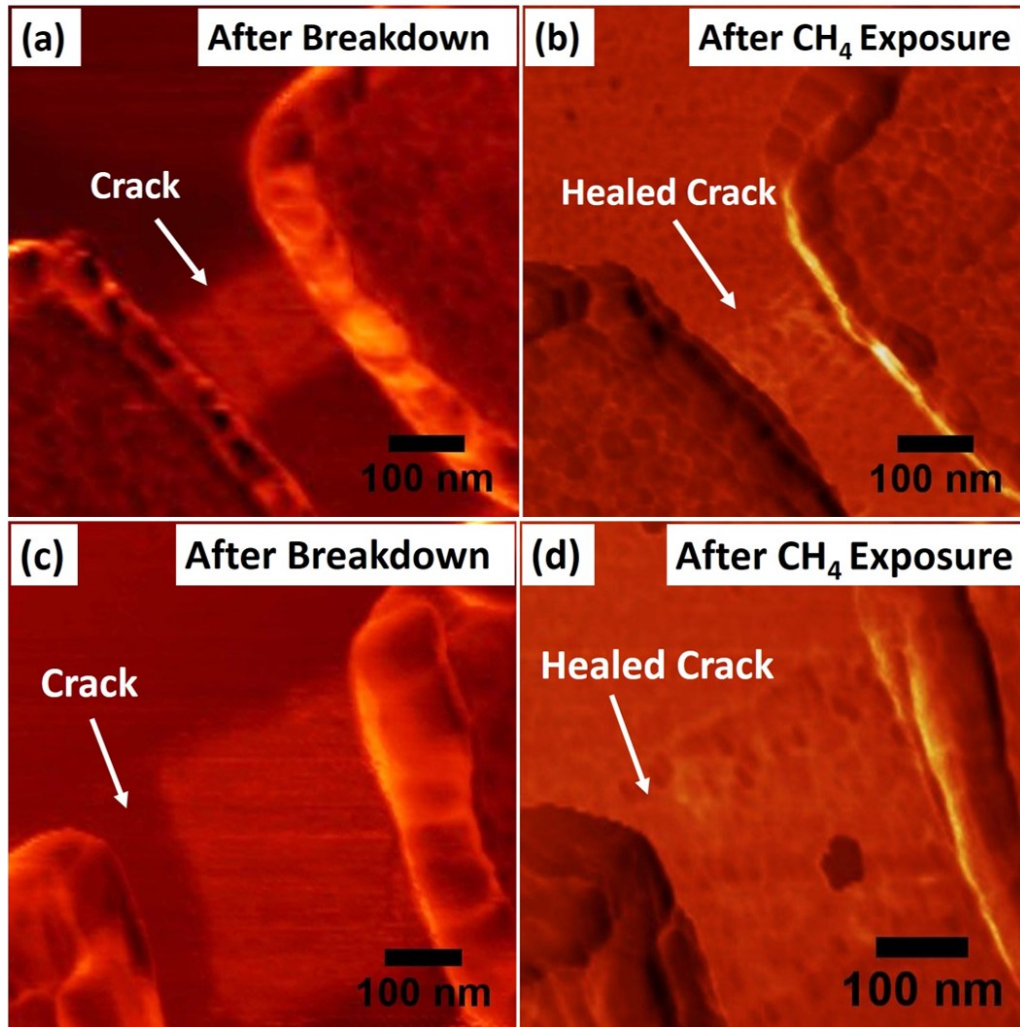


Fig. 5.7. (a) AFM image of graphene with small crack width of ~ 10 nm. (b) AFM image after healing of small crack. (c) AFM image of graphene with a large crack (~ 120 nm) after breakdown. (d) AFM image after reconstruction of large crack in (c).

For detailed study of electrical properties of reconstructed graphene, maximum current density and resistivity were also extracted from the I-V characteristics. These parameters allow a fair quantitative comparison of the characteristics of several devices of varying length and width. In our experiment, the maximum current density was obtained by dividing the current measured at 3 V by the cross sectional area of the device. The cross sectional area is given by the product of the width and height of the graphene. Suzuki et al. proposed a power law relationship for the maximum current density with resistivity ($J_{MAX} \propto 1/\sqrt{\rho}$) [129]. The maximum current density decreases with the length as shown in Fig. 5.8(a). The same characteristic was also followed by graphene after methane exposure. Fig. 5.8 exhibit correlation between resistivity and maximum current density.

The data is fitted with $J_{MAX} = A\rho^{-n}$ with $A = 1.07 \times 10^7 \text{ A/cm}^2$ and $n = 0.89$. The R^2 value of the fit is 0.78, indicating a good fit of the data to the model. Murali et al. argued that a value higher than 0.5 for n indicates higher density of defects in the GNR if the breakdown mechanism is Joule heating [35]. Higher resistivity of graphene induce faster breakdown and this higher resistivity might occur due to higher defect density. Here in Fig. 5.8(b), resistivity after thermal treatment in CH_4 is lower than the before breakdown resistivity. Fig. 5.8(b) suggests that the thermal treatment in CH_4 does not alter the defect density significantly.

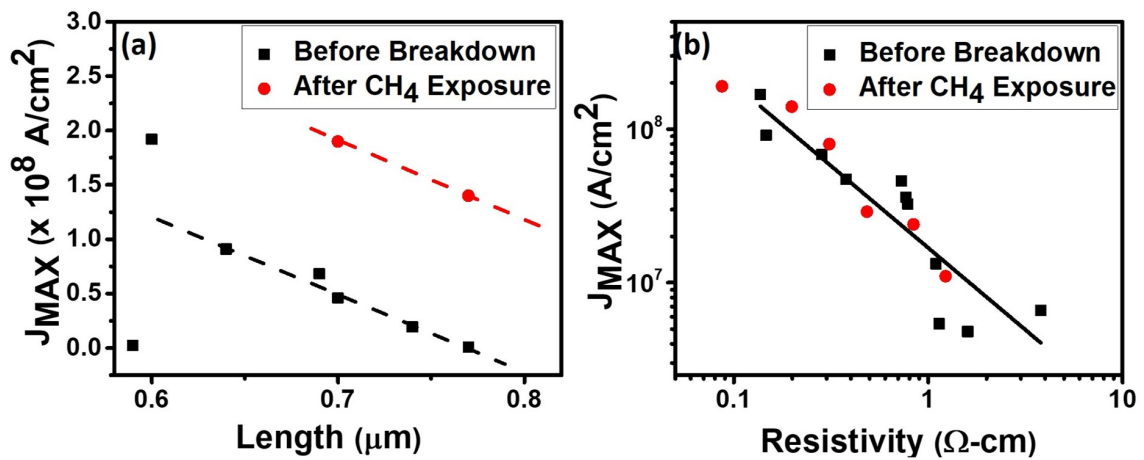


Fig. 5.8. The maximum current density (J_{MAX}) of graphene as a function of (a) length and (b) resistivity (ρ). Maximum current density decreases with the resistivity and length. The lines are fits to experimental data.

Raman measurements were performed on graphene to verify number of layers before breakdown and after methane exposure. Raman spectrum before breakdown and after methane exposure for 30 min. are shown in Fig. 5.9. Fig. 5.9(a) shows red shift of G and 2D peaks, and decrease in the ratio of I_{2D}/I_G after CH_4 exposure, which indicates doping [108]. Fig. 5.9(b) and (c) show the deconvolution of the 2D peaks before breakdown and after CH_4 exposure respectively. After reconstruction of graphene, number of layers is seen to be increased to three [140]. Fig. 5.9(d) shows the Raman spectra acquired from the surface of SiO_2 far from the device regions, before breakdown and after CH_4 exposure. No signature of carbon deposition on SiO_2 during the CH_4 exposure could be identified from the Raman spectra.

Fractured graphene can also be reconstructed without the presence of metal on the sample surface due to activation of dangling bonds and high energy states of graphene

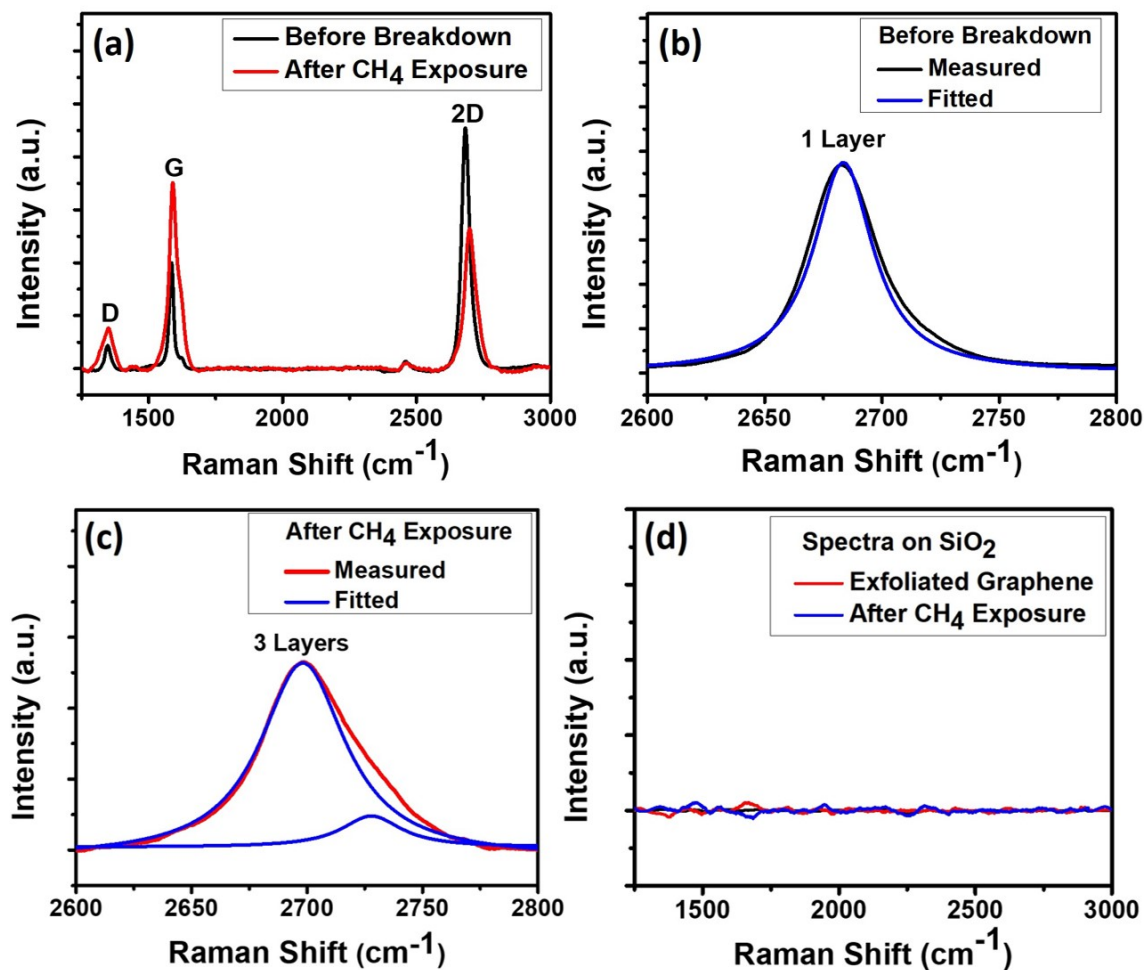


Fig. 5.9. (a) Raman spectra before and after CH₄ exposure for 30 min. G and 2D peaks are red shifted after CH₄ exposure, suggesting doping. (b) Deconvolution of the 2D peak obtained before breakdown. (c) Deconvolution of the 2D obtained after CH₄ exposure. (d) Raman spectra obtained on SiO₂ far from device areas before breakdown and after CH₄ exposure.

edges after fracture. We performed thermal treatment of methane gas on graphene without metal on the samples to investigate if catalytic action by the metal is necessary for the reconstruction. Graphene was fractured by the tip of the atomic force microscope, and nanoindentation (Nanoindenter, Hysitron Inc, TI-900). In AFM, 800 nN force was applied on graphene by Si tip (spring constant 40 N/m) at consecutive points. An example of consecutive points of force by AFM tip is shown in Fig. 5.10.

Fracture is seen in graphene after applying force (Fig. 5.11(a)). A large fracture is visible, as highlighted in the inset of Fig. 5.11(a), and the graphene is seen to be folded at the edges. After the fracture the graphene was subjected to thermal treatment in methane

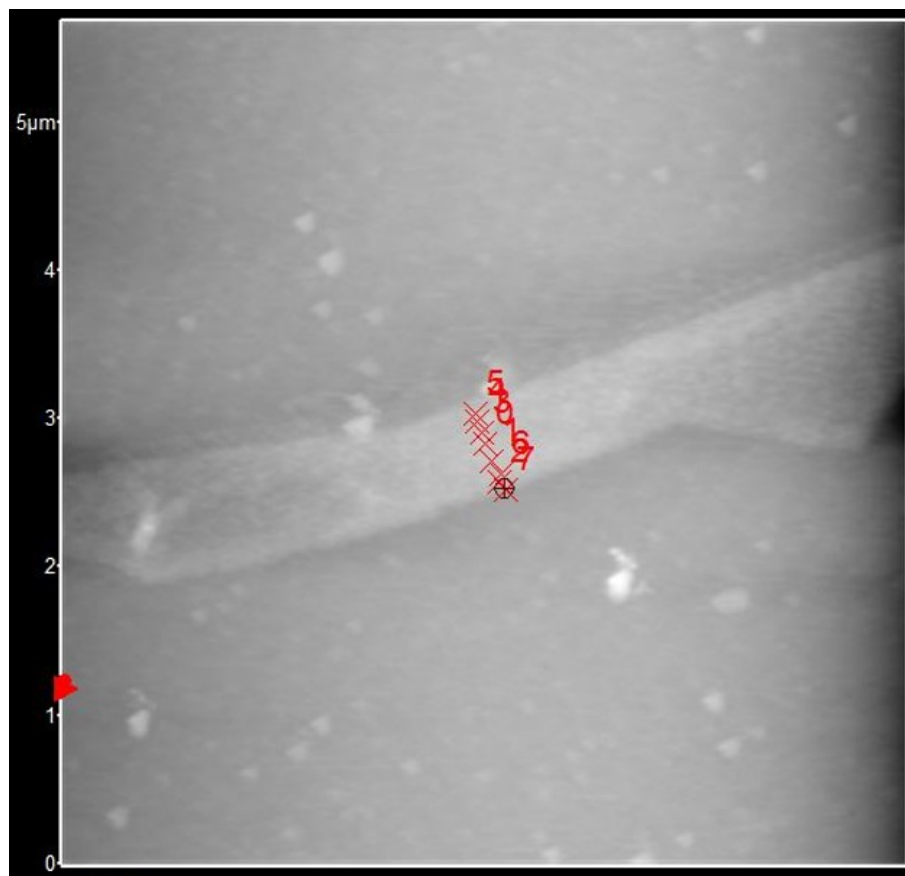


Fig. 5.10. Atomic Force Microscopy (AFM) image of exfoliated graphene with consecutive force points. The AFM tip force was 800 nN.

gas at 850°C. The fracture was healed after methane exposure which is clearly visible in Fig. 5.11(b).

In nanoindentation, Berkovich tip with 1 mN force was used for indenting a graphite flake. AFM image of indented graphite flake is shown in Fig. 5.12(a). The line profile of blue arrow of Fig. 5.12(a) shows that depth of indent is 6 nm (Fig. 5.12(b)). Indent width is approximately 300 nm. After indentation, the sample is treated at 850°C in methane gas. Fig. 5.12(c) shows the reconstruction of fractured graphite flake. The line profile of reconstructed graphite flake at indent spot in Fig. 5.12(d) shows that the indent is partly reconstructed by the thermal process. The indent depth has decreased from 6 nm to 3 nm after the thermal treatment in methane. We conclude that fractured graphite flake can be reconstructed by thermal treatment in methane ambient and this process do not require any catalyst.

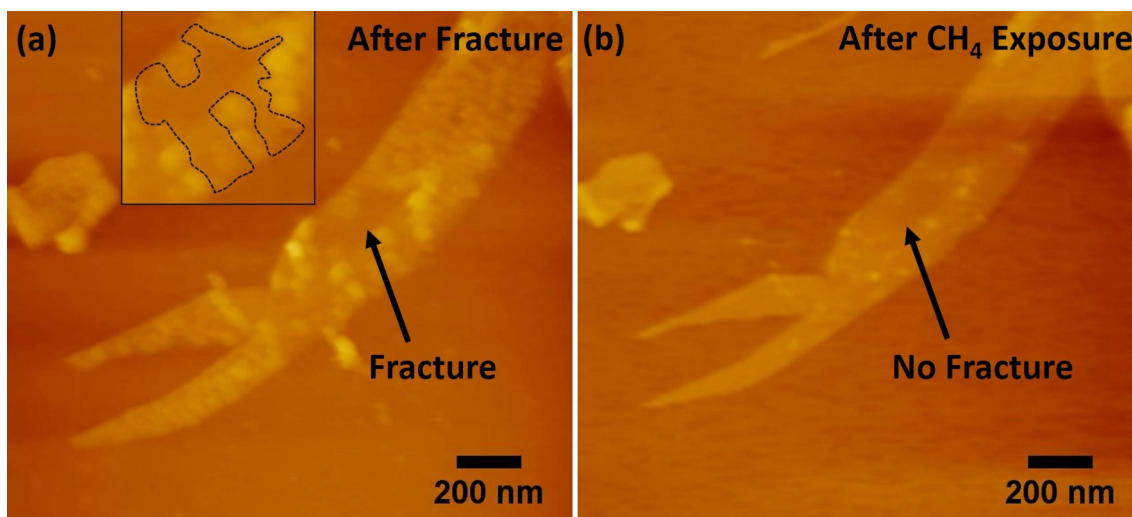


Fig. 5.11. (a) AFM image of exfoliated graphene after force microscopy with 800 nN force. Black arrow shows the fracture. The magnified view of fracture is shown in the inset of figure (a). (b) AFM image of exfoliated graphene after thermal treatment with methane gas. Fracture is healed after thermal treatment.

5.1.3 Discussion

Previous studies on graphene and CNTs, reported that the edges of graphene sheets and CNTs have activated dangling bonds, zigzag and armchair edges [80, 177]. These edges have high chemical activity because of their distinct electronic states near the Fermi level [92, 178, 179]. In our process, during electrical breakdown the carbon - carbon bonds in graphene are broken leading to creation of dangling bonds and zigzag/armchair edges at the breakdown sites. Our experiments show that the broken graphene can be reconstructed by high temperature treatment in methane gas. At the high temperature employed, methane decomposes. The C - C bond in graphene has higher dissociation energy (4.95 eV) than C - H bond (4.51 eV) in CH_4 [180], implying that at the temperature used in our process, methane could be dissociated while the graphene remains stable. Carbon from the dissociated methane diffuse to the substrate and could repair the breaks in the graphene layer. This process is somewhat similar to the initial steps in the CVD growth of graphene [181]. At high temperature, carbon from methane precursor react with the edge carbons and make covalent bonds with the activated edges. Formation of covalent bonds induce healing of fractured graphene. This process is visualized in Fig. 5.13.

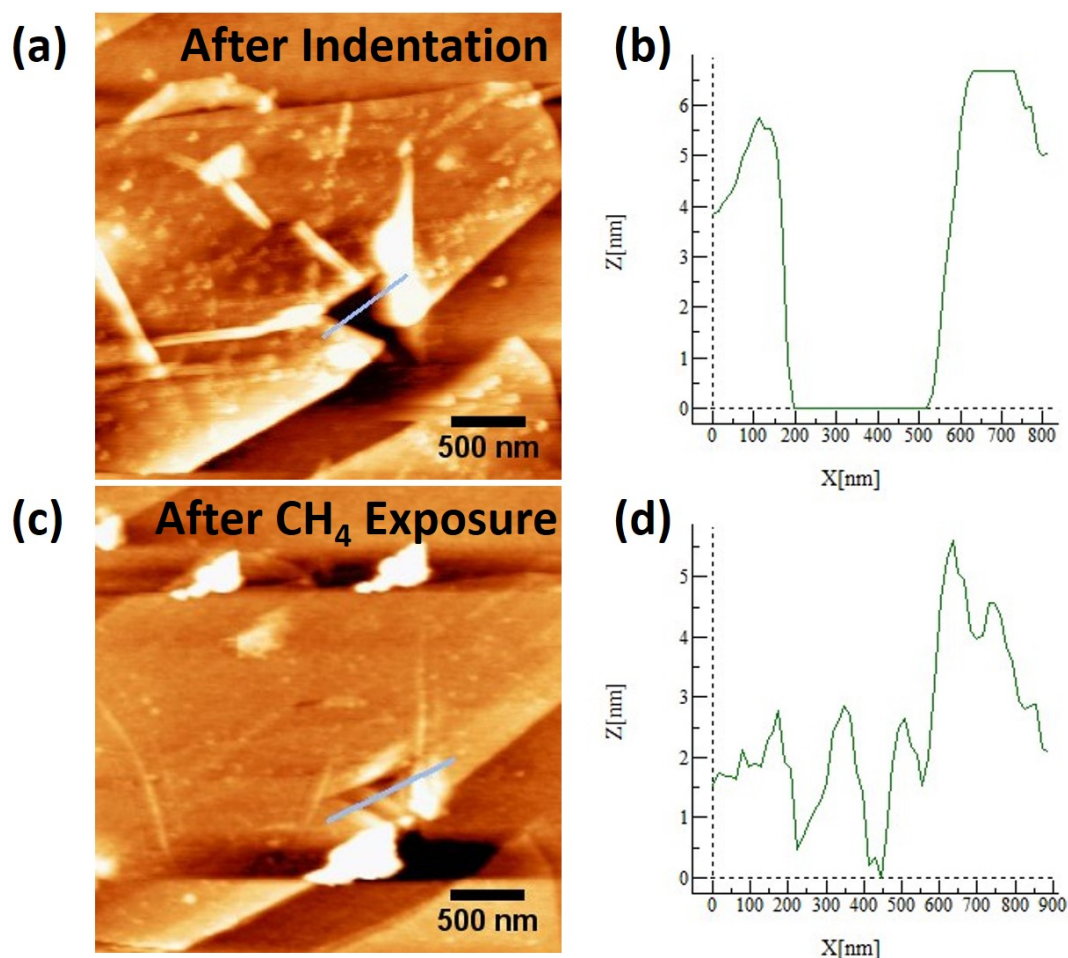


Fig. 5.12. (a) AFM image of exfoliated graphite flake after nanoindentation with 1 mN force. (b) Height profile along the blue line in figure(a). Depth and width of nanoindent are approximately 6 nm and 300 nm. (c) AFM image of exfoliated graphene after thermal treatment in methane gas. (d) Height profile of blue line in figure(c). The depth of the indent has decreased from 6 nm to 3 nm at many locations within the 300 nm indicating reconstruction.

5.2 Reconstruction of Graphene by E-Beam Irradiation

Electron-beam irradiation effects on graphene have been already demonstrated [107]. The beam energy used in [107] was 5-10 keV. Here we illustrate the healing of fractured graphene by low energy e-beam irradiation.

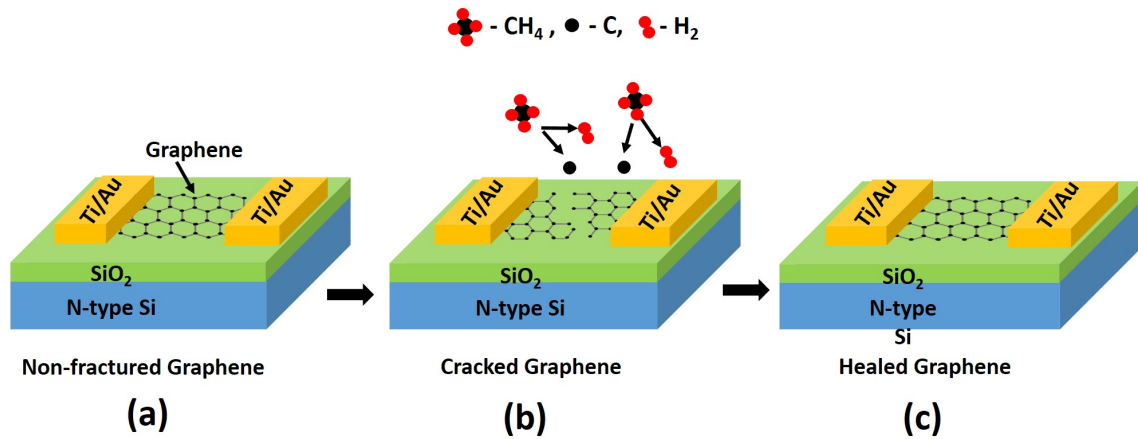


Fig. 5.13. Schematic of graphene healing process. (a) Intact graphene device with contact pads. (b) Fractured graphene after electrical breakdown. (c) Healed graphene after CH_4 exposure.

5.2.1 Experimental

For reconstruction of fractured graphene by e-beam irradiation, two groups of devices were fabricated as shown in Fig. 5.14. After device fabrication, current-voltage measurement was performed using a semiconductor device analyzer (Agilent B1500). High bias during measurement induce fracture in graphene and gives current in picoampere. After breakdown of devices, SEM and Raman characterization were carried out. After physical characterization, devices were splits in to two group C and D. Group C devices were irradiated with e-beam (10 keV, 5 min.) in Raith 150 Two System. Group D devices were firstly irradiated with e-beam for 2 min. at 10 keV and subsequently treated with CH_4 gas at 850°C for 15 and 60 min.

After e-beam irradiation and methane gas exposure, all electrical and physical characterizations (I-V, SEM and Raman) were performed again on group C and D devices. In methane gas treatment, 100 sccm methane gas flow and cooling gas argon were used. SEM and Raman spectroscopy confirms healing of cracked graphene nanoribbons.

5.2.2 Results

In e-beam irradiation method, devices of group C were irradiated with low energy electron (10 keV) in SEM for 5 min. after electrical stress. Fig. 5.15(a) confirms increment of current after e-beam irradiation. The breakdown current after electrical stress

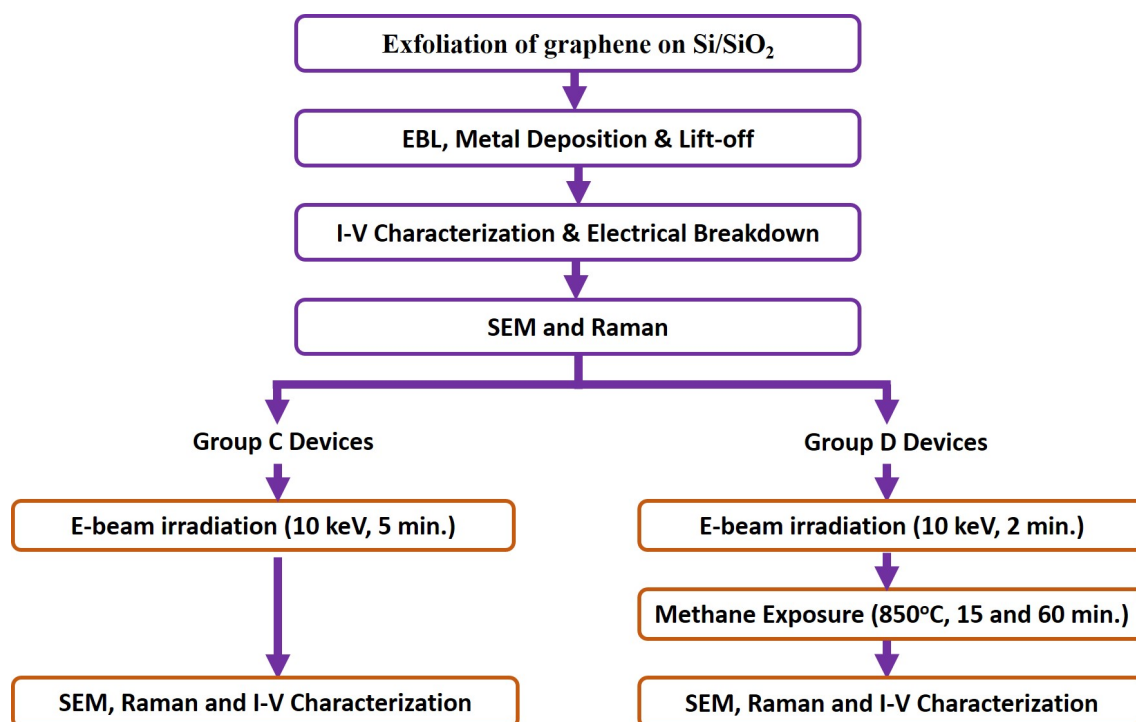


Fig. 5.14. Process sequences used for fabrication and characterization of two groups of devices for reconstruction of graphene by e-beam irradiation and e-beam irradiation with methane exposure.

is in picoampere (Fig. 5.15(b)). The current is improved because of mechanical joining of broken graphene edges which occurs due to Joule heating which rearrange the carbon network or reconstruct the graphene. Cracked graphene nanoribbon after breakdown and healed graphene nanoribbon after e-beam irradiation is shown by SEM images in Fig. 5.16(a) and (b).

For healing of graphene nanoribbon, e-beam was irradiated for 5 min but for healing of larger width of graphene, longer e-beam exposure is required. Longer e-beam irradiation can damage the graphene thus shorter e-beam irradiation with methane gas treatment was explored. In e-beam irradiation with methane treatment, current values of group D devices were restored after e-beam irradiation with methane gas exposure. Comparison of electrical characteristics before breakdown and after e-beam irradiation with 15 min. of methane treatment are shown in Fig. 5.17(a). Same process (e-beam irradiation with methane gas) is repeated but methane gas exposure time was increased from 15 min. to 60 min. Current values after e-beam irradiation with methane treatment is increased (Fig.

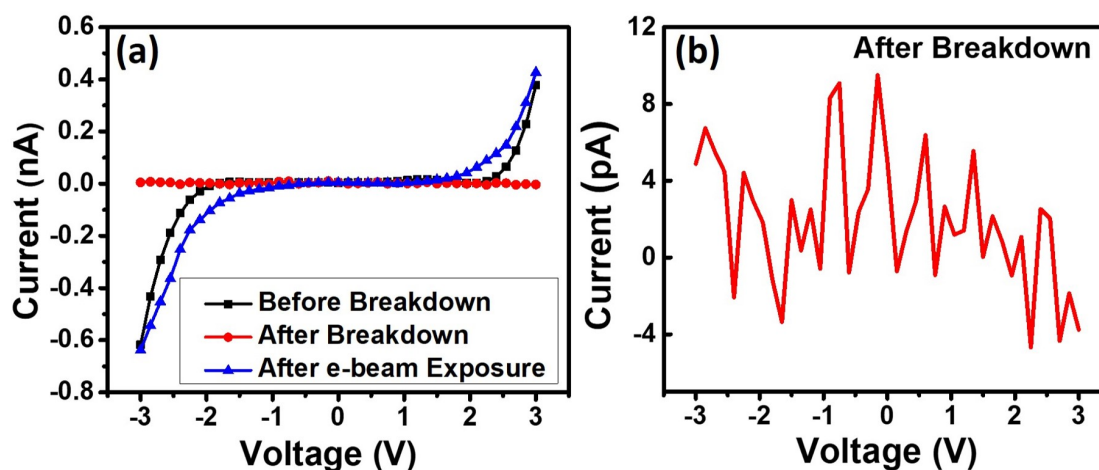


Fig. 5.15. (a) Current-voltage characteristic of graphene before breakdown, after breakdown and after e-beam exposure. (b) Fractured graphene is showing picoampere currents after breakdown.

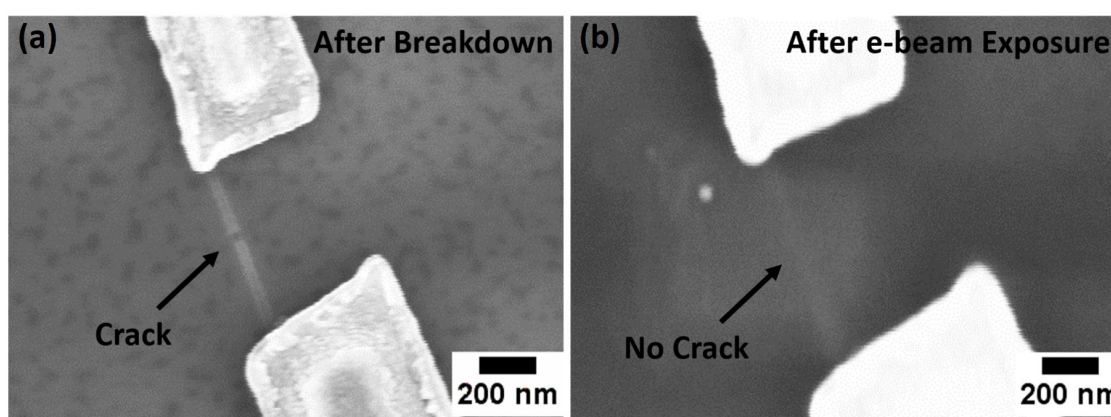


Fig. 5.16. (a) SEM image of graphene nanoribbons after breakdown and (b) after e-beam irradiation. After breakdown it is showing crack and after irradiation crack is not clearly visible.

5.17(a) and (b)). This indicates that longer methane exposure induce more graphene layer formation by decomposition of carbon from methane source.

The crack and healing of graphene after breakdown, and after e-beam irradiation and CH_4 treatment are shown in Fig. 5.18. The cracks are repaired after exposure which is clearly visible in Fig. 5.18(b). Physical confirmation of intact graphene, fractured graphene and healed graphene after reconstruction are shown in Fig. 5.19.

The current ratio after e-beam irradiation and e-beam irradiation with methane exposure to before breakdown as a function of exposure time are also compared in Fig.

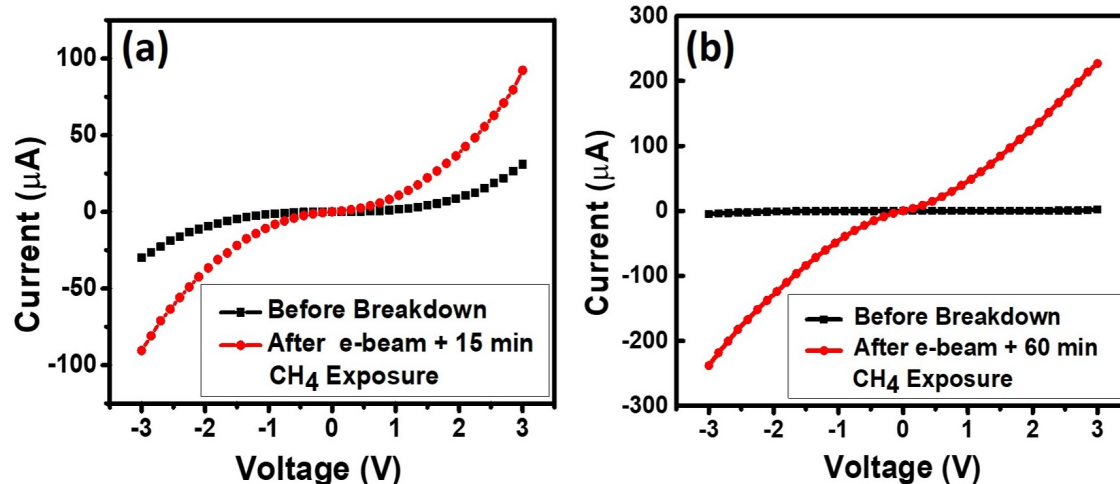


Fig. 5.17. Current-voltage characteristics (a) Before breakdown and after 2 min. e-beam irradiation and 15 min. of methane exposure. (b) Before Breakdown and after 2 min. e-beam irradiation and 60 min. of methane exposure.

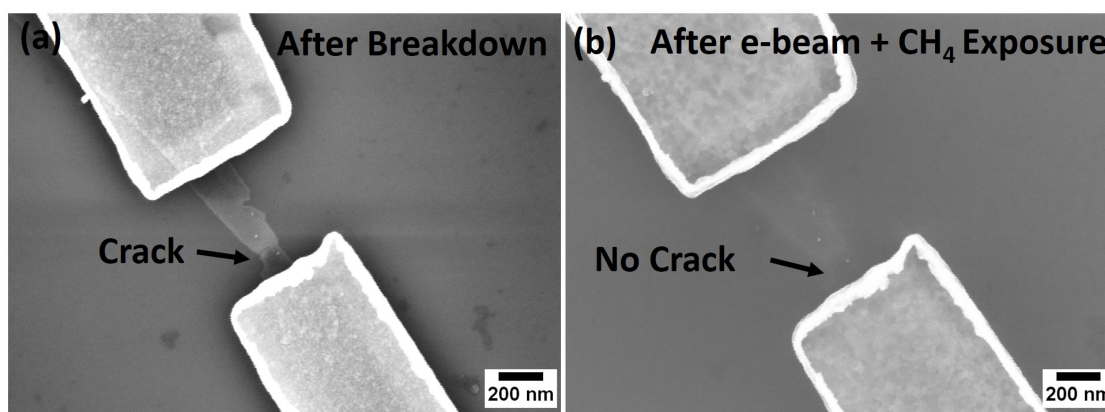


Fig. 5.18. (a) SEM of graphene crack after breakdown and (b) Healed graphene after e-beam with CH₄ exposure.

5.20(a). It is seen that longer methane exposure increase the current values. The current values were measured at 3 V. We also plotted current density as a function of resistivity in Fig. 5.20(b). Pre-breakdown, and after e-beam irradiation and methane gas exposure follow the power law relation between current density and resistivity [129]. In power law relation, current density is inversely proportional to the resistivity (equation is already expressed in section 5.1.2). Reconstructed graphene after e-beam irradiation and e-beam with methane exposure have similar electrical characteristics as intact graphene.

Raman spectrum of fractured graphene before breakdown and after e-beam irradiation are shown in Fig. 5.21(a) and deconvolution of 2D peak in Fig. 5.21(b) and (c) con-

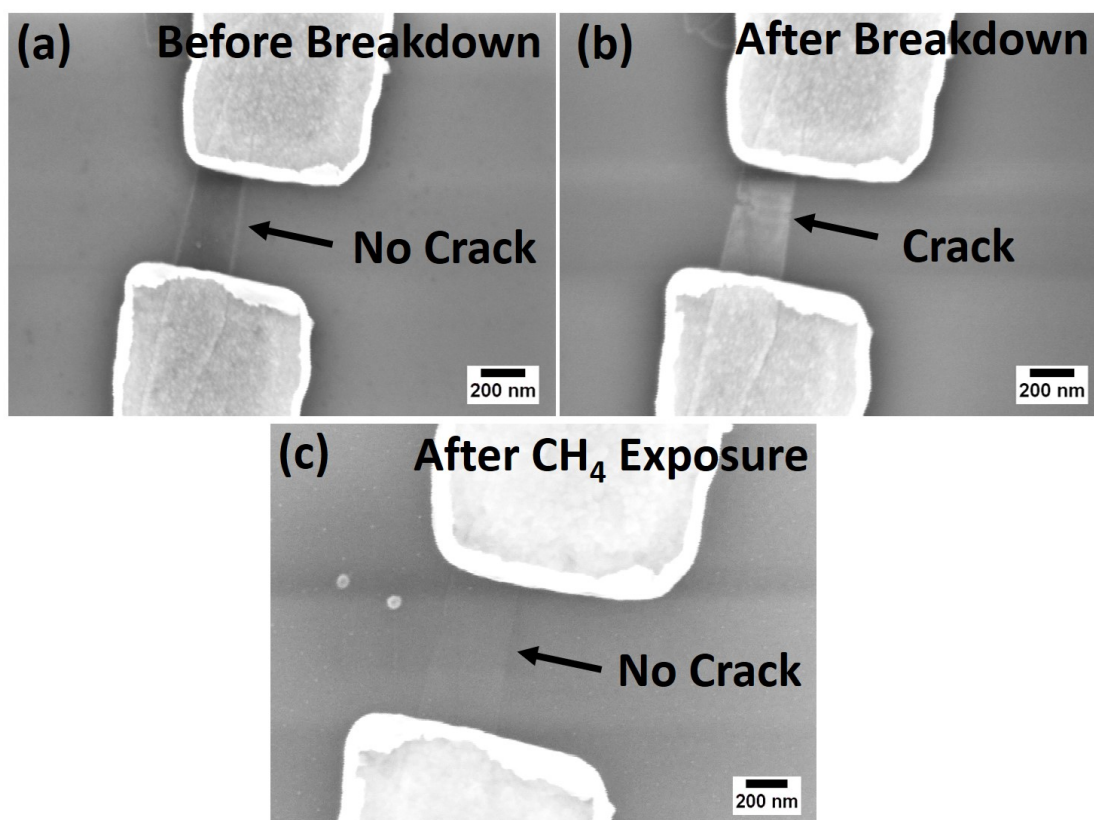


Fig. 5.19. (a) SEM of intact graphene before breakdown (no crack) and (b) Crack is shown after electrical stress. (c) Crack is invisible after CH₄ gas treatment.

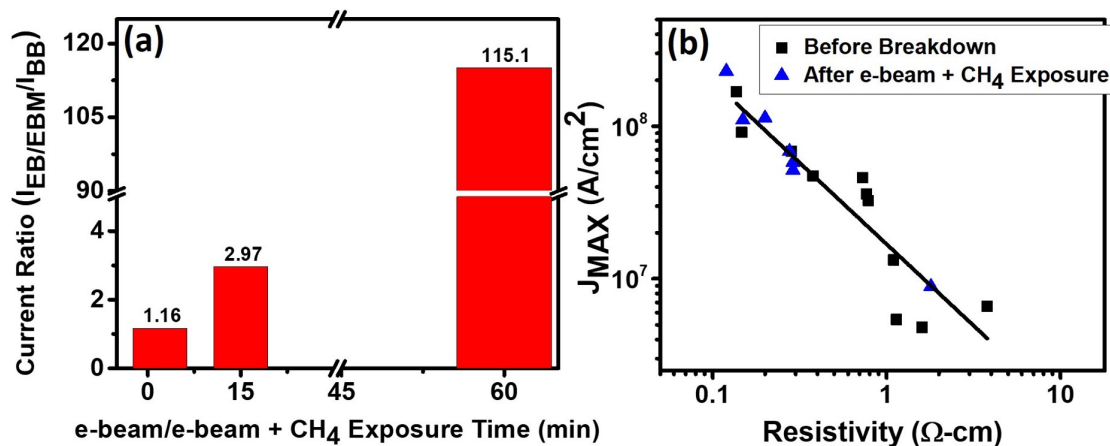


Fig. 5.20. (a) Ratio of current after e-beam with methane gas exposure to the current before breakdown (both the currents measured at 3 V) as a function of methane exposure time. (b) Maximum current density as a function of resistivity.

firm that number of graphene layers (6-7 layers) are same. This indicates that graphene is healed only in cracked region and there is no increment in number of layers. Fig. 5.21(d)

shows that e-beam with methane treatment increase number of layers from 3 to 4-5 layers. The number of layers is extracted by Lorentzian fitting of 2D peak. Raman spectrum before breakdown and after e-beam irradiation and, after e-beam irradiation with methane exposure in Fig. 5.21(a) and (d) show red shift of G and 2D peak and decrease in the ratio of 2D/G peak which indicates heavy doping [108] and more number of graphene layers. Another reason of heavy doping could be that vacuum annealing removes H₂O and O₂ molecules from the substrate.

5.2.3 Discussion

After physical breakdown of graphene, graphene breakage is healed by e-beam irradiation. In e-beam irradiation method, amorphous carbon is deposited at broken graphene edges by applying low energy e-beam (10 keV) due to knock-on effects [91]. The source of amorphous carbon in this case is the hydrocarbon contamination in SEM tool. During beam focusing and irradiation at broken sites of graphene, these amorphous carbon react with activated carbon edges at broken sites.

The graphene edges have higher chemical reactivity due to delocalization of charge distribution at the step edges according to first principle calculations [182–184]. These states react with amorphous carbon and join the broken carbon networks. For joining of carbon networks, several electron volts of activation energy is required which is provided by the electron beam [51]. After electron beam focusing at fractured region, the dangling bonds are activated at the edges due to current heating and form new covalent bonds and rearrange the carbon networks for joining of fractured graphene layer. Electron beam energy is a critical parameter for joining of graphene layers. At very low energy (<1.6 keV), dangling bonds at the edges are not activated for joining of graphene layers and high energy (100-200 keV) evaporates carbon easily and damage the graphene [48, 185]. Thus appropriate applied electron beam energy (5-10 keV) is required for joining of broken graphene layers. Schematic illustration of healing process of cracked graphene by e-beam irradiation is illustrated in figure 5.22.

In e-beam irradiation with methane exposure method, in addition to the amorphous carbon deposited in SEM, carbon from methane gas also reacts at broken edges of graphene. At high temperature, amorphous carbons (from e-beam irradiation) are graphitized and react with carbon from methane gas source. The covalent bonds are formed

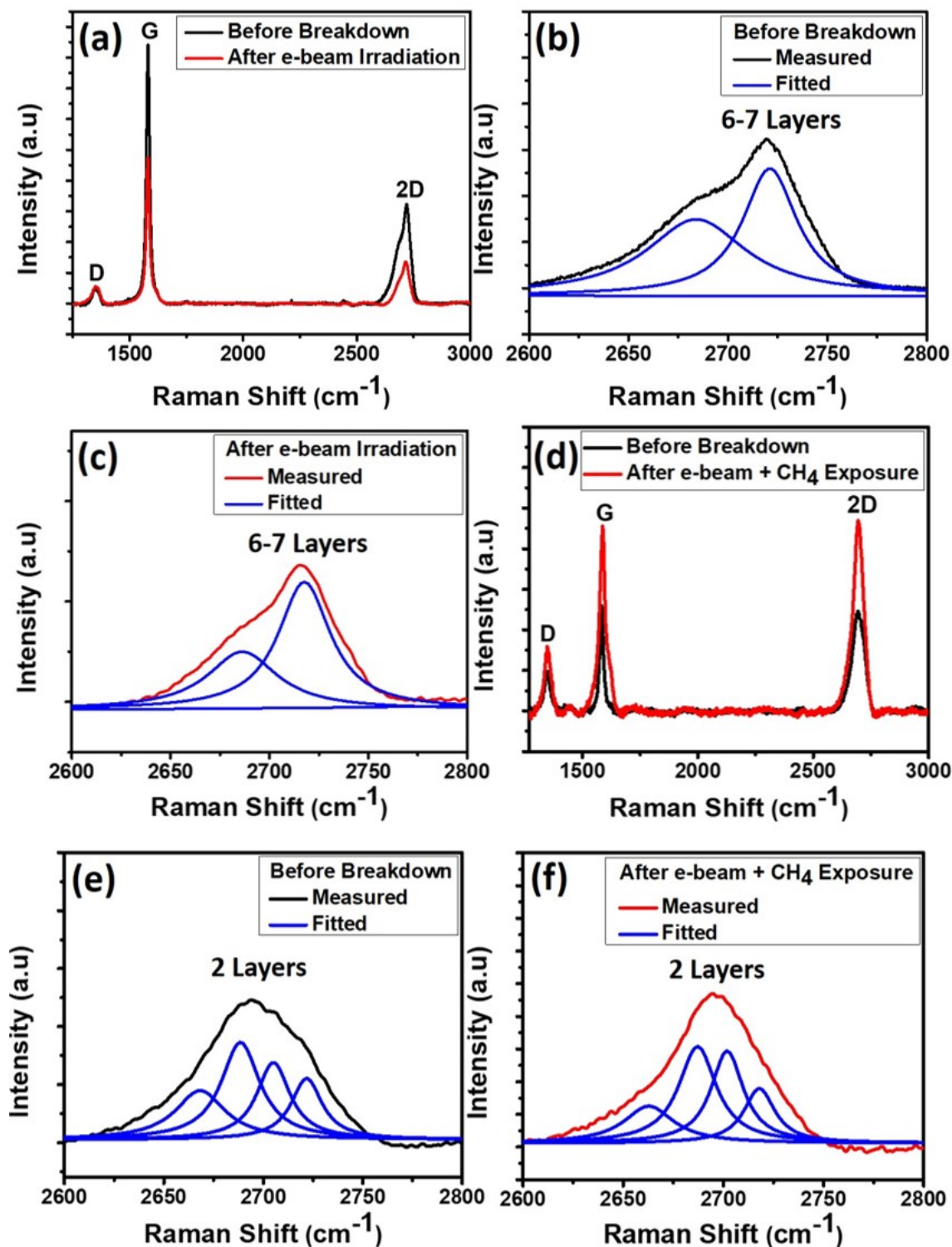


Fig. 5.21. (a) Raman spectrum of graphene before breakdown and after e-beam irradiation. (b,c) Lorentzian fitting of 2D peak before and after e-beam irradiation which confirms number of layers are same. (d) Raman Spectrum of graphene before breakdown and after e-beam irradiation with methane exposure. (e,f) Lorentzian fitting of 2D peak before and after e-beam irradiation with methane exposure which confirms the more number of graphene layer formation.

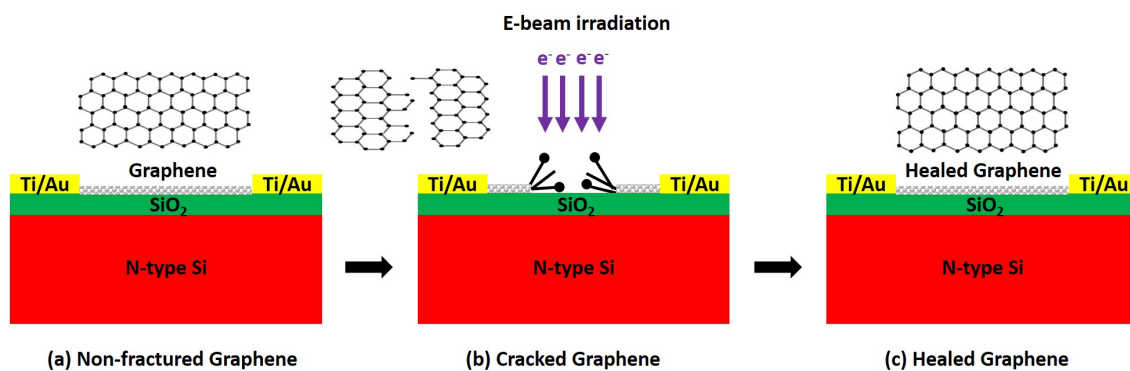


Fig. 5.22. Schematic of graphene healing process. (a) Graphene device with contact pads. (b) Fractured graphene after electrical breakdown and exposed with e-beam irradiation. (c) Healed graphene after e-beam irradiation.

between carbon from methane gas source and broken graphene edges. This covalent bond formation join the fractured graphene layer.

5.3 Summary

In this work we have demonstrated reconstruction of fractured graphene by a high temperature thermal treatment in methane gas, by e-beam irradiation and a sequence involving e-beam irradiation followed by methane gas exposure. Graphene was fractured by applying electrical stress. Electrical and physical characterization results are presented to prove the reconstruction. It is noticed that the reconstruction process induce doping in the graphene and the number of layers of graphene is increased after reconstruction. A suitable process window in terms of process temperature and time may be obtained by further optimization of the reconstruction process for controlling the number of layers of graphene after reconstruction. For e-beam irradiation, individual device has to be irradiated and it would be time-consuming and expensive process. The methane treatment reconstruction process has the potential to be employed for large scale repair of graphene after device processing.

Chapter 6

Conclusions and Future Scope

In this thesis, two topics on advanced processing of graphene were explored. These are namely (i) graphene nanoribbon fabrication by metal nanoparticle catalysed etching of graphene, presented in chapter 4 and (ii) reconstruction of fractured graphene, presented in chapter 5. The following conclusions can be drawn from the work presented in chapter 4.

- Pt-assisted etching is better than Ni-assisted etching due to higher carbon solubility and physisorption of Pt on graphene.
- The etching behavior is better in exfoliated graphene than CVD graphene due to low density of defects. Etching is randomly oriented in CVD graphene due to wrinkles and grain boundaries. In exfoliated graphene, etching proceeds along crystallographic orientations (30° , 60° , 90° , 120° and 150°).
- GNRs with width of sub - 10 nm and 10 - 20 nm were obtained in exfoliated graphene.
- The crystallographic orientations of etched graphene and width of GNRs are extracted from SEM and AFM techniques. The chirality of graphene nanoribbon edges (arm chair or zigzag) are identified by Raman spectroscopy and imaging.
- High quality of the GNR shows high I_{ON}/I_{OFF} ratio (2×10^7) and high carrier mobility ($1100 \text{ cm}^2\text{V}^{-1}\text{s}^{-1}$) at 6 K.

The following conclusions can be drawn from the work presented in chapter 5.

- Fractured graphene were reconstructed by a high temperature thermal treatment in methane gas, by e-beam irradiation and a sequence involving e-beam irradiation followed by methane gas exposure. Graphene was fractured by applying electrical stress.
- In high temperature thermal treatment with methane gas, formation of covalent bonds induce healing of fractured graphene. In e-beam irradiation method, the dangling bonds are activated at the edges due to current heating and form new covalent bonds and rearrange the carbon networks for joining of fractured graphene layer.
- The physical characterization techniques (AFM, SEM and Raman) confirm the healing of fractured graphene. The crack width range of 5-150 nm was repaired after methane exposure. Raman spectrum before breakdown and after methane exposure/e-beam irradiation shows red shift of G and 2D peaks, and decrease in the ratio of I_{2D}/I_G . The reconstruction process induce doping in the graphene and the number of layers of graphene is increased after reconstruction.
- The current of fractured graphene after reconstruction was restored and it was confirmed by current - voltage characteristics. The maximum current density versus resistivity of pre-breakdown and after reconstruction graphene shows that the thermal treatment in CH_4 does not alter the defect density significantly.
- Fractured graphene can also be reconstructed without the presence of metal on the sample surface due to activation of dangling bonds and high energy states of graphene edges after fracture.
- For e-beam irradiation, individual device has to be irradiated and it would be time-consuming and expensive process. The methane treatment reconstruction process has the potential to be employed for large scale repair of graphene after device processing.

6.1 Future Directions

The following future insights deserve further research efforts.

- GNR width is not controllable using Pt-catalyzed etching technique. This process is not scalable because nanoribbons formation is random and can not be used for mass manufacturing of nanoribbon devices. Graphene nanoribbon width can be controlled by movement of small size nanoparticles. The presence of magnetic field at high temperature may be used for the control of the etching directions of nanoparticles.
- The carrier scattering study is essential to improve transport properties of GNRs. The analytical study of all scattering mechanisms (surface impurity scattering, acoustic phonon and LER scattering) in 3 and 5 nm GNR have been reported at different temperatures. Detailed characterization of the transport at different temperatures over a broader width range could provide more insights into the scattering mechanism. The method presented for the fabrication of GNRs presented in chapter 4 could be interesting for such studies due to the excellent edge properties of the GNR.
- Etching behaviour of epitaxial CVD graphene using metal nano particles can be explored. It might give larger nanoribbons length due to absence of wrinkles and defects which arise due to transfer process in CVD graphene.
- In spite of theoretical modeling of various fracture mechanisms, electrical fracture behavior of graphene need to be focused theoretically and experimentally. A novel experimental technique is required to capture crack propagation and branching in graphene. Fracture behavior like exact position of crack initiation, crack propagation speed and effects of defects on fracture in CVD graphene has to be examined carefully for graphene devices.
- Reconstruction behavior of graphene in the presence of e-beam irradiation and methane gas exposure can be studied theoretically with variants like temperature, methane gas exposure time, voltage range and e-beam irradiation time. This could pave the way for better control of the process, wherein desired number of layers of graphene can be added during the reconstruction process.

Appendices

A.1 Process Recipe for Fabrication of Graphene Nanoribbon Transistors

Step No.	Process Step	Tool used	Process Recipe	Remarks
----------	--------------	-----------	----------------	---------

1	RCA Cleaning	RCA Wet Bench	<ul style="list-style-type: none"> • 2% HF dip - 192 ml DI water + 8 ml (49% HF) for 30 sec • RCA1 - NH₄OH : H₂O₂ : DI H₂O (25 ml : 50 ml : 180 ml) @ 75°C, duration - 1200 sec • 2% HF dip - 192 ml DI water + 8 ml (49%HF) for 30 sec • RCA2 - HCL : H₂O₂ : DI H₂O (25 ml : 50 ml : 180 ml @ 75°C, duration - 1200 sec • 2% HF dip - 192 ml DI water + 8 ml (49% HF) for 30 sec 	
2	Thin Dry Oxide	Dry Oxidation Furnace	<ul style="list-style-type: none"> • Process Time - 34 min. • Process Temperature - 1100°C • N₂ Flow - 2 Div • O₂ Flow - 20 Div 	Check thickness before doing any fresh run
3	RF Cleaning	Sputter Orion	<ul style="list-style-type: none"> • 2 min., RF Power - 50 W 	
4	Graphene Exfoliation	Nano Lab Wet Bench	<ul style="list-style-type: none"> • Graphene exfoliation using HOPG 	

5	Marker to identify graphene flakes	Raith 150 Two	<ul style="list-style-type: none"> • Dehydration - 175°C on hot plate for 120 sec • Resist used - 4% PMMA 950 K • Spin recipe - Step 1 = 500 rpm, 10 sec, step 2 = 4000 rpm, 45 sec, step 3 = 500 rpm, 5 sec • Prebake - 175°C, 120 sec • Exposure - 150 mJ/cm², EHT - 12 keV, aperture - 20 μm, step size - 50 nm • Development - MIBK : IPA (1 : 3) - 40 sec • Post development bake - 175°C, 60 sec 	2-3 dummy run for optimization of numbers
6	Metal Deposition	Sputter Orion	<ul style="list-style-type: none"> • Ti - 150 W, 5 min., • Pt - 100 W, 7 min. 	1 dummy run to check lift-off
7	Lift-off	Nano Lab Wet Bench	<ul style="list-style-type: none"> • Kept in acetone for 15 hours 	

8	Pt Line Arrays Patterning	Raith 150 Two	<ul style="list-style-type: none"> • Dehydration - 175°C on hot plate for 120 sec • Resist used - 2% PMMA 950 K • Spin recipe - Step 1 = 500 rpm, 10 sec, step 2 = 3000 rpm, 45 sec, step 3 = 500 rpm, 5 sec • Prebake - 175°C, 120 sec • Exposure - 120 mJ/cm², EHT - 15 keV, aperture - 20 μm, step size - 50 nm • Development - MIBK : IPA (1 : 3) - 20 sec, • Post development bake - 175°C, 60 sec 	2-3 dummy run to get 1-2 μ m line arrays
9	Pt Deposition	Sputter Orion	<ul style="list-style-type: none"> • Power - 35 W, 2 min. 	
10	Lift-off	Nano Lab Wet Bench	<ul style="list-style-type: none"> • Kept in acetone for 30 min. 	
11	Annealing	General Purpose Annealing Furnace	<ul style="list-style-type: none"> • 20 min. in Ar + H₂ (70: 30)@500°C 	
12	Post-annealing	General Purpose Annealing Furnace	<ul style="list-style-type: none"> • 25 min. in Ar + H₂ (70: 30)@1050°C 	

13	Identify GNRs	Raith 150 Two	<ul style="list-style-type: none"> EHT - 5 keV, Aperture - 30 μm 	
14	Metal Pads	Raith 150 Two	<ul style="list-style-type: none"> Same as in step 5 	
15	Lift-off	Nano Lab Wet Bench	<ul style="list-style-type: none"> Kept in acetone for 15 hours 	

A.2 Physical Characterization

SEM images of the substrate after graphene nanoribbon and device fabrication were taken using Raith-150 Two tool with an accelerating voltage of 5 keV. Topographic images of graphene nanoribbons and graphene were taken using conductive-AFM with 1 Hz scan rate. HR800-UV confocal micro-Raman spectrometer model was used to identify number of graphene layers and edges of graphene nanoribbons. 532 nm - Ar ion laser and 5 mW power was used with 100x objective lens for Raman measurements.

A.3 Graphene Device Fabrication for Reconstruction

Graphene were exfoliated on 100 nm SiO₂ grown on Si wafer. Graphene flakes were located and marked by SEM imaging using Raith 150 Two system. Raith 150 Two system was used for patterning of contacts on graphene flakes using PMMA resist. Developer MIBK : IPA (1 : 3) was used for developing and subsequently metal was deposited using sputtering process. Lift-off process was completed using acetone.

A.4 Device Characterization

Agilent B1500 semiconductor device analyzer was used for measurement of electrical characteristics of graphene and graphene nanoribbons. The contact pins were probed on metal contact pads which are connected to a Keithley switch matrix. Each data point is integrated over 6 Power Line Cycles (PLC) to eliminate transient effect. Low temperature measurement of graphene nanoribbon devices were performed in XCRX-4K cryogenic probe station. Vacuum 1 mTorr was maintained during low temperature measurements.

References

- [1] H. S. Lipson and A. Stokes, “The structure of graphite,” *Proceedings of the Royal Society of London. Series A. Mathematical and Physical Sciences*, vol. 181, no. 984, pp. 101–105, 1942.
- [2] K. S. Novoselov, V. Fal, L. Colombo, P. Gellert, M. Schwab, K. Kim, *et al.*, “A roadmap for graphene,” *Nature*, vol. 490, no. 7419, pp. 192–200, 2012.
- [3] A. S. Mayorov, R. V. Gorbachev, S. V. Morozov, L. Britnell, R. Jalil, L. A. Ponomarenko, P. Blake, K. S. Novoselov, K. Watanabe, T. Taniguchi, *et al.*, “Micrometer-scale ballistic transport in encapsulated graphene at room temperature,” *Nano Letters*, vol. 11, no. 6, pp. 2396–2399, 2011.
- [4] A. A. Balandin, “Thermal properties of graphene and nanostructured carbon materials,” *Nature Materials*, vol. 10, no. 8, pp. 569–581, 2011.
- [5] C. Lee, X. Wei, J. W. Kysar, and J. Hone, “Measurement of the elastic properties and intrinsic strength of monolayer graphene,” *Science*, vol. 321, no. 5887, pp. 385–388, 2008.
- [6] R. R. Nair, P. Blake, A. N. Grigorenko, K. S. Novoselov, T. J. Booth, T. Stauber, N. M. Peres, and A. K. Geim, “Fine structure constant defines visual transparency of graphene,” *Science*, vol. 320, no. 5881, pp. 1308–1308, 2008.
- [7] J. S. Bunch, S. S. Verbridge, J. S. Alden, A. M. Van Der Zande, J. M. Parpia, H. G. Craighead, and P. L. McEuen, “Impermeable atomic membranes from graphene sheets,” *Nano Letters*, vol. 8, no. 8, pp. 2458–2462, 2008.

- [8] K. S. Novoselov, A. K. Geim, S. Morozov, D. Jiang, M. Katsnelson, I. Grigorieva, S. Dubonos, Firsov, and AA, “Two-dimensional gas of massless dirac fermions in graphene,” *Nature*, vol. 438, no. 7065, pp. 197–200, 2005.
- [9] J. Kedzierski, P.-L. Hsu, P. Healey, P. W. Wyatt, C. L. Keast, M. Sprinkle, C. Berger, and W. A. De Heer, “Epitaxial graphene transistors on SiC substrates,” *IEEE Transactions on Electron Devices*, vol. 55, no. 8, pp. 2078–2085, 2008.
- [10] F. Xia, T. Mueller, Y.-m. Lin, A. Valdes-Garcia, and P. Avouris, “Ultrafast graphene photodetector,” *Nature Nanotechnology*, vol. 4, no. 12, pp. 839–847, 2009.
- [11] J. D. Fowler, M. J. Allen, V. C. Tung, Y. Yang, R. B. Kaner, and B. H. Weiller, “Practical chemical sensors from chemically derived graphene,” *ACS Nano*, vol. 3, no. 2, pp. 301–306, 2009.
- [12] S.-K. Lee, B. J. Kim, H. Jang, S. C. Yoon, C. Lee, B. H. Hong, J. A. Rogers, J. H. Cho, and J.-H. Ahn, “Stretchable graphene transistors with printed dielectrics and gate electrodes,” *Nano Letters*, vol. 11, no. 11, pp. 4642–4646, 2011.
- [13] Y. Zhang, Y.-W. Tan, H. L. Stormer, and P. Kim, “Experimental observation of the quantum Hall effect and Berry’s phase in graphene,” *Nature*, vol. 438, no. 7065, pp. 201–204, 2005.
- [14] A. K. Geim and K. S. Novoselov, “The rise of graphene,” in *Nanoscience and Technology: A Collection of Reviews from Nature Journals*, pp. 11–19, World Scientific, 2010.
- [15] K. S. Novoselov, A. K. Geim, S. V. Morozov, D. Jiang, Y. Zhang, S. V. Dubonos, I. V. Grigorieva, and A. A. Firsov, “Electric field effect in atomically thin carbon films,” *science*, vol. 306, no. 5696, pp. 666–669, 2004.
- [16] Y. Yao, Z. Li, Z. Lin, K.-S. Moon, J. Agar, and C. Wong, “Controlled growth of multilayer, few-layer, and single-layer graphene on metal substrates,” *The Journal of Physical Chemistry C*, vol. 115, no. 13, pp. 5232–5238, 2011.
- [17] L. Jiao, L. Zhang, X. Wang, G. Diankov, and H. Dai, “Narrow graphene nanoribbons from carbon nanotubes,” *Nature*, vol. 458, no. 7240, pp. 877–880, 2009.

- [18] X. Li, X. Wang, L. Zhang, S. Lee, and H. Dai, “Chemically derived, ultrasmooth graphene nanoribbon semiconductors,” *Science*, vol. 319, no. 5867, pp. 1229–1232, 2008.
- [19] L. Ponomarenko, F. Schedin, M. Katsnelson, R. Yang, E. Hill, K. Novoselov, and A. Geim, “Chaotic Dirac billiard in graphene quantum dots,” *Science*, vol. 320, no. 5874, pp. 356–358, 2008.
- [20] L. Villamagua, M. Carini, A. Stashans, and C. V. Gomez, “Band gap engineering of graphene through quantum confinement and edge distortions,” *Ricerche di Matematica*, vol. 65, no. 2, pp. 579–584, 2016.
- [21] W. J. Yu and X. Duan, “Tunable transport gap in narrow bilayer graphene nanoribbons,” *Scientific Reports*, vol. 3, pp. 1–5, 2013.
- [22] Y.-W. Son, M. L. Cohen, and S. G. Louie, “Energy gaps in graphene nanoribbons,” *Physical Review Letters*, vol. 97, no. 21, p. 216803, 2006.
- [23] K. Nakada, M. Fujita, G. Dresselhaus, and M. S. Dresselhaus, “Edge state in graphene ribbons: Nanometer size effect and edge shape dependence,” *Physical Review B*, vol. 54, no. 24, pp. 17954–17960, 1996.
- [24] X. Jia, J. Campos-Delgado, M. Terrones, V. Meunier, and M. S. Dresselhaus, “Graphene edges: a review of their fabrication and characterization,” *Nanoscale*, vol. 3, no. 1, pp. 86–95, 2011.
- [25] M. Y. Han, B. Özyilmaz, Y. Zhang, and P. Kim, “Energy band-gap engineering of graphene nanoribbons,” *Physical Review Letters*, vol. 98, no. 20, p. 206805, 2007.
- [26] P. Kim, M. Y. Han, A. F. Young, I. Meric, and K. L. Shepard, “Graphene nanoribbon devices and quantum heterojunction devices,” in *IEEE International Electron Devices Meeting*, pp. 241–244, IEEE, 2009.
- [27] Z. Chen, Y.-M. Lin, M. J. Rooks, and P. Avouris, “Graphene nano-ribbon electronics,” *Physica E: Low-dimensional Systems and Nanostructures*, vol. 40, no. 2, pp. 228–232, 2007.

- [28] M. Evaldsson, I. V. Zozoulenko, H. Xu, and T. Heinzl, “Edge-disorder-induced Anderson localization and conduction gap in graphene nanoribbons,” *Physical Review B*, vol. 78, no. 16, p. 161407, 2008.
- [29] F. Cervantes-Sodi, G. Csányi, S. Piscanec, and A. Ferrari, “Edge-functionalized and substitutionally doped graphene nanoribbons: Electronic and spin properties,” *Physical Review B*, vol. 77, no. 16, p. 165427, 2008.
- [30] H. Raza and E. C. Kan, “Armchair graphene nanoribbons: Electronic structure and electric-field modulation,” *Physical Review B*, vol. 77, no. 24, p. 245434, 2008.
- [31] X. Wang, Y. Ouyang, X. Li, H. Wang, J. Guo, and H. Dai, “Room-temperature all-semiconducting sub-10-nm graphene nanoribbon field-effect transistors,” *Physical Review Letters*, vol. 100, no. 20, p. 206803, 2008.
- [32] P. Jangid, D. Pathan, and A. Kottantharayil, “Graphene nanoribbon transistors with high I_{ON}/I_{OFF} ratio and mobility,” *Carbon*, vol. 132, pp. 65–70, 2018.
- [33] L. Jiao, X. Wang, G. Diankov, H. Wang, and H. Dai, “Facile synthesis of high-quality graphene nanoribbons,” *Nature Nanotechnology*, vol. 5, no. 5, pp. 321–325, 2010.
- [34] T. Zhang, X. Li, and H. Gao, “Fracture of graphene: a review,” *International Journal of Fracture*, vol. 196, no. 1-2, pp. 1–31, 2015.
- [35] R. Murali, Y. Yang, K. Brenner, T. Beck, and J. D. Meindl, “Breakdown current density of graphene nanoribbons,” *Applied Physics Letters*, vol. 94, no. 24, p. 243114, 2009.
- [36] P. Zhang, L. Ma, F. Fan, Z. Zeng, C. Peng, P. E. Loya, Z. Liu, Y. Gong, J. Zhang, X. Zhang, *et al.*, “Fracture toughness of graphene,” *Nature Communications*, vol. 5, p. 3782, 2014.
- [37] C. S. Ruiz-Vargas, H. L. Zhuang, P. Y. Huang, A. M. Van Der Zande, S. Garg, P. L. McEuen, D. A. Muller, R. G. Hennig, and J. Park, “Softened elastic response and unzipping in chemical vapor deposition graphene membranes,” *Nano Letters*, vol. 11, no. 6, pp. 2259–2263, 2011.

- [38] L.-Y. Lin, D.-E. Kim, W.-K. Kim, and S.-C. Jun, “Friction and wear characteristics of multi-layer graphene films investigated by atomic force microscopy,” *Surface and Coatings Technology*, vol. 205, no. 20, pp. 4864–4869, 2011.
- [39] P. Y. Huang, C. S. Ruiz-Vargas, A. M. Van Der Zande, W. S. Whitney, M. P. Levendorf, J. W. Kevek, S. Garg, J. S. Alden, C. J. Hustedt, Y. Zhu, *et al.*, “Grains and grain boundaries in single-layer graphene atomic patchwork quilts,” *Nature*, vol. 469, no. 7330, pp. 389–392, 2011.
- [40] H. B. Chew, M.-W. Moon, K. Lee, and K.-S. Kim, “Compressive dynamic scission of carbon nanotubes under sonication: fracture by atomic ejection,” *Proceedings of the Royal Society A: Mathematical, Physical and Engineering Sciences*, vol. 467, no. 2129, pp. 1270–1289, 2010.
- [41] L. Yang, C.-H. Park, Y.-W. Son, M. L. Cohen, and S. G. Louie, “Quasiparticle energies and band gaps in graphene nanoribbons,” *Physical Review Letters*, vol. 99, no. 18, p. 186801, 2007.
- [42] P. Nemes-Incze, L. Tapasztó, G. Z. Magda, Z. Osváth, G. Dobrik, X. Jin, C. Hwang, and L. Biró, “Graphene nanoribbons with zigzag and armchair edges prepared by scanning tunneling microscope lithography on gold substrates,” *Applied Surface Science*, vol. 291, pp. 48–52, 2014.
- [43] L. P. Biro and P. Lambin, “Nanopatterning of graphene with crystallographic orientation control,” *Carbon*, vol. 48, no. 10, pp. 2677–2689, 2010.
- [44] D. V. Kosynkin, A. L. Higginbotham, A. Sinitskii, J. R. Lomeda, A. Dimiev, B. K. Price, and J. M. Tour, “Longitudinal unzipping of carbon nanotubes to form graphene nanoribbons,” *Nature*, vol. 458, no. 7240, pp. 872–879, 2009.
- [45] S. Ryu, J. Maultzsch, M. Y. Han, P. Kim, and L. E. Brus, “Raman spectroscopy of lithographically patterned graphene nanoribbons,” *ACS Nano*, vol. 5, no. 5, pp. 4123–4130, 2011.
- [46] L. Talirz, P. Ruffieux, and R. Fasel, “On-surface synthesis of atomically precise graphene nanoribbons,” *Advanced Materials*, vol. 28, no. 29, pp. 6222–6231, 2016.

- [47] H. Ago, Y. Kayo, P. Solís-Fernández, K. Yoshida, and M. Tsuji, “Synthesis of high-density arrays of graphene nanoribbons by anisotropic metal-assisted etching,” *Carbon*, vol. 78, pp. 339–346, 2014.
- [48] R. Zou, Z. Zhang, K. Xu, L. Jiang, Q. Tian, Y. Sun, Z. Chen, and J. Hu, “A method for joining individual graphene sheets,” *Carbon*, vol. 50, no. 13, pp. 4965–4972, 2012.
- [49] C. Berger, Z. Song, T. Li, X. Li, A. Y. Ogbazghi, R. Feng, Z. Dai, A. N. Marchenkov, E. H. Conrad, P. N. First, *et al.*, “Ultrathin epitaxial graphite: 2d electron gas properties and a route toward graphene-based nanoelectronics,” *The Journal of Physical Chemistry B*, vol. 108, no. 52, pp. 19912–19916, 2004.
- [50] E. McCann and M. Koshino, “The electronic properties of bilayer graphene,” *Reports on Progress in Physics*, vol. 76, no. 5, p. 056503, 2013.
- [51] A. C. Neto, F. Guinea, N. M. Peres, K. S. Novoselov, and A. K. Geim, “The electronic properties of graphene,” *Reviews of Modern Physics*, vol. 81, no. 1, pp. 109–162, 2009.
- [52] H. Rashid, A. Koel, and T. Rang, “Simulations of propane and butane gas sensor based on pristine armchair graphene nanoribbon,” in *IOP Conference Series: Materials Science and Engineering*, vol. 362, p. 012001, IOP Publishing, 2018.
- [53] C. Tao, L. Jiao, O. V. Yazyev, Y.-C. Chen, J. Feng, X. Zhang, R. B. Capaz, J. M. Tour, A. Zettl, S. G. Louie, *et al.*, “Spatially resolving edge states of chiral graphene nanoribbons,” *Nature Physics*, vol. 7, no. 8, pp. 616–620, 2011.
- [54] C. L. Kane and E. J. Mele, “Quantum spin Hall effect in graphene,” *Physical Review Letters*, vol. 95, no. 22, p. 226801, 2005.
- [55] O. V. Yazyev, “A guide to the design of electronic properties of graphene nanoribbons,” *Accounts of Chemical Research*, vol. 46, no. 10, pp. 2319–2328, 2013.
- [56] V. Barone, O. Hod, and G. E. Scuseria, “Electronic structure and stability of semiconducting graphene nanoribbons,” *Nano Letters*, vol. 6, no. 12, pp. 2748–2754, 2006.

- [57] O. V. Yazyev, R. B. Capaz, and S. G. Louie, “Theory of magnetic edge states in chiral graphene nanoribbons,” *Physical Review B*, vol. 84, no. 11, p. 115406, 2011.
- [58] A. Akhmerov and C. Beenakker, “Boundary conditions for dirac fermions on a terminated honeycomb lattice,” *Physical Review B*, vol. 77, no. 8, p. 085423, 2008.
- [59] P. B. Bennett, Z. Pedramrazi, A. Madani, Y.-C. Chen, D. G. de Oteyza, C. Chen, F. R. Fischer, M. F. Crommie, and J. Bokor, “Bottom-up graphene nanoribbon field-effect transistors,” *Applied Physics Letters*, vol. 103, no. 25, p. 253114, 2013.
- [60] P. Solís-Fernández, K. Yoshida, Y. Ogawa, M. Tsuji, and H. Ago, “Dense arrays of highly aligned graphene nanoribbons produced by substrate-controlled metal-assisted etching of graphene,” *Advanced Materials*, vol. 25, no. 45, pp. 6562–6568, 2013.
- [61] F. Xia, D. B. Farmer, Y.-m. Lin, and P. Avouris, “Graphene field-effect transistors with high on/off current ratio and large transport band gap at room temperature,” *Nano Letters*, vol. 10, no. 2, pp. 715–718, 2010.
- [62] W. S. Hwang, K. Tahy, X. Li, H. Xing, A. C. Seabaugh, C. Y. Sung, and D. Jena, “Transport properties of graphene nanoribbon transistors on chemical-vapor-deposition grown wafer-scale graphene,” *Applied Physics Letters*, vol. 100, no. 20, p. 203107, 2012.
- [63] S. Ilani, L. A. Donev, M. Kindermann, and P. L. McEuen, “Measurement of the quantum capacitance of interacting electrons in carbon nanotubes,” *Nature Physics*, vol. 2, no. 10, pp. 687–691, 2006.
- [64] Y. Ouyang, Y. Yoon, and J. Guo, “Scaling behaviors of graphene nanoribbon FETs: A three-dimensional quantum simulation study,” *IEEE Transactions on Electron Devices*, vol. 54, no. 9, pp. 2223–2231, 2007.
- [65] Y. Yoon and J. Guo, “Effect of edge roughness in graphene nanoribbon transistors,” *Applied Physics Letters*, vol. 91, no. 7, p. 073103, 2007.
- [66] W. S. Hwang, P. Zhao, K. Tahy, L. O. Nyakiti, V. D. Wheeler, R. L. Myers-Ward, C. R. Eddy Jr, D. K. Gaskill, J. A. Robinson, W. Haensch, *et al.*, “Graphene

- nanoribbon field-effect transistors on wafer-scale epitaxial graphene on SiC substrates,” *APL Materials*, vol. 3, no. 1, p. 011101, 2015.
- [67] W. S. Hwang, K. Tahy, L. O. Nyakiti, V. D. Wheeler, R. L. Myers-Ward, C. Eddy Jr, D. K. Gaskill, H. Xing, A. Seabaugh, and D. Jena, “Fabrication of top-gated epitaxial graphene nanoribbon FETs using hydrogen-silsesquioxane,” *Journal of Vacuum Science & Technology B, Nanotechnology and Microelectronics: Materials, Processing, Measurement, and Phenomena*, vol. 30, no. 3, p. 03D104, 2012.
- [68] L. Brey and H. Fertig, “Electronic states of graphene nanoribbons studied with the Dirac equation,” *Physical Review B*, vol. 73, no. 23, p. 235411, 2006.
- [69] F. Molitor, A. Jacobsen, C. Stampfer, J. Güttinger, T. Ihn, and K. Ensslin, “Transport gap in side-gated graphene constrictions,” *Physical Review B*, vol. 79, no. 7, p. 075426, 2009.
- [70] M. Sprinkle, M. Ruan, Y. Hu, J. Hankinson, M. Rubio-Roy, B. Zhang, X. Wu, C. Berger, and W. A. De Heer, “Scalable templated growth of graphene nanoribbons on sic,” *Nature Nanotechnology*, vol. 5, no. 10, p. 727, 2010.
- [71] V. E. Dorgan, M.-H. Bae, and E. Pop, “Mobility and saturation velocity in graphene on SiO₂,” *Applied Physics Letters*, vol. 97, no. 8, p. 082112, 2010.
- [72] A. Deshpande, W. Bao, F. Miao, C. N. Lau, and B. J. LeRoy, “Spatially resolved spectroscopy of monolayer graphene on sio₂,” *Physical Review B*, vol. 79, no. 20, p. 205411, 2009.
- [73] Y. Gong, M. Long, G. Liu, S. Gao, C. Zhu, X. Wei, X. Geng, M. Sun, C. Yang, L. Lu, *et al.*, “Electronic transport properties of graphene nanoribbon arrays fabricated by unzipping aligned nanotubes,” *Physical Review B*, vol. 87, no. 16, p. 165404, 2013.
- [74] Y. Zhang, C. Hui, R. Sun, K. Li, K. He, X. Ma, and F. Liu, “A large-area 15 nm graphene nanoribbon array patterned by a focused ion beam,” *Nanotechnology*, vol. 25, no. 13, p. 135301, 2014.

- [75] J. Cai, P. Ruffieux, R. Jaafar, M. Bieri, T. Braun, S. Blankenburg, M. Muoth, A. P. Seitsonen, M. Saleh, X. Feng, *et al.*, “Atomically precise bottom-up fabrication of graphene nanoribbons,” *Nature*, vol. 466, no. 7305, pp. 470–473, 2010.
- [76] W. Kim, A. Javey, O. Vermesh, Q. Wang, Y. Li, and H. Dai, “Hysteresis caused by water molecules in carbon nanotube field-effect transistors,” *Nano Letters*, vol. 3, no. 2, pp. 193–198, 2003.
- [77] J. Chan, A. Venugopal, A. Pirkle, S. McDonnell, D. Hinojos, C. W. Magnuson, R. S. Ruoff, L. Colombo, R. M. Wallace, and E. M. Vogel, “Reducing extrinsic performance-limiting factors in graphene grown by chemical vapor deposition,” *ACS Nano*, vol. 6, no. 4, pp. 3224–3229, 2012.
- [78] V. Derycke, R. Martel, J. Appenzeller, and P. Avouris, “Controlling doping and carrier injection in carbon nanotube transistors,” *Applied Physics Letters*, vol. 80, no. 15, pp. 2773–2775, 2002.
- [79] L. C. Campos, V. R. Manfrinato, J. D. Sanchez-Yamagishi, J. Kong, and P. Jarillo-Herrero, “Anisotropic etching and nanoribbon formation in single-layer graphene,” *Nano Letters*, vol. 9, no. 7, pp. 2600–2604, 2009.
- [80] Y. You, Z. Ni, T. Yu, and Z. Shen, “Edge chirality determination of graphene by Raman spectroscopy,” *Applied Physics Letters*, vol. 93, no. 16, p. 163112, 2008.
- [81] J.-H. Chen, C. Jang, S. Xiao, M. Ishigami, and M. S. Fuhrer, “Intrinsic and extrinsic performance limits of graphene devices on SiO₂,” *Nature Nanotechnology*, vol. 3, no. 4, pp. 206–209, 2008.
- [82] S. Xiao and T. Belytschko, “A bridging domain method for coupling continua with molecular dynamics,” *Computer Methods in Applied Mechanics and Engineering*, vol. 193, no. 17-20, pp. 1645–1669, 2004.
- [83] A. Omeltchenko, J. Yu, R. K. Kalia, and P. Vashishta, “Crack front propagation and fracture in a graphite sheet: a molecular-dynamics study on parallel computers,” *Physical Review Letters*, vol. 78, no. 11, p. 2148, 1997.
- [84] Z. Zhang, A. Kutana, and B. I. Yakobson, “Edge reconstruction-mediated graphene fracture,” *Nanoscale*, vol. 7, no. 6, pp. 2716–2722, 2015.

- [85] X. Jia, M. Hofmann, V. Meunier, B. G. Sumpter, J. Campos-Delgado, J. M. Romo-Herrera, H. Son, Y.-P. Hsieh, A. Reina, J. Kong, *et al.*, “Controlled formation of sharp zigzag and armchair edges in graphitic nanoribbons,” *Science*, vol. 323, no. 5922, pp. 1701–1705, 2009.
- [86] L. Meng, J. Jiang, J. Wang, and F. Ding, “Mechanism of metal catalyzed healing of large structural defects in graphene,” *The Journal of Physical Chemistry C*, vol. 118, no. 1, pp. 720–724, 2013.
- [87] I. Childres, L. A. Jauregui, M. Foxe, J. Tian, R. Jalilian, I. Jovanovic, and Y. P. Chen, “Effect of electron-beam irradiation on graphene field effect devices,” *Applied Physics Letters*, vol. 97, no. 17, p. 173109, 2010.
- [88] D. Sen, K. S. Novoselov, P. M. Reis, and M. J. Buehler, “Tearing graphene sheets from adhesive substrates produces tapered nanoribbons,” *Small*, vol. 6, no. 10, pp. 1108–1116, 2010.
- [89] J.-H. Lee, P. E. Loya, J. Lou, and E. L. Thomas, “Dynamic mechanical behavior of multilayer graphene via supersonic projectile penetration,” *Science*, vol. 346, no. 6213, pp. 1092–1096, 2014.
- [90] K.-J. Lee, A. P. Chandrakasan, and J. Kong, “Breakdown current density of CVD-grown multilayer graphene interconnects,” *IEEE Electron Device Letters*, vol. 32, no. 4, pp. 557–559, 2011.
- [91] F. Banhart, “Irradiation effects in carbon nanostructures,” *Reports on Progress in Physics*, vol. 62, no. 8, pp. 1181–1221, 1999.
- [92] A. Du, S. C. Smith, and G. Lu, “Formation of single-walled carbon nanotube via the interaction of graphene nanoribbons: ab initio density functional calculations,” *Nano Letters*, vol. 7, no. 11, pp. 3349–3354, 2007.
- [93] B. Wei, R. Vajtai, and P. Ajayan, “Reliability and current carrying capacity of carbon nanotubes,” *Applied Physics Letters*, vol. 79, no. 8, pp. 1172–1174, 2001.
- [94] F. Kreupl, A. P. Graham, G. Duesberg, W. Steinhögl, M. Liebau, E. Unger, and W. Hönlein, “Carbon nanotubes in interconnect applications,” *Microelectronic Engineering*, vol. 64, no. 1-4, pp. 399–408, 2002.

- [95] P. G. Collins, M. S. Arnold, and P. Avouris, "Engineering carbon nanotubes and nanotube circuits using electrical breakdown," *Science*, vol. 292, no. 5517, pp. 706–709, 2001.
- [96] K. Mølhave, S. B. Gudnason, A. T. Pedersen, C. H. Clausen, A. Horsewell, and P. Bøggild, "Transmission electron microscopy study of individual carbon nanotube breakdown caused by Joule heating in air," *Nano Letters*, vol. 6, no. 8, pp. 1663–1668, 2006.
- [97] M. Tsutsui, Y.-k. Taninouchi, S. Kurokawa, and A. Sakai, "Electrical breakdown of short multiwalled carbon nanotubes," *Journal of Applied Physics*, vol. 100, no. 9, p. 094302, 2006.
- [98] N. Kulshrestha, A. Misra, K. S. Hazra, S. Roy, R. Bajpai, D. R. Mohapatra, and D. Misra, "Healing of broken multiwalled carbon nanotubes using very low energy electrons in SEM: a route toward complete recovery," *ACS Nano*, vol. 5, no. 3, pp. 1724–1730, 2011.
- [99] S. Dhall, G. Vaidya, and N. Jaggi, "Joining of broken multiwalled carbon nanotubes using an electron beam-induced deposition (EBID) technique," *Journal of Electronic Materials*, vol. 43, no. 9, pp. 3283–3289, 2014.
- [100] S. Mathew, U. Bhatta, J. Ghatak, B. Sekhar, and B. Dev, "The effects of 2 MeV Ag ion irradiation on multiwalled carbon nanotubes," *Carbon*, vol. 45, no. 13, pp. 2659–2664, 2007.
- [101] H. M. Kim, H. S. Kim, S. K. Park, J. Joo, T. J. Lee, and C. J. Lee, "Morphological change of multiwalled carbon nanotubes through high-energy (MeV) ion irradiation," *Journal of Applied Physics*, vol. 97, no. 2, pp. 2003–2006, 2005.
- [102] C.-H. Kiang, W. A. Goddard, R. Beyers, and D. S. Bethune, "Structural modification of single-layer carbon nanotubes with an electron beam," *The Journal of Physical Chemistry*, vol. 100, no. 9, pp. 3749–3752, 1996.
- [103] C. Claeys and E. Simoen, *Radiation effects in advanced semiconductor materials and devices*, vol. 57. Springer Science & Business Media, 2013.

- [104] A. Krashennnikov and K. Nordlund, “Ion and electron irradiation-induced effects in nanostructured materials,” *Journal of Applied Physics*, vol. 107, no. 7, p. 3, 2010.
- [105] D. Teweldebrhan and A. A. Balandin, “Modification of graphene properties due to electron-beam irradiation,” *Applied Physics Letters*, vol. 94, no. 1, p. 013101, 2009.
- [106] M. Xu, D. Fujita, and N. Hanagata, “Monitoring electron-beam irradiation effects on graphenes by temporal Auger electron spectroscopy,” *Nanotechnology*, vol. 21, no. 26, p. 265705, 2010.
- [107] S. Kang, H. C. Movva, A. Sanne, A. Rai, and S. K. Banerjee, “Influence of electron-beam lithography exposure current level on the transport characteristics of graphene field effect transistors,” *Journal of Applied Physics*, vol. 119, no. 12, p. 124502, 2016.
- [108] C. Casiraghi, S. Pisana, K. Novoselov, A. Geim, and A. Ferrari, “Raman fingerprint of charged impurities in graphene,” *Applied Physics Letters*, vol. 91, no. 23, p. 233108, 2007.
- [109] S. O. Woo and W. Teizer, “The effect of electron induced hydrogenation of graphene on its electrical transport properties,” *Applied Physics Letters*, vol. 103, no. 4, p. 041603, 2013.
- [110] M. Lafkioti, B. Krauss, T. Lohmann, U. Zschieschang, H. Klauk, K. V. Klitzing, and J. H. Smet, “Graphene on a hydrophobic substrate: doping reduction and hysteresis suppression under ambient conditions,” *Nano Letters*, vol. 10, no. 4, pp. 1149–1153, 2010.
- [111] F. Chen, J. Xia, D. K. Ferry, and N. Tao, “Dielectric screening enhanced performance in graphene FET,” *Nano Letters*, vol. 9, no. 7, pp. 2571–2574, 2009.
- [112] C. Deng, W. Lin, G. Agnus, D. Dragoe, D. Pierucci, A. Ouerghi, S. Eimer, I. Barisic, D. Ravelosona, C. Chappert, *et al.*, “Reversible charge-transfer doping in graphene due to reaction with polymer residues,” *The Journal of Physical Chemistry C*, vol. 118, no. 25, pp. 13890–13897, 2014.

- [113] S. F. Chowdhury, S. Sonde, S. Rahimi, L. Tao, S. Banerjee, and D. Akinwande, “Improvement of graphene field-effect transistors by hexamethyldisilazane surface treatment,” *Applied Physics Letters*, vol. 105, no. 3, p. 033117, 2014.
- [114] A. Krasheninnikov and F. Banhart, “Engineering of nanostructured carbon materials with electron or ion beams,” *Nature Materials*, vol. 6, no. 10, pp. 723–733, 2007.
- [115] J. H. Warner, M. H. Rummeli, L. Ge, T. Gemming, B. Montanari, N. M. Harrison, B. Büchner, and G. A. D. Briggs, “Structural transformations in graphene studied with high spatial and temporal resolution,” *Nature Nanotechnology*, vol. 4, no. 8, pp. 500–504, 2009.
- [116] K. Murakami, T. Kadowaki, and J.-i. Fujita, “Damage and strain in single-layer graphene induced by very-low-energy electron-beam irradiation,” *Applied Physics Letters*, vol. 102, no. 4, p. 043111, 2013.
- [117] Y. H. He, L. Wang, X. Chen, Z. Wu, W. Li, Y. Cai, and N. Wang, “Modifying electronic transport properties of graphene by electron beam irradiation,” *Applied Physics Letters*, vol. 99, no. 3, p. 033109, 2011.
- [118] F. Giubileo, A. Di Bartolomeo, N. Martucciello, F. Romeo, L. Iemmo, P. Romano, and M. Passacantando, “Contact resistance and channel conductance of graphene field-effect transistors under low-energy electron irradiation,” *Nanomaterials*, vol. 6, no. 11, p. 206, 2016.
- [119] F. Schedin, A. Geim, S. Morozov, E. Hill, P. Blake, M. Katsnelson, and K. Novoselov, “Detection of individual gas molecules adsorbed on graphene,” *Nature Materials*, vol. 6, no. 9, pp. 652–655, 2007.
- [120] S. Ryu, L. Liu, S. Berciaud, Y.-J. Yu, H. Liu, P. Kim, G. W. Flynn, and L. E. Brus, “Atmospheric oxygen binding and hole doping in deformed graphene on a SiO_2 substrate,” *Nano Letters*, vol. 10, no. 12, pp. 4944–4951, 2010.
- [121] A. Pirkle, J. Chan, A. Venugopal, D. Hinojos, C. Magnuson, S. McDonnell, L. Colombo, E. Vogel, R. Ruoff, and R. Wallace, “The effect of chemical residues

- on the physical and electrical properties of chemical vapor deposited graphene transferred to SiO₂,” *Applied Physics Letters*, vol. 99, no. 12, p. 122108, 2011.
- [122] H. Wang, Y. Wu, C. Cong, J. Shang, and T. Yu, “Hysteresis of electronic transport in graphene transistors,” *ACS Nano*, vol. 4, no. 12, pp. 7221–7228, 2010.
- [123] A. Di Bartolomeo, M. Rinzan, A. K. Boyd, Y. Yang, L. Guadagno, F. Giubileo, and P. Barbara, “Electrical properties and memory effects of field-effect transistors from networks of single- and double-walled carbon nanotubes,” *Nanotechnology*, vol. 21, no. 11, p. 115204, 2010.
- [124] A. Venugopal, L. Colombo, and E. M. Vogel, “Issues with characterizing transport properties of graphene field effect transistors,” *Solid State Communications*, vol. 152, no. 15, pp. 1311–1316, 2012.
- [125] R. Murali, K. Brenner, Y. Yang, T. Beck, and J. D. Meindl, “Resistivity of graphene nanoribbon interconnects,” *IEEE Electron Device Letters*, vol. 30, no. 6, pp. 611–613, 2009.
- [126] P. G. Collins, M. Hersam, M. Arnold, R. Martel, and P. Avouris, “Current saturation and electrical breakdown in multiwalled carbon nanotubes,” *Physical Review Letters*, vol. 86, no. 14, p. 3128, 2001.
- [127] Y.-W. Tan, Y. Zhang, K. Bolotin, Y. Zhao, S. Adam, E. Hwang, S. D. Sarma, H. Stormer, and P. Kim, “Measurement of scattering rate and minimum conductivity in graphene,” *Physical Review Letters*, vol. 99, no. 24, p. 246803, 2007.
- [128] X. Chen, K.-J. Lee, D. Akinwande, G. F. Close, S. Yasuda, B. Paul, S. Fujita, J. Kong, and H.-S. P. Wong, “High-speed graphene interconnects monolithically integrated with CMOS ring oscillators operating at 1.3 GHz,” in *IEEE International Electron Devices Meeting*, pp. 581–584, IEEE, 2009.
- [129] M. Suzuki, Y. Ominami, Q. Ngo, C. Y. Yang, A. M. Cassell, and J. Li, “Current-induced breakdown of carbon nanofibers,” *Journal of Applied Physics*, vol. 101, no. 11, p. 114307, 2007.

- [130] W. Fang, A. L. Hsu, R. Caudillo, Y. Song, A. G. Birdwell, E. Zakar, M. Kalbac, M. Dubey, T. Palacios, M. S. Dresselhaus, *et al.*, “Rapid identification of stacking orientation in isotopically labeled chemical-vapor grown bilayer graphene by Raman spectroscopy,” *Nano Letters*, vol. 13, no. 4, pp. 1541–1548, 2013.
- [131] S. Okazaki, “Resolution limits of optical lithography,” *Journal of Vacuum Science & Technology B: Microelectronics and Nanometer Structures Processing, Measurement, and Phenomena*, vol. 9, no. 6, pp. 2829–2833, 1991.
- [132] L. De Broglie, “The wave nature of the electron,” *Nobel Lecture*, vol. 12, pp. 244–256, 1929.
- [133] R. Gillibert, J. Q. Huang, Y. Zhang, W. L. Fu, and M. L. de La Chapelle, “Explosive detection by surface enhanced Raman scattering,” *TrAC Trends in Analytical Chemistry*, vol. 105, pp. 166–172, 2018.
- [134] B. W. Smith and K. Suzuki, *Microlithography: science and technology*, vol. 126. CRC press, 2018.
- [135] P. Rai-Choudhury, *Handbook of microlithography, micromachining, and microfabrication: microlithography*, vol. 1. Iet, 1997.
- [136] J. L. Vossen, W. Kern, and W. Kern, *Thin film processes II*, vol. 2. Gulf Professional Publishing, 1991.
- [137] P. Blake, E. Hill, A. Castro Neto, K. Novoselov, D. Jiang, R. Yang, T. Booth, and A. Geim, “Making graphene visible,” *Applied Physics Letters*, vol. 91, no. 6, p. 063124, 2007.
- [138] G. Hübschen, I. Altpeter, R. Tschuncky, and H.-G. Herrmann, *Materials characterization using Nondestructive Evaluation (NDE) methods*. Woodhead publishing, 2016.
- [139] A. Vilalta-Clemente, K. Gloystein, and N. Frangis, “Principles of atomic force microscopy (AFM),” *Proceedings of Physics of Advanced Materials Winter School*, 2008.

- [140] A. C. Ferrari, J. Meyer, V. Scardaci, C. Casiraghi, M. Lazzeri, F. Mauri, S. Piscanec, D. Jiang, K. Novoselov, S. Roth, *et al.*, “Raman spectrum of graphene and graphene layers,” *Physical Review Letters*, vol. 97, no. 18, p. 187401, 2006.
- [141] M. Dresselhaus, G. Dresselhaus, and M. Hofmann, “Raman spectroscopy as a probe of graphene and carbon nanotubes,” *Philosophical Transactions of the Royal Society A: Mathematical, Physical and Engineering Sciences*, vol. 366, no. 1863, pp. 231–236, 2007.
- [142] Y. Wang, D. C. Alsmeyer, and R. L. McCreery, “Raman spectroscopy of carbon materials: structural basis of observed spectra,” *Chemistry of Materials*, vol. 2, no. 5, pp. 557–563, 1990.
- [143] C. Thomsen and S. Reich, “Double resonant Raman scattering in graphite,” *Physical Review Letters*, vol. 85, no. 24, p. 5214, 2000.
- [144] L. Malard, M. Pimenta, G. Dresselhaus, and M. Dresselhaus, “Raman spectroscopy in graphene,” *Physics Reports*, vol. 473, no. 5-6, pp. 51–87, 2009.
- [145] A. Gupta, G. Chen, P. Joshi, S. Tadigadapa, and P. Eklund, “Raman scattering from high-frequency phonons in supported n-graphene layer films,” *Nano Letters*, vol. 6, no. 12, pp. 2667–2673, 2006.
- [146] R. J. Nemanich and S. Solin, “First-and second-order Raman scattering from finite-size crystals of graphite,” *Physical Review B*, vol. 20, no. 2, p. 392, 1979.
- [147] R. Vidano, D. Fischbach, L. Willis, and T. Loehr, “Observation of Raman band shifting with excitation wavelength for carbons and graphites,” *Solid State Communications*, vol. 39, no. 2, pp. 341–344, 1981.
- [148] P. Venezuela, M. Lazzeri, and F. Mauri, “Theory of double-resonant Raman spectra in graphene: Intensity and line shape of defect-induced and two-phonon bands,” *Physical Review B*, vol. 84, no. 3, p. 035433, 2011.
- [149] A. C. Ferrari, “Raman spectroscopy of graphene and graphite: disorder, electron-phonon coupling, doping and nonadiabatic effects,” *Solid State Communications*, vol. 143, no. 1-2, pp. 47–57, 2007.

- [150] L. Cancado, M. Pimenta, B. Neves, M. Dantas, and A. Jorio, "Influence of the atomic structure on the Raman spectra of graphite edges," *Physical Review Letters*, vol. 93, no. 24, p. 247401, 2004.
- [151] L. Ma, J. Wang, J. Yip, and F. Ding, "Mechanism of transition-metal nanoparticle catalytic graphene cutting," *The Journal of Physical Chemistry Letters*, vol. 5, no. 7, pp. 1192–1197, 2014.
- [152] A. Tomita and Y. Tamai, "Optical microscopic study on the catalytic hydrogenation of graphite," *The Journal of Physical Chemistry*, vol. 78, no. 22, pp. 2254–2258, 1974.
- [153] P. J. Goethel and R. T. Yang, "Mechanism of graphite hydrogenation catalyzed by nickel," *Journal of Catalysis*, vol. 108, no. 2, pp. 356–363, 1987.
- [154] H. Uchida, M. Kiso, T. Nakamura, T. Kamitamari, R. Susuki, and K. Shimizu, "Electroless nickel plating solution and method," June 8 1999. US Patent 5,910,340.
- [155] R. Yang, P. Goethel, J. Schwartz, and C. Lund, "Solubility and diffusivity of carbon in metals," *Journal of Catalysis*, vol. 122, no. 1, pp. 206–210, 1990.
- [156] J. Santiesteban, S. Fuentes, and M. Yacaman, "Catalysis of carbon methanation by small platinum particles," *Journal of Vacuum Science & Technology A: Vacuum, Surfaces, and Films*, vol. 1, no. 2, pp. 1198–1200, 1983.
- [157] C. Gong, G. Lee, B. Shan, E. M. Vogel, R. M. Wallace, and K. Cho, "First-principles study of metal–graphene interfaces," *Journal of Applied Physics*, vol. 108, no. 12, p. 123711, 2010.
- [158] W. Holstein and M. Boudart, "Hydrogenolysis of carbon and its catalysis by platinum," *Journal of Catalysis*, vol. 72, no. 2, pp. 328–337, 1981.
- [159] C. Keep, S. Terry, and M. Wells, "Studies of the nickel-catalyzed hydrogenation of graphite," *Journal of Catalysis*, vol. 66, no. 2, pp. 451–462, 1980.

- [160] P. J. Goethel and R. T. Yang, "Platinum-catalyzed hydrogenation of graphite: mechanism studied by the rates of monolayer channeling," *Journal of Catalysis*, vol. 101, no. 2, pp. 342–351, 1986.
- [161] U. K. Parashar, S. Bhandari, R. K. Srivastava, D. Jariwala, and A. Srivastava, "Single step synthesis of graphene nanoribbons by catalyst particle size dependent cutting of multiwalled carbon nanotubes," *Nanoscale*, vol. 3, no. 9, pp. 3876–3882, 2011.
- [162] R. Saito, A. Jorio, A. Souza Filho, G. Dresselhaus, M. Dresselhaus, and M. Pimenta, "Probing phonon dispersion relations of graphite by double resonance Raman scattering," *Physical Review Letters*, vol. 88, no. 2, p. 027401, 2001.
- [163] I. Meric, C. R. Dean, A. F. Young, N. Baklitskaya, N. J. Tremblay, C. Nuckolls, P. Kim, and K. L. Shepard, "Channel length scaling in graphene field-effect transistors studied with pulsed current- voltage measurements," *Nano Letters*, vol. 11, no. 3, pp. 1093–1097, 2011.
- [164] Y.-J. Yu, M. Y. Han, S. Berciaud, A. B. Georgescu, T. F. Heinz, L. E. Brus, K. S. Kim, and P. Kim, "High-resolution spatial mapping of the temperature distribution of a Joule self-heated graphene nanoribbon," *Applied Physics Letters*, vol. 99, no. 18, p. 183105, 2011.
- [165] T. E. Beechem, R. A. Shaffer, J. Nogan, T. Ohta, A. B. Hamilton, A. E. McDonald, and S. W. Howell, "Self-heating and failure in scalable graphene devices," *Scientific Reports*, vol. 6, p. 26457, 2016.
- [166] A. Betti, G. Fiori, G. Iannaccone, and Y. Mao, "Physical insights on graphene nanoribbon mobility through atomistic simulations," in *IEEE International Electron Devices Meeting*, pp. 897–900, IEEE, 2009.
- [167] Y. Yang and R. Murali, "Impact of size effect on graphene nanoribbon transport," *IEEE Electron Device Letters*, vol. 31, no. 3, pp. 237–239, 2010.
- [168] H. Zhong, Z. Zhang, H. Xu, C. Qiu, and L.-M. Peng, "Comparison of mobility extraction methods based on field-effect measurements for graphene," *AIP Advances*, vol. 5, no. 5, p. 057136, 2015.

- [169] M. Bresciani, A. Paussa, P. Palestri, D. Esseni, and L. Selmi, “Low-field mobility and high-field drift velocity in graphene nanoribbons and graphene bilayers,” in *IEEE International Electron Devices Meeting*, pp. 724–727, IEEE, 2010.
- [170] X. Yu, J. Zhang, J. Kang, H. Qian, Z. Yu, and Y. Tan, “Study on carrier mobility in graphene nanoribbons,” in *International Conference on Simulation of Semiconductor Processes and Devices*, pp. 219–222, IEEE, 2011.
- [171] T. Fang, A. Konar, H. Xing, and D. Jena, “Mobility in semiconducting graphene nanoribbons: Phonon, impurity, and edge roughness scattering,” *Physical Review B*, vol. 78, no. 20, p. 205403, 2008.
- [172] V. Passi, A. Gahoi, B. V. Senkovskiy, D. Haberer, F. R. Fischer, A. Grüllneis, and M. C. Lemme, “Field-effect transistors based on networks of highly aligned, chemically synthesized $N = 7$ armchair graphene nanoribbons,” *ACS Applied Materials and Interfaces*, vol. 10, no. 12, pp. 9900–9903, 2018.
- [173] M. Ohtomo, Y. Sekine, H. Hibino, and H. Yamamoto, “Graphene nanoribbon field-effect transistors fabricated by etchant-free transfer from au (788),” *Applied Physics Letters*, vol. 112, no. 2, p. 021602, 2018.
- [174] S.-J. Jeong, S. Jo, J. Lee, K. Yang, H. Lee, C.-S. Lee, H. Park, and S. Park, “Self-aligned multichannel graphene nanoribbon transistor arrays fabricated at wafer scale,” *Nano Letters*, vol. 16, no. 9, pp. 5378–5385, 2016.
- [175] T. Kato and R. Hatakeyama, “Site-and alignment-controlled growth of graphene nanoribbons from nickel nanobars,” *Nature Nanotechnology*, vol. 7, no. 10, p. 651, 2012.
- [176] A. D. Liao, J. Z. Wu, X. Wang, K. Tahy, D. Jena, H. Dai, and E. Pop, “Thermally limited current carrying ability of graphene nanoribbons,” *Physical Review Letters*, vol. 106, no. 25, p. 256801, 2011.
- [177] M. Terrones, F. Banhart, N. Grobert, J.-C. Charlier, H. Terrones, and P. Ajayan, “Molecular junctions by joining single-walled carbon nanotubes,” *Physical Review Letters*, vol. 89, no. 7, p. 075505, 2002.

- [178] L. He, J.-Q. Lu, and H. Jiang, “Controlled carbon-nanotube junctions self-assembled from graphene nanoribbons,” *Small*, vol. 5, no. 24, pp. 2802–2806, 2009.
- [179] P. Koskinen, S. Malola, and H. Häkkinen, “Self-passivating edge reconstructions of graphene,” *Physical Review Letters*, vol. 101, no. 11, p. 115502, 2008.
- [180] M. Ishigami, J. Chen, W. Cullen, M. Fuhrer, and E. Williams, “Atomic structure of graphene on SiO₂,” *Nano Letters*, vol. 7, no. 6, pp. 1643–1648, 2007.
- [181] X. Li, W. Cai, J. An, S. Kim, J. Nah, D. Yang, R. Piner, A. Velamakanni, I. Jung, E. Tutuc, *et al.*, “Large-area synthesis of high-quality and uniform graphene films on copper foils,” *Science*, vol. 324, no. 5932, pp. 1312–1314, 2009.
- [182] A. Shen, Y. Zou, Q. Wang, R. A. Dryfe, X. Huang, S. Dou, L. Dai, and S. Wang, “Oxygen reduction reaction in a droplet on graphite: direct evidence that the edge is more active than the basal plane,” *Angewandte Chemie International Edition*, vol. 53, no. 40, pp. 10804–10808, 2014.
- [183] K. K. Ghuman, S. Yadav, and C. V. Singh, “Adsorption and dissociation of H₂O on monolayered MoS₂ edges: Energetics and mechanism from ab initio simulations,” *The Journal of Physical Chemistry C*, vol. 119, no. 12, pp. 6518–6529, 2015.
- [184] K. Wong, S. J. Kang, C. W. Bielawski, R. S. Ruoff, and S. K. Kwak, “First-principles study of the role of O₂ and H₂O in the decoupling of graphene on Cu (111),” *Journal of the American Chemical Society*, vol. 138, no. 34, pp. 10986–10994, 2016.
- [185] M. Wang, J. Wang, Q. Chen, and L.-M. Peng, “Fabrication and electrical and mechanical properties of carbon nanotube interconnections,” *Advanced Functional Materials*, vol. 15, no. 11, pp. 1825–1831, 2005.

List of Publications

1. P. Jangid, D. Pathan, and A. Kottantharayil, "Graphene nanoribbon transistors with high I_{ON}/I_{OFF} ratio and mobility", *Carbon*, vol. 132, pp. 65-70, 2018.
2. P. Jangid and A. Kottantharayil, "Reconstruction of Fractured Graphene by Thermal Treatment in Methane Gas", Manuscript under Review.
3. P. Jangid and A. Kottantharayil, "Fabrication of Graphene Nanoribbons by Metal Nanocrystal Assisted Etching", in *3rd International Conference on Emerging Electronics IEEE*, 2016.
4. P. Jangid and A. Kottantharayil, "Fabrication of Graphene nanoribbons by Pt-catalyzed etching of Graphene", in *Graphene Week*, 2018.